UNIVERSIDADE FEDERAL DO RIO GRANDE DO NORTE
CENTRO DE CIÊNCIAS EXATAS E DA TERRA
PROGRAMA DE PÓS-GRADUAÇÃO EM GEODINÂMICA E GEOFISICA

TESE DE DOUTORADO

CARACTERIZAÇÃO DE FALHAS UTILIZANDO DADOS DE AFLORAMENTO E SÍSMICA DE REFLEXÃO 3D, BACIA RIO DO PEIXE - BRASIL

Autor:

LORENNA SÁVILLA BRITO OLIVEIRA

Orientador:

PROF. DR. FRANCISCO HILÁRIO REGO BEZERRA

Coorientador:

PROF. DR. FRANCISCO CÉZAR COSTA NOGUEIRA

Tese nº 78/PPGG

Março de 2023

Natal/RN, Brasil

LORENNA SÁVILLA BRITO OLIVEIRA

CARACTERIZAÇÃO DE FALHAS UTILIZANDO DADOS DE AFLORAMENTO E SÍSMICA DE REFLEXÃO 3D, BACIA RIO DO PEIXE - BRASIL

Tese apresentada em 13 de março de 2023 ao Programa de Pós-Graduação em Geodinâmica e Geofísica (PPGG) da Universidade Federal do Rio Grande do Norte (UFRN) como requisito à obtenção do Título de Doutor em Geodinâmica e Geofísica, Área de Concentração Geodinâmica.

BANCA EXAMINADORA:

PROF. DR. FRANCISCO HILÁRIO RÊGO BEZERRA
Presidente e orientador (PPGG-UFRN)

_____

PROF. DR. DAVID LOPES DE CASTRO
Membro interno (PPGG-UFRN)

_____

DRA. INGRID BARRETO MACIEL
Membro interno (UFRN)

_____

DR. MATHEUS AMADOR NICCHIO
Membro Externo (UFRJ)

_____

DR. KLEDSON TOMASO PEREIRA DE LIMA
Membro externo (PETROBRÁS)

_____

‘Minha neta vai estudar bem longe,
E que seja feliz no mei dos mato,
Que se eu fosse da sua idade faria o mesmo,
ia estudar e ganhar o mundo’

A rainha que me apoiou em tudo que descobri que sou,
A minha avó Rita.

Universidade Federal do Rio Grande do Norte - UFRN
Sistema de Bibliotecas - SISBI
Catalogação de Publicação na Fonte. UFRN - Biblioteca Setorial Prof. Ronaldo Xavier de Arruda - CCET

Oliveira, Lorenna Sávilla Brito.
Caracterização de falhas utilizando dados de afloramento e sísmica de reflexão 3D, Bacia Rio do Peixe – Brasil / Lorenna Sávilla Brito Oliveira. – 2023.
xvii, 121f.: il.

Tese (doutorado) – Universidade Federal do Rio Grande do Norte, Centro de Ciências Exatas e da Terra, Programa de Pós-Graduação em Geodinâmica e Geofísica. Natal, RN, 2023.
Orientador: Prof. Dr. Francisco Hilário Rego Bezerra.
Coorientador: Prof. Dr. Francisco Cézar Costa Nogueira.

1. Estratigrafia mecânica – Tese. 2. Bandas de deformação – Tese. 3. Propriedades petrofísicas – Tese. 4. Atributos sísmicos – Tese. 5. Machine learning – Tese. 6. Bacia Rio do Peixe – Tese. I. Bezerra, Francisco Hilário Rego. II. Nogueira, Francisco Cézar Costa. III. Título.

RN/UF/CCET CDU 551.7

Elaborado por Joseneide Ferreira Dantas – CRB-15/324

AGRADECIMENTOS

Finalizando esse período do processo de doutoramento, eu gostaria de agradecer as pessoas que contribuíram no meu crescimento, me deram acolhimento e também aos que profissionalmente fizeram parte da minha vida nos últimos anos.

Agradeço a PETROBRÁS e ao Projeto DEBRIP (Bandas de deformação Rio do Peixe: análise multiescalar e geração de banco de dados geofísicos, modelagem e simulação numérica) pelo financiamento da minha bolsa de auxílio estudantil e também os períodos de coleta de campo durante esses quase 4 anos. Além disso, o projeto científico me proporcionou a oportunidade de interagir com pesquisadores de outros países, os quais sempre foram fundamentais no meu processo de doutoramento. Com isso, sou grata a Universidade Federal do Rio Grande do Norte (UFRN), a Universidade Federal de Campina Grande (UFCG), ao Programa de Pós-Graduação em Geodinâmica e Geofísica (PPGG) e principalmente aos laboratórios que estive envolvida: Laboratório de Pesquisa em Exploração Petrolífera (LAPEP) e Laboratório de Sismologia (LABSIS), no qual fiquei instalada por todos esses anos.

Agradeço aos meus orientadores Francisco Hilário e Francisco Cézar por todos os ensinamentos que me deram desde o período de graduação, mestrado e no doutorado. Agradeço ambos pela paciência, consideração, por acreditarem em mim e na minha capacidade como cientista, por todos os momentos de campo que estávamos cansados e felizes encontrando afloramentos ou contando bandas de deformação em cima de escada ou cobras. Eu gostaria de agradecer especificamente a Cezar por ter aberto as portas em uma universidade em outro Estado, por ter confiado e me enviado para interagir com a maioria dos pesquisadores que conheci nos últimos anos; os anos passam e do mesmo jeito que o conheci em campo brilhando os olhos pelas estruturas ele continua com a mesma expressão por todo esse tempo, muito obrigada por toda inspiração geológica, compartilhamento de artigos, ideias e modelos; e principalmente por todo o esforço de atender todas as minhas ligações com pedidos de socorro. Eu gostaria de agradecer especificamente a Hilário, o qual me aceitou como orientanda desde a graduação até os dias atuais. A Hilário eu sou eternamente grata por muitos motivos, desde ter se colocado por mim quando tive a possibilidade de sair do curso de graduação injustamente, a ter me ‘empurrado’ pra falar inglês com todos os

pesquisadores internacionais que vieram pra interagir com ele; eu penso que sempre falei ‘sim’ para todas as tarefas que Hilário me passou por ele ter acreditado na minha capacidade de pesquisadora antes de mim todos esses anos. Professor, muito obrigada por todos esses anos de conversas sinceras, por todas as portas abertas, por estar disponível ao diálogo e por todas as chances que demos a nós mesmos.

Agradeço aos professores que também me orientaram não oficialmente dentro do processo do doutorado. A Patrick Cobertt eu agradeço muito por ter insistido no meu primeiro artigo, por ter me acolhido e insistido em mim! A toda poesia que a geologia traz, Patrick que agora faz poesia me encantou muito admirando rochas e a petrofísica, e sou eternamente grata por isso. A Fabrizio Balsamo eu agradeço imensamente pela generosidade e acolhimento de todos esses anos, por ter paciência no ensino, por cada chamada de vídeo para discutir geologia e desenhar as zonas de falha (obrigada, Fabri!). Agradeço a Anita Torabi e Behzad Alaei por toda inspiração, paciência, ética, confiança, atenção, incentivo, acolhimento, orientação e pelos puxões de orelha; ambos mudaram meu jeito de ver ciência, de entender as relações profissionais, e principalmente os agradeço por me proporcionarem a oportunidade de poder ser eu mesma no ambiente científico, podendo atuar feliz sendo pesquisadore.

Agradeço aos profissionais da UFRN que tão gentilmente mantiveram esses espaços limpos, conduziram carros, me concederam chaves e pelas trocas de ideais regados de cafezinhos (obrigada Josi e todos da secretaria LABSIS; a Antônio Vicente, Fernando Feitosa e carinhosamente a ‘Seu’ Pedro, agradeço por cuidarem de mim e serem companheiros de campo). Onde estive trabalhando fiz amigos, e por isso gostaria de agradecer aos meus companheiros de LAPEP, que foram fundamentais para o presente momento, se esforçaram ligaram os computadores por todo período de pandemia com alegria em cada ‘bom dia’. Obrigada Igor (do coração imenso num pote pequenininho, se fazendo presente mesmo que distante), ‘Carol’, Gabriel, ‘Duda’, Amanda, ‘Leo’ Palhano, Eli, Thiago, ‘Klyn’, ‘Jane’ e Rayanna por todos os ‘lapeps’ compartilhados, campos, diárias, e momentos não tão sóbrios. Atuando de forma crucial na minha formação enquanto cientista, eu gostaria de agradecer a David Lino por ser meu guia/orientador, e principalmente pela nossa amizade em todo o doutorado! David, muito obrigada por ter me escutado em todas as minhas frustrações dentro do doutorado,

por ter me inspirado e compartilhado tantos trabalhos, por tentar me animar com fotos e vídeos de ‘Jujubinha’, por acreditar em mim e me elogiar em qualquer lugar do mundo, e a ‘Gabi’ especialmente muito obrigada por te ceder em todas as chamadas fora de hora.

Agradeço aos meus companheiros de LABSIS, os quais compartilham as tristezas e alegrias de vida de pós-graduando. Obrigada Ingrid por toda confiança e troca em momentos difíceis e das boas histórias. Agradeço ao meu amigo Vincenzo (o gringo natalense) por me conceder o cargo inicial de tradutora oficial, mas principalmente por todo carinho diário. A Juliana (juju), Renata, Francesca e Luca agradeço por todos os ombros e momentos de escuta. Especialmente agradeço imensamente aos que estiveram me aguentando por rotina no mesmo espaço físico de ‘problemas inversos’: a Cayo, Juliana Rabelo e João (o ruivo), sou muito feliz por ter vocês como pesquisadores e principalmente como meus amigos de vida, ouvindo meus dramas, tirando cochilos juntos, opinando em figuras e pirações geológicas! Obrigada a todos os componentes do ‘Labisisters and Cousins’. Agradeço ao meu ‘mano’ Flauber por todos os salves de ansiedades, respiros e rotina extenuante compartilhadas nos momentos de por do sol e luas. A todas as mulheres que lutaram nos últimos dois anos por respeito e existência, eu gostaria de agradecer a força, apoio e sororidade, e em especial sou grata carinhosamente a professora Aline e a Sofia por toda resistência e insistência na manutenção do respeito e ética no espaço.

Agradeço aos amigos que fiz em Oslo, por terem permitido os cafezinhos e dramas brasileiros, por terem me apresentado o coração tão rapidamente, por me mostrarem inspiração com suas pesquisas, e por terem estado comigo da glória ao estrago mental. Obrigada Hege, Aurora, Owen, Letícia, John, Sian, Nora, Mohammad Masoudi, Federica, Juan e Wiktor, fica registrado meu carinhoso ‘Takk’ por tudo que viemos. Agradeço ao casal que me deu teto, instrumentos e risadas em meio ao frio da Noruega, muito obrigada a Kenny e Lars por literalmente me abrigarem. Em especial agradeço a Abhisek Basa por ter sido meu suporte, por cuidar de mim, ser meu amigo, companheiro de rotina, por dividir sua vida comigo.

Agradeço aos meus amigos queridos fora da vida geológica, os quais me mantiveram sã e me amaram quando a sanidade acabou durante um doutoramento,

pandemia e situação de ‘BR’ nos últimos anos. Com meu mais profundo amor e carinho eu os agradeço por tudo, por se manterem comigo e serem quem são nos momentos em que mais me perdi de mim. Agradeço especialmente a quem me tirou literalmente do laboratório pra respirar, me trouxe de volta a mim mesma, me amou e ninou, me deu praia e festival, quem me deu puxão de orelha e ouviu muitíssimo sobre ‘falhas’, meu profundo ‘muito obrigada’ as minhas queridas amigas Isabela, Victória e Alessandra. Agradeço aos meus ex vizinhos de quarto Jordy e Pablo por compartilharem a loucura de viver no mato perto da praia durante o doutorado, por todos os momentos de ouvir e de salvação, meu carinhoso obrigado pela amizade. Agradeço a todos os moradores da Vila Paraíso que tornaram a vizinha geóloga uma pessoa comunitária, em especial a Serena por ser minha melhor amiga em tempos pandêmicos. Agradeço de todo meu coração a minha amigona Luiza, que me atura desde que entrei na jornada de ser geóloga, dividindo a vida e sala comigo desde cálculo I e recentemente na nossa salinha de hoje; obrigada amigona por ser quem é e por nos permitir tanto, e especialmente a Giovanna por toda gentileza, carinho e animação convivendo dentro dessa amizade e sendo companheira; eu não tenho como expressar em palavras a minha gratidão a vocês por me abraçarem e me acolherem diante de todo o colapso nos últimos anos. Agradeço a Izabella e Mayara por tanto amor que atravessa a fronteira PB-RN, por sempre se permitirem ser meu abrigo sem importar o que aconteça.

Agradeço a minha família, minha base e de onde vem imenso suporte e incentivo desde que reencarnei. Agradeço profundamente a minha mãe Augusta por tanto acreditar em mim, por me apoiar mesmo sem entender, por investir em mim, por dedicar boa parte da sua vida na minha felicidade, por ter guardado minhas amostras de rocha desde criancinha, por ter me permitido viver a profissão que me faz feliz, mas que tanto a aflige em meio a aventuras. Agradeço ao meu pai Élidon e meu irmão Giorgio, por me amarem tanto diante de tanta diversidade de quem sou, por escutarem tanto sobre palavras geológicas sem sentido, e por e me acolherem desde que nasci aos dias mais amargos nos últimos anos que sobrevivemos. Agradeço aos que me amam e cuidam do outro lado da vida, a família maior e a Deus pela existência, ao meu mentor por toda fidelidade, e a minha avó por ser tão grandiosa comigo e ceder aos meus carinhos em meio a tantas questões.

RESUMO

Zonas de falha acomodam a deformação de forma complexa, apresentando-se com diferentes geometrias, gerando variados tipos de estruturas secundárias e alterando parâmetros petrofísicos de rochas hospedeiras. Em uma perspectiva de exploração de reservatórios siliciclásticos de hidrocarbonetos, a compreensão da complexidade de zonas de falha é necessária, uma vez que essas estruturas alteram volumes de rocha influenciando assim no fluxo de fluidos. No desafio de entender essas estruturas faz necessário o uso de metodologias convencionais, proporcionando relações com o arcabouço estrutural da bacia, assim como compreendendo a deformação de uma zona de falha desde a escala de afloramento, onde é possível observar estruturas secundárias como bandas de deformação. Nessa pesquisa, foram investigadas zonas de falhas na Bacia Rio do Peixe em escala de afloramento, entendendo a influência mecânico-estratigráfica das bandas de deformação, e também foi realizada a detecção e caracterização de falhas de forma automática através de dados de sísmica de reflexão. Para isso, foram combinados dados estruturais, sedimentológicos e petrofísicos para analisar as propriedades geomecânicas das rochas, e caracterizar a alteração nas propriedades petrofísicas das rochas gerada por bandas de deformação. Ainda, foram utilizados dados sísmicos para a detecção automática de falhas através de atributos sísmicos e técnica de aprendizagem profunda de máquina. Nossos resultados mostram a influência mecânico-estratigráfica de bandas deformação em uma zona de falha que indicam mesma tendência regional de direção NE-SW, E-W e NW-SE, gerando alterações evidenciadas por nossos modelos em parâmetros petrofísicos como porosidade, permeabilidade, modulo de Young e razão de Poisson. As bandas de deformação transpassam as camadas sedimentares sem estarem condicionada a espessura dessas, variando parâmetros estruturais como frequência, mergulho, geometria e espessura de bandas. Em relação as análises de zona de falha em macro escala, nossos resultados demonstram uma comparação entre atributos sísmicos e aprendizagem profunda (DNN), na qual o DNN é mais bem sucedido na detecção de falhas, identificando seus segmentos subsidiários com maior variação de direção e quantidade de falhas menores. Atributos sísmicos se mostram condicionados ao ruido

no dado sísmico. Ainda, interpretamos e mapeamos uma nova falha, que está alinhada paralela a Falha Malta de direção E-W, com uma estrutura em flor negativa central.

Palavras-chave: Estratigrafia Mecânica; Bandas de Deformação; Propriedades Petrofísicas; Atributos Sísmicos; Machine Learning; Detecção Automática; Bacia Rio do Peixe.

ABSTRACT

Fault zones accommodate deformation in a complex pattern, presenting themselves with different geometries, types of secondary structures, and changing the petrophysical parameters of host rocks. From a perspective of exploration of siliciclastic hydrocarbon reservoirs, understanding the complexity of fault zones has become fundamental, since these structures alter rock volumes, thus influencing fluid flow. The challenge of understanding these structures requires the use of conventional methodologies, providing relationships with the structural framework of the basin, as well as understanding the deformation of a fault zone from the outcrop scale, where it is possible to observe secondary structures such as deformation bands. In this research, fault zones in the Rio do Peixe Basin were investigated at the outcrop scale, understanding the mechanical-stratigraphic influence of deformation bands, and fault detection and characterization were also performed automatically using reflection seismic data. For this, structural, sedimentological and petrophysical data were combined to analyze mechanically the rock layers, and to characterize the deformation generated by deformation bands. Also, seismic data were used for automatic fault detection through seismic attributes and deep learning. Our results show the mechanical-stratigraphic influence of deformation bands in a fault zone that indicate the same regional trend of NE-SW, E-W and NW-SE direction, generating changes evidenced by our models in petrophysical parameters such as porosity, permeability, Young's modulus and Poisson's ratio. The deformation bands cross the sedimentary layers without being conditioned to their thickness, varying structural parameters such as frequency, dip, geometry and thickness of the bands. Our results also demonstrate the comparison between seismic attributes and deep learning (DNN), in which DNN is more successful in detecting faults, identifying their subsidiary segments with more strikes variation and number of minor faults. Seismic attributes are shown to be conditional on noise in the seismic data. Furthermore, we interpreted and mapped a new fault, which is aligned parallel to Fault Malta of E-W direction, with a central negative flower structure.

Keywords: Mechanical Stratigraphy; Deformation Bands; Petrophysical Properties; Seismic Attributes; Machine Learning; Automatic Detection; Rio do Peixe Basin.

Sumário

LISTA DE FIGURAS E TABELAS

CAPITULO 4

Artigo 2

Capítulo 1

Introdução

1 Introdução

1.1 Apresentação

A presente Tese de Doutorado é parte dos requisitos para a obtenção da titulação em Doutor(a) em Geodinâmica e Geofísica, o qual é conferido pelo Programa de Pós Graduação em Geodinâmica e Geofísica (PPGG) da Universidade Federal do Rio Grande do Norte (UFRN). Com esse estudo, pretendeu-se compreender, detectar e caracterizar falhas e suas feições geométricas na Bacia Rio do Peixe (BRP), sendo esse contexto análogo de reservatórios siliciclásticos de hidrocarbonetos.

A presente pesquisa tem um caráter multidiciplinar correlacionando várias metodologias objetivando a caracterização geométrica de falhas em diferentes escalas na BRP. A aplicação dessas metodologias teve o apoio financeiro e logístico do projeto "Bandas de deformação Rio do Peixe (DEBRIP): análise multiescalar e geração de banco de dados geofísicos, modelagem e simulação numérica", financiado pela PETROBRAS e executado pela Universidade Federal de Campina Grande (UFCG), tendo colaboração da Universidade Federal do Rio Grande do Norte (UFRN). Parte da pesquisa com enfoque em detecção de falhas através de apredizagem de máquina foi financiada pela Nasjonal Forskerskole i Petroleumsfag (NFiP) – Petroleum Reseach School of Norway em parceria com a Universidade de Oslo (UiO). Essa pesquisa foi desenvolvida sob a orientação do Prof. Dr. Francisco Hilário Rego Bezerra e coorientação do Prof. Dr. Francisco Cézar Costa Nogueira, o qual também é o coordenador do projeto DEBRIP que apoiou os trabalhos do presente doutoramento através da bolsa-auxílio.

1.2 Estrutura da Tese

A presente tese se estrutura em cinco capítulos, nos quais serão apresentados os resultados, metodologias e discussões desta pesquisa na forma de artigos científicos redigidos e em processo de submissão em periódicos internacionais. Com isso, apresenta-se a tese, seus objetivos, justificativas, localização da área de estudo e base de dados no presente *Capítulo 1 (Introdução)*. Este capítulo introdutório tem como finalidade de apresentar o leitor em relação a área de estudo, às especificidades das justificativas e lacunas cientificas, assim como, aos objetivos propostos e suas contribuições para com a comunidade científica.

Seguindo o modelo de estrutura descrito anteriormente, o *Capítulo 2 (Contexto Geológico)* aborda os principais temas acerca do arcabouço estrutural, formações litoestratigráficas e evolução tectônica da Bacia Rio do Peixe. Além disso, são discutidas mais objetivamente características e contribuições cientificas recentes sobre bandas de deformação, uma vez que essas estruturas são alvo desta pesquisa e estão presentes na área de estudo.

No *Capítulo 3 (Referencial Teórico)*, serão apresentados brevemente os conceitos e definições acerca dos temas que embasam a caracterização de zonas de falhas em diferentes escalas, se dividindo em zona de falha, estratigrafia mecânica e atributos sísmicos na detecção de falhas utilizando dados de sísmica de reflexão 3D.

No *Capítulo 4 (Resultados)*, são apresentados os resultados em forma de manuscritos redigidos durante o tempo de doutoramento. O primeiro manuscrito tem como título “*Mechanical Stratigraphy Influences Deformation Band Pattern in Arkosic*

Sandstones, Rio do Peixe Basin, Brazil", e foi publicado no periódico *Journal of Structural Geology* em 4 de Janeiro de 2022. Em seguida, é apresentado o manuscrito "*Automatic 3D fault detection and characterization – a comparison between seismic attribute methods and deep learning*", o qual foi submetido no dia 15 de fevereiro de 2023 no periódico *Interpretation*, onde encontra-se em fase de revisão até o presente momento de confecção desta Tese.

No *Capítulo 5 (Conclusões)*, são apresentados em síntese as principais conclusões de ambos artigos e suas contribuições para o entendimento da caracterização estrutural de falhas na Bacia Rio do Peixe através de dados de afloramento e sísmica de reflexão.

1.3 Justificativas e Objetivos

Reservatórios siliciclásticos falhados apresentam uma grande variedade de controles em relação a essas estruturas, os quais precisam ser caracterizados e descritos para que assim possam ser compreendidos estes reservatórios e, posteriormente, modelados. Contudo, as falhas podem apresentar um complexo padrão de distribuição das suas estruturas secundárias, tais como falhas menores, juntas, fraturas, bandas de deformação (Caine et al., 1996; Fossen et al., 2007). Além disso zonas de falhas também apresentam complexidade em relação a sua geometria (Nicol et al., 1995; Admasu et al., 2006; Gui et al., 2021), e quantificação de parâmetros como espessura, abertura e orientação, tornando assim a caracterização destes sistemas muito onerosa em termos de uma análise geométrica convencional.

A presença de estruturas tectônicas pode favorecer o acúmulo e/ou servir como condutos no carreamento de fluidos, como hidrocarbonetos, os quais podem migrar ao longo destas estruturas formadas (e.g., Berndt, 2005; Ligtenberg, 2005; Hustoft et al., 2007; Kluesner and Brothers, 2016). Zonas de falha podem gerar na rocha hospedeira espaços vazios como fraturas secas, que podem atuar como condutos de fluxo e potencializar zonas de alta permeabilidade (Pontes et al., 2020), agindo como caminhos de preferência para fluxos gerados nessas rochas (Bezerra et al., 2007). Assim como, a presença de falhas também pode gerar estruturas como bandas de deformação, podendo ser oriundas do processo de cisalhamento e cominuição/cataclase de grãos (Nogueira et al., 2021), e até recristalização de minerais e/ou foliação ao longo dessas estruturas rúpteis (Nicchio et al., 2018). Com isso, essas estruturas se mostram ainda mais complexas ao atuarem como barreiras na migração de fluxos e até condutos em outros casos (Medeiros et al., 2010). Apesar do largo avanço nas caracterizações estruturais de bandas de deformação, não têm sido totalmente elucidados os parâmetros mecânico-estratigráficos e quais os impactos da presença dessas estruturas em reservatórios petrolíferos. A estratigrafia mecânica que investiga a relação entre a reologia das camadas sedimentares e a intensidade de fraturas (e.g., Mcquillan, 1974; Bai and Pollard, 2000; Bertotti et al., 2007; Cooke et al., 2006; Zahm and Hennings, 2009; Lavenu and Lamarche, 2018), vem tendo enfoque, principalmente, em estruturas como fraturas, juntas, e linkagem entre essas estruturas (Ferrill and Morris, 2003; Ferrill and Morris, 2008; Morris et al., 2009b; Roche et al., 2013; La Bruna et al., 2021; Pontes et al., 2021). Ainda, dependendo do tipo de rocha afetada pela deformação de zonas de falhas, estruturas secundarias geradas podem ser bandas de deformação em contexto

de rochas com porosidade alta, tornando a análise mecânico-estratigráfica mais complexa. Por esse motivo, estudos envolvendo diversas técnicas de análises mecânico-estratigráficas, em escalas de detalhe, são necessários para povoar cadeias de falhas e suas zonas de dano contendo bandas de deformação, sendo importantes na quantificação da porosidade e permeabilidade de reservatórios siliciclásticos e para simulação de fluxo de fluidos.

Objetivando compreender a complexidade das zonas de falhas, estudos baseados em dados de subsuperfície reconhecem e descrevem parâmetros que caracterizam essas estruturas tridimensionalmente em relação as estruturas internas (e.g., Jones e Knipe, 1996; Cohen et al., 2006; Botter et al., 2014; Liao et al., 2019), predição de crescimento de falhas (e.g., Mansfield e Cartwright, 1996; Preuss et al.,2019), e medição de rejeito e deslocamento dessas (e.g., Walsh e Watterson, 1987; Hale, 2013; Ma et al., 2019). Avanços significativos na área de interpretação sísmica automatizaram e facilitaram processos na detecção de falhas através de atributos sísmicos (Bahorich e Farmer, 1995; Chopra e Marfurt, 2005, 2007, 2010b; Brouwer e Huck, 2011; Libak et al., 2017; Qi et al., 2019), objetivando a identificar zonas de deformação e até padrões de fluxos de fluidos nessas zonas (Berndt, 2005; Iacopini et al., 2016; Kluesner e Brothers, 2016; Liao et al., 2020). Mais recentemente, vem se utilizando de técnicas de aprendizagem de máquina na automatização do processo, redução de tempo, gastos e detecção e predição de estruturas rúpteis e até domos de sal no dado sísmico (Purves et al., 2008; Di et al., 2018; Wu e Zhang, 2018 Wu et al., 2019; Wrona et al., 2020; An et al., 2021). Ainda que haja um potencial avanço em relação a predição automática de falhas na interpretação sísmica, existem diversas

dificuldades na interpretação do dado sísmico *onshore* como ruídos, problemas de aquisição, processamento e tamanho do dado, criando assim maiores desafios na compreensão do arcabouço estrutural de bacia sedimentares continentais.

A Bacia Rio do Peixe localizada no estado da Paraíba é considerada como um importante análogo de reservatórios de hidrocarboneto em território brasileiro, tendo em vista o volume de sedimentos siliciclásticos depositados durante sua formação, e principalmente por apresentar reservatórios compostos por óleo maturo (Araujo et al., 2018; Maciel, et al., 2018; Nicchio, et al., 2018; Pontes, et al., 2019). Um aspecto importante nessa bacia diz respeito ao complexo padrão de distribuição das fraturas menores, assim como a quantificação de parâmetros como espessura, abertura e orientação destas estruturas que tornam a caracterização destes sistemas muito onerosa em termos de uma análise geométrica convencional (Araujo et al., 2018; Pontes et al., 2019; Souza et al., 2021; Torabi et al., 2021; Silva et al., 2022). Da mesma forma, a complexidade genética e geométrica destas estruturas, quando presentes em reservatórios, nem sempre é entendida quando são utilizados de forma isolada dados de poços e sísmicos. Com isso, compreende-se nessa bacia um cenário de análise estrutural único, sendo composto de boas exposições de zonas de falha em áreas aflorantes acima de uma subsuperfície mapeada por sísmica de reflexão e poços. Portanto, propõe-se o estudo de caracterização de zonas de falhas na Bacia do Rio do Peixe, já que essa pode ser considerada um importante análogo para o estudo de reservatórios do tipo fraturados.

A presente proposta tem como objetivo principal caracterizar falhas como zonas volumétricas, analisando de forma multiescalar essas estruturas com dados de

afloramento e de sísmica de reflexão. Com isso, serão analisadas essas estruturas em: (1) contexto de microescala e de afloramento, compreendendo desde seus diferentes aspectos acerca das bandas de deformação de forma geométrica, mecânico-estratigráfica, cinemática, petrofísica, e contexto geológico, para gerar modelos geológicos em rochas sedimentares análogas a reservatórios petrolíferos siliciclásticos; (2) em contexto de mesoescala e dados de sísmica de reflexão, detectando e caracterizando falhas em relação a sua geometria, cinemática e contexto tectônico, contribuindo com o mapeamento do arcabouço estrutural da Bacia Rio do Peixe.

Objetivos Específicos:

- Avaliar o efeito das grandes falhas e bandas de deformação sobre as propriedades petrofísicas das rochas da Formação Antenor Navarro através da extração de parâmetros petrofísicos em rochas deformadas e não deformadas. Com isto, pretende-se compreender a influência dessas estruturas rúpteis e seu efeito sobre as propriedades petrofísicas, também em microescala;
- Modelar as estruturas que deformam os depósitos da Formação Antenor Navarro em escala de detalhe com base em dados de afloramento;
- Entender a complexidade do comportamento mecânico dos estratos da Formação Antenor Navarro, e sua influência na deformação de zonas de falha, seus elementos e como esses estão distribuídos;
- Mapear e interpretar estruturas rúpteis nos dados de sísmica de reflexão, compreendendo as geometrias e estilos de falha;
- Analisar cinematicamente falhas interpretadas no dado sísmico através da examinação dos dados sísmicos tridimensionais;

- Comparar e analisar metodologias de detecção de descontinuidades no dado sísmico, afim de reconhecer o arcabouço estrutural da bacia.

1.4 Localização da Área de Estudo e Banco de Dados

A área de estudo da presente Tese se concentra na Bacia Rio do Peixe, a qual está localizada em maioria no leste do Estado da Paraíba, com áreas na divisa dos Estados do Ceará e do Rio Grande do Norte (Figura 1). Dentro dessa área estão as cidades de São João do Rio do Peixe, Souza e Uiraúna, e em proximidades as cidades de Cajazeiras e Marizópolis.

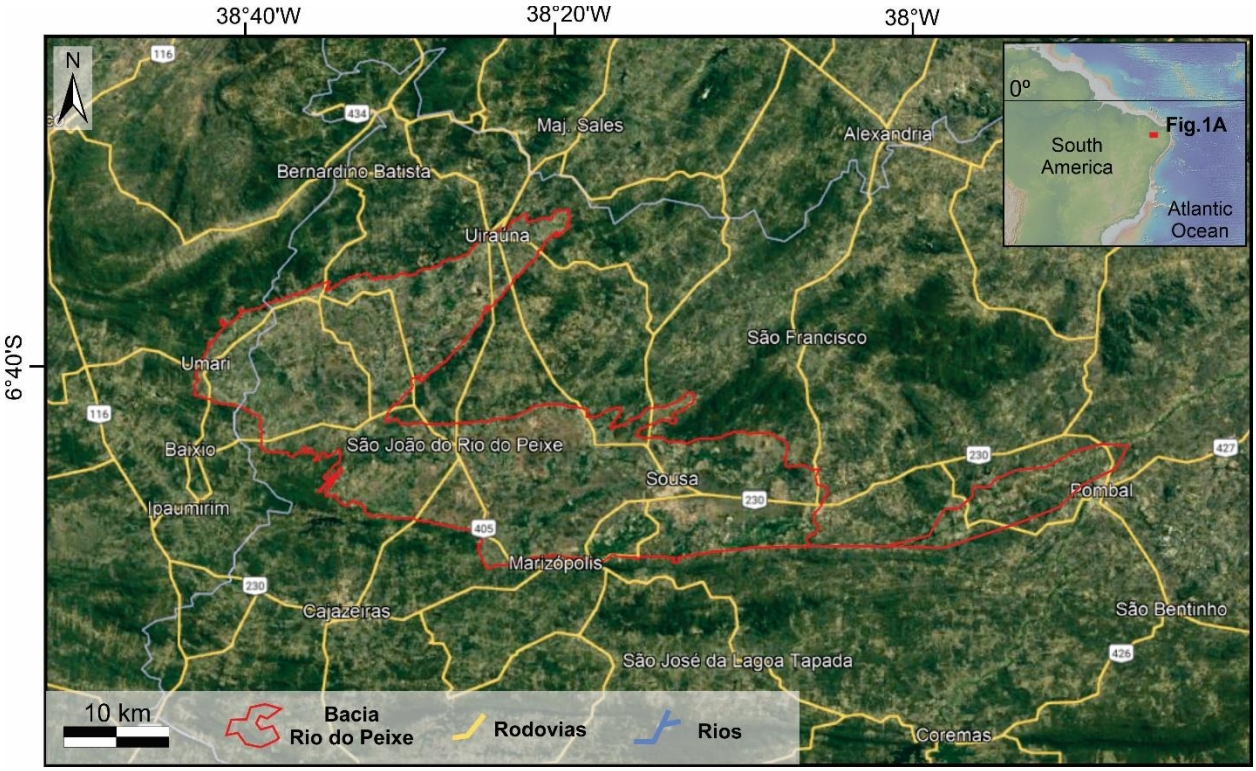

Figura 1 - Mapa de localização da Bacia Rio do Peixe, com principais municípios e vias de acesso. Fonte: Google Earth.

Para a caracterização do arcabouço estrutural da porção sudoeste da Sub-Bacia Sousa da Bacia Rio do Peixe, foram utilizados dados de sísmica de reflexão fornecido

pela Agência Brasileira de Petróleo, Gás Natural e Biocombustíveis (ANP). O conjunto de dados de reflexão sísmica 3D é exibido com polaridade inversa, seguindo a convenção SEG. O levantamento sísmico utilizado se estende até 2000 ms (TWT). Além disso, os dados sísmicos migram no tempo e tem frequência dominante de aproximadamente 30 Hz, com velocidade de intervalo de aproximadamente 3.200m/s, indicando com isso uma resolução vertical de aproximadamente 26m.

Referências:

Admasu, F., Back, S., Klaus, T., 2006, Autotracking of faults on 3D seismic data: Geophysics, **71**, 49-53, accessed 11 October 2022; doi:10.1190/1.2358399.

An, Y., Guo, J., Ye, Q., Childs, C., Walsh, J., Dong, R., 2021, Deep convolutional neural network for automatic fault recognition from 3D seismic datasets: Computers and Geosciences, 153, 104776, https://doi.org/10.1016/j.cageo.2021.104776.

Araujo, R. E. B., Bezerra, F. H. R., Nogueira, F. C. C., Carvalho, B. R. B. M., Souza, J. A. B., Sanglard, J. C. D., de Castro, D. L., Melo, A. C. C., 2018, Basement control on fault formation and deformation band damage zone evolution in the Rio do Peixe Basin, Brazil: Tectonophysics, 745, 117-131, accessed 13 September 2022; https://doi.org/10.1016/j.tecto.2018.08.011.

Bahorich, M. S., Farmer, S. L., 1995, 3-D seismic discontinuity for faults and stratigraphic features: The coherence cube: SEG Technical Program Expanded Abstracts: 93-96, https://doi.org/10.1190/1.1887523.

Bai, T., Pollard, D., 2000. Fracture Spacing in Layered Rocks: A New Explanation Based on the Stress Transition. Journal of Structural Geology 22(1):43-57. https://doi.org/10.1016/S0191-8141(99)00137-6.

Berndt, C., 2005, Focused fluid flow in passive continental margins: Philosophical Transactions of the Royal Society, 363, 2855-2871, accessed 13 September 2022; doi: 10.1098/rsta.2005.1666.

Bertotti, G., Hardebol, N., Koppen, T. J. K., Luthi, S. M., 2007. Toward a quantitative definition of mechanical units: New techniques and results from an outcropping deep-water turbidite succession (Tanqua-Karoo Basin, South Africa), Geohorizons. https://doi.org/10.1306/03060706074.

Botter, C., Cardozo, N., Hardy, S., Lecomte, I., Escalona, A., 2014, From mechanical modeling to seismic imaging of faults: A synthetic workflow to study the impact of faults on seismic: Marine and Petroleum Geology, 57, 187-207, http://dx.doi.org/10.1016/j.marpetgeo.2014.05.013.

Brouwer, F., Huck, A., 2011, An Integrated Workflow to Optimize Discontinuity Attributes for the Imaging of Faults: Attributes: New Views on Seismic Imaging – Their Use in Exploration and Production: 31st Annual, book, DOI: 10.5724/gcs.11.31.0496.

Caine, J. S., Evans, J. P., Forster, C. B., 1996, Fault zone architecture and permeability structure: Geology, 24, 1025-1028, accessed 17 October 2022; http://dx.doi.org/10.1130/0091-7613(1996)024%3C1025:FZAAPS%3E2.3.CO;2.

Chopra, S., Marfurt, K. J., 2005, Seismic Attributes: A Historical Perspective: Geophysics, **70**, 3-28, accessed 13 September 2022; https://doi.org/10.1190/1.2098670.

Chopra, S., Marfurt, K. J., 2007, Volumetric curvature attributes for fault/fracture characterization: First Break, **25**, 19-30, accessed 13 September 2022; https://doi.org/10.1190/1.2756864.

Chopra, S., Marfurt, K. J., 2010b, Delineating Fractures from Seismic Attributes: Search and Discovery Article #110124

Cohen, I., Coult, N., Vassilou, A. A., 2006, Detection and extraction of fault surfaces in 3D seismic data: Geophysics, **71**, 21-27, accessed 13 September 2022; doi:10.1190/1.2215357.

Cooke, M. L., Simo, J. A., Underwood, C. A., Rijken, P., 2006. Mechanical stratigraphic controls on fracture patterns within carbonates and implications for groundwater flow. Sedimentary Geology. Volume 184, Issues 3–4, 15, Pages 225-239. https://doi.org/10.1016/j.sedgeo.2005.11.004.

Di, H., Wang, Z., AlRegib, G., 2018a, Seismic fault detection from post-stack amplitude by convolutional neural networks: 80th EAGE Conference and Exhibition 2018. European Association of Geoscientists & Engineers, 1–5.

Ferrill, D. A., Morris, A. P., 2003. Dilational Normal Faults: Journal of Structural Geology, V. 25, P. 183–196. https://doi.org/10.1016/S0191-8141(02)00029-9.

Ferrill, D. A., Morris, A. P., 2008. Fault zone deformation controlled by carbonate mechanical stratigraphy, Balcones fault system, Texas. American Association of Petroleum Geologists. 92, 359-380. https://doi.org/10.1306/10290707066.

Ferrill, D. A., Morris, A. P., Mcginnis, R. N., Smart, K. J., Wigginton, S. S., Hill, N. J., 2017. Mechanical Stratigraphy and Normal Faulting. Journal of Structural Geology. https://doi.org/10.1016/j.jsg.2016.11.010.

Fossen, H., Schulz, R. A., Shipton, Z. K., Mair, K., 2007, Deformation bands in sandstone — A review: Geological Society (London), 164, 755-769, accessed 17 October 2022; doi:10.1306/07300706146

Gui, B., He, H., Zhang, Y., Sun, Y., Zhang, W., 2021, 3D geometry and kinematics of the Niudong Fault, Baxian Sag, Bohai Bay Basin, Eastern China—Insights from high-resolution seismic data: Journal Structural Geology, 146, 104307, accessed 11 October 2022; https://doi.org/10.1016/j.jsg.2021.104307.

Hale, D., 2013, Methods to compute fault images, extract fault surfaces, and estimate fault throws from 3D seismic images: Geophysics, 78, 033–043, doi: 10.1190/geo2012-0331.1.

Hustoft, S., Mienert, J., Bünz, S., Nouzé, H., 2007, High-resolution 3D-seismic data indicate focussed fluid migration pathways above polygonal fault systems of the mid-Norwegian margin: Marine Geology, 245, 89-106, accessed 13 September 2022; doi:10.1016/j.margeo.2007.07.004.

Iacopini, D., Butler, R. W. H., Purves, S., McArdle, N., De Freslon, N., 2016, Exploring the seismic expression of fault zones in 3D seismic volumes: Journal of Structural Geology, 89, 54-73, accessed 13 September 2022; https://doi.org/10.1016/j.jsg.2016.05.005.

Jones, G., Knipe, R. J., 1996, Seismic attribute maps; application to structural interpretation and fault seal analysis in the North Sea Basin: First Break, 14, accessed 13 September 2022; https://doi.org/10.3997/1365-2397.1996024.

Kluesner, J. W., Brothers, D. S., 2016, Seismic attribute detection of faults and fluid pathways within an active strike-slip shear zone: New insights from high-resolution 3D P-Cable™ seismic data along the Hosgri Fault, offshore California: Interpretation, 4, 1F-T121, accessed 13 September 2022; https://doi.org/10.1190/INT-2015-0143.1.

La Bruna, V., Bezerra, F.H.R., Souza, V.H.P., Maia, R.P., Auler, A.S., Araujo, R.E.B., Cazarin, C.L., Rodrigues, M.A.F., Vieira, L.C., Sousa, M.O.L., 2021. High-permeability zones in folded and faulted silicified carbonate rocks – Implications for karstified carbonate reservoirs. Marine and Petroleum Geology 128, 105046. https://doi.org/10.1016/j.marpetgeo.2021.105046

Lavenu, A. P. C., Lamarche, J., 2018. What controls diffuse fractures in platform carbonates? Insights from Provence (France) and Apulia (Italy). Journal of Structural Geology. V. 108, pp. 94-107. https://doi.org/10.1016/j.jsg.2017.05.011.

Liao, Z., Liu, H., Carpenter, B. M., Marfurt, K. J., Reches, Z., 2019, Analysis of fault damage zones using three-dimensional seismic coherence in the Anadarko Basin, Oklahoma: The American Association of Petroleum Geologist, 103, 1771–1785, accessed 13 September 2022; DOI:10.1306/1219181413417207.

Liao, Z., Hu, L., Huang, X., Carpenter, B. M., Marfurt, K. J., Vasileva, S., Zhou, Y., 2020, Characterizing damage zones of normal faults using seismic variance in the Wangxuzhuang oil field, China: Interpretation, 8, 1-8, accessed 22 October 2022; http://dx.doi.org/10.1190/INT-2020-0004.1.

Libak, A., Behzad, A., Torabi, A., 2017, Fault visualization and identification in fault seismic attribute volumes: Implications for fault geometric characterization: Interpretation, 5; http://dx.doi.org/10.1190/INT-2016-0152.1

Ligtenberg, J. H., 2005, Detection of fluid migration pathways in seismic data: implications for fault seal analysis: Basin Research, 17, 141-153, accessed 13 September 2022; https://doi.org/10.1111/j.1365-2117.2005.00258.x.

Loveless, S., Bense, V., Turner, J., 2011. Fault architecture and deformation processes within poorly lithified rift sediments, Central Greece. Journal of Structural Geology 33, 1554 -1568. https://doi.org/10.1016/j.jsg.2011.09.008

Nicchio, M. A., Nogueira, F. C. C., Balsamo, F., Souza, J. A. B., Carvalho, B. R. B. M., Bezerra, F. H. R., 2018, Development of cataclastic foliation in deformation bands in

feldspar-rich conglomerates of the Rio do Peixe Basin, NE Brazil: Journal of Structural Geology, 107, 132-141, accessed 13 September 2022; doi:10.1016/j.jsg.2017.12.013.

Nicol, A., Walsh, J. J., Waterson, J., Bretan, P. G., 1995, Three-dimensional geometry and growth of conjugate normal faults, Journal of Structural Geology, 17, 847-862, http://dx.doi.org/10.1016/0191-8141(94)00109-D.

Nogueira, F. C. C., Nicchio, M. A., Balsamo, F., Souza, J. A. B., Silva, I. V. L., Bezerra, F. H. R., Vasconcelos, D. L., Carvalho, B. R. B. M., 2021, The influence of the cataclastic matrix on the petrophysical properties of deformation bands in arkosic sandstones: Marine and Petroleum Geology, **124**, 104825, accessed 13 October 2022; https://doi.org/10.1016/j.marpetgeo.2020.104825.

Ma, D., Wu, G., Scarselli, N., Luo, X., Han, J., Chen, Z., 2019, Seismic damage zone and width–throw scaling along the strike-slip faults in the Ordovician carbonates in the Tarim Basin: Petroleum Science, 16, 752-762, accessed 23 October 2022; https://doi.org/10.1007/s12182-019-0352-4.

Maciel, I. B., Dettori, A., Balsamo, F., Bezerra, F. H. R., Vieira, M. M., Nogueira, F. C. C., Salvioli-Mariani, E., Sousa J. A. B. 2018. Structural control on clay mineral authigenesis in faulted arkosic sandstone of the Rio do Peixe Basin, Brazil. Minerals 8, pp. 1-17, https://doi.org/10.3390/min8090408.

Mcquillan, H., 1974. Fracture Patterns on Kuh-E Asmari Anticline, Southwest Iran. AAPG Bull. 1177 58, 236–246. https://doi.org/10.1306/83D913C1-16C7-11D7-8645000102C1865D.

Mansfield C. S., Cartwright. J. A., 1996, High resolution fault displacement mapping from three-dimensional seismic data: evidence for dip linkage during fault growth: Journal of Structural Geology, 18, 249-263, accessed 13 September 2022; https://doi.org/10.1016/S0191-8141(96)80048-4.

Medeiros, W. E., do Nascimento, A. F., Alves da Silva, F. C., Destro, N., Demétrio, J. G. A., 2010. Evidence of hydraulic connectivity across deformation bands from field pumping

tests: Two examples from Tucano Basin, NE Brazil. Journal of Structural Geology 32, 1783–1791. https://doi.org/10.1016/j.jsg.2009.08.019

Morris, A. P., Ferrill, D. A., McGinnis, R. N., 2009. Mechanical stratigraphy and faulting in Cretaceous carbonates. AAPG Bulletin, v. 93, no. 11, p. 1459–1470. doi: 10.1306/04080909011.

Silva, M. E., Nogueira, F. C. C., Pérez, Y. A. R., Vasconcelos, D. L., Stohler, R. C., Sanglard, J. C. D., Balsamo, F., Bezerra, F. H. R., Carvalho, B. R. B. M., Souza, J. A. B., 2022. Permeability modeling of a basin-bounding fault damage zone in the Rio do Peixe Basin, Brazil. Marine and Petroleum Geology. V. 135, 105409. https://doi.org/10.1016/j.marpetgeo.2021.105409.

Souza, D. H. S., Nogueira, F. C. C., Vasconcelos, D. L. Torabi, A., Souza, J. A. B., Nicchio, M. A., Pérez, Y. A. R., Balsamo, F., 2021, Growth of cataclastic bands into a fault zone: A multiscalar process by microcrack coalescence in sandstones of Rio do Peixe Basin, NE Brazil: Journal of Structural Geology, 146, 104315; https://doi.org/10.1016/j.jsg.2021.104315.

Pontes, C. C. C., Nogueira, F. C. C., Bezerra, F. H. R., Balsamo, F., Miranda, T. S., Nicchio, M. A., Souza, J. A. B., Carvalho, B. R. B. M., 2019, Petrophysical properties of deformation bands in high porous sandstones across fault zones in the Rio do Peixe Basin, Brazil: International Journal of Rock Mechanics and Mining Sciences, 114, 153-163, accessed 13 September 2022; https://doi.org/10.1016/j.ijrmms.2018.12.009.

Pontes, C., Bezerra, F.H., Bertotti, G., Balsamo, F., La, V., Hoop, S. De, 2020. Karst conduits formed along fracture corridors in anticline hinges of carbonate units – implications for reservoir quality.

Pontes, C. C. C., Bezerra, F. H. R., Bertotti, G., La Bruna, V., Audra, P., De Waela, J., Auler, A. S., Balsamo, F., De Hoop, S., Pisani, L., 2021. Flow pathways in multiple-direction fold hinges: Implications for fractured and karstified carbonate reservoirs. Journal of Structural Geology. V. 146, 104324. https://doi.org/10.1016/j.jsg.2021.104324.

Preuss, S., Herrendörfer, R.,Gerya, T. V., Ampuero, J.-P., &van Dinther, Y., 2019, Seismic and aseismic fault growth lead to different fault orientations: Journal of Geophysical Research: Solid Earth, 124, 8867–8889, accessed 13 September 2022; https://doi.org/10.1029/2019JB017324.

Purves, S., Alaei, B., Larsen. E., 2018, Bootstrapping Machine-Learning based seismic fault interpretation: ACE 2018 Annual Convention, accessed 13 September 2022; http://www.searchanddiscovery.com/abstracts/html/2018/ace2018/abstracts/2856016.html.

Qi, J., B. Lyu, A. Alali, G. Machado, Y. Hu, and K. J. Marfurt, 2019, Image processing of seismic attributes for automatic fault extraction: Geophysics, 84, 25–37.

Roche, V., Homberg, C., Rocher, M., 2013. Fault nucleation, restriction, and aspect ratio in layered sections: Quantification of the strength and stiffness roles using numerical modeling. J. Geophys. Res., Solid Earth, 118, 1–15. doi: 10.1002/jgrb.50279.

Torabi, A., Balsamo, F., Nogueira, F. C. C., Vasconcelos, D. L., Silva, A. C. E., Bezerra, F. H. R., Souza, J. A. B., 2021, Variation of thickness, internal structure and petrophysical properties in a deformation band fault zone in siliciclastic rocks: Marine and Petroleum Geology, 133, 105297, accessed 13 September 2022; https://doi.org/10.1016/j.marpetgeo.2021.105297.

Zahm, C. K., Hennings, P. H., 2009.Complex fracture development related to stratigraphic architecture: Challenges for structural deformation prediction, Tensleep Sandstone at the Alcova anticline, Wyoming. AAPG Bulletin, V. 93, No. 11. doi: 10.1306/08040909110.

Walsh, J. J. & Watterson, J. 1987, Distributions of cumulative dis-placement and seismic slip on a single normal fault surface: Journal of Structural Geology 9, 1039-1046, accessed 13 September 2022; https://doi.org/10.1016/0191-8141(87)90012-5.

Wrona, T. Pan, I., Bell, R. E., Gawthorpe, R. L., Fossen, H., Brune, S., 2021, 3D seismic interpretation with deep learning: A brief introduction: The Leading Edge 40, 524–532, accessed 13 September 2022; https://doi.org/10.1190/tle40070524.1

Wu, H., Zhang, B., 2018, A deep convolutional encoder-decoder neural network in assisting seismic horizon tracking, accessed 13 September 2022; https://doi.org/10.48550/arXiv.1804.06814.

Wu, X., Liang, L., Shi, Y., Fomel, S., 2019b, FaultSeg3D: Using synthetic data sets to train an end-to-end convolutional neural network for 3D seismic fault segmentation: Geophysics, 84, 35-45, accessed 13 September 2022; http://dx.doi.org/10.1190/geo2018-0646.1.

Capítulo 2

Contexto Geológico

2 Contexto Geológico

2.1 Bacia Rio do Peixe – Arcabouço Estrutural e Estratigráfico

A área de estudo desta tese está localizada na Bacia do Rio do Peixe (BRP) (Figura 2), a qual é uma bacia intracontinental que faz parte do grupo de bacias sedimentares do nordeste do Brasil. Tais bacias intracontinentais estão inseridas sobre a Província Borborema, sendo essa composta por diferentes porções de rocha oriundas de faixas orogênicas arqueanas e neoproterozóicas, do embasamento e até de microcontinentes anteriores (Brito Neves et al., 2000). Esse grande bloco rochoso que embasa as bacias interiores limita-se de um complexo estrutural de lineamentos que são as zonas de cisalhamento de orientação preferencial E-W e NE-SW, as quais são resultantes da Orogenia Brasiliana (De Castro et al., 2012; Bezerra et al., 2014). Nesse ínterim, as bacias interiores do nordeste do Brasil têm origem num processo de abertura do oceano atlântico sul, em que esses lineamentos sofreram reativações rúpteis, gerando regimes de transcorrência que se desenvolveram nesses grabéns e semi-grábens (e.g., De Castro et al., 2007; Nogueira et al., 2015; Vasconcelos et al., 2020).

Fazendo parte desse contexto, a BRP herdou a geometria das zonas de cisalhamento pré-cambrianas com direções de orientação NE-SW e E-W devido a sua reativação rúptil (Matos, 1992; Brito Neves et al., 2000) (Figura 2A). Com isso, a BRP está estruturalmente baseada nas falhas: Rio Piranhas (NE-NW), Portalegre (NE-SW), e Malta (E-W); as quais apresentam os mesmos *trends* estruturais das zonas de cisalhamento de Portalegre e Patos (Sénant e Popoff, 1991; Françolin et al., 1994). Ainda sobre a tectônica da bacia, Nogueira et al. (2015) e Vasconcelos et al. (2020) identificaram duas fases tectônicas principais como sin-rift e pós-rift, as quais foram

responsáveis pela geração da bacia durante o processamento de extensão, criando as falhas com orientação E-W e NE-SW, assim como a inversão tectônica da bacia como resposta a compressão ENE-WNW. Mais recentemente foram utilizados dados paleomagnéticos para concluir que duas direções de abertura mudaram gradualmente de NNE-SSW para NW-SE durante o desenvolvimento da bacia (início do Cretáceo), como consequência da rotação no sentido horário da América do Sul (Nicchio et al., 2022).

Em relação ao seu arcabouço estratigráfico (Figura 2B), a BRP é composta pelas sub-bacias Brejo das Freiras, Sousa e Pombal, possuindo os grupos-estratigráficos que se apresentam de baixo pra cima: grupo Santa Helena contendo formações Devonianas (Formações Triunfo e Pilões), e o grupo Rio do Peixe que contém as formações Cretáceas Inferiores (Formações Antenor Navarro, Sousa, Rio piranhas) (Córboda et al., 2008; Françolin et al.,1994; Sénant e Popoff, 1991; Roesner et al., 2011; Silva et al., 2014). A Formação Pilões consiste predominantemente de siltitos e argilitos relacionados a ambientes de deposição deltaica a fluvial, e esses estão sobrepostos pela Formação Triunfo, a qual é composta principalmente de arenitos e conglomerados fluvio-deltaicos de coloração cinza a branco. A Formação Antenor Navarro é descrita como ambiente de fluvial fino que é composta de conglomerados e arenitos conglomerados. Sobrepondo a Formação Antenor Navarro está a Formação Sousa, sendo composta de unidades lacustres com intercalações de argilas e siltes. No topo, a Formação Rio Piranhas é composta predominantemente de conglomerados relacionados a leques aluviais.

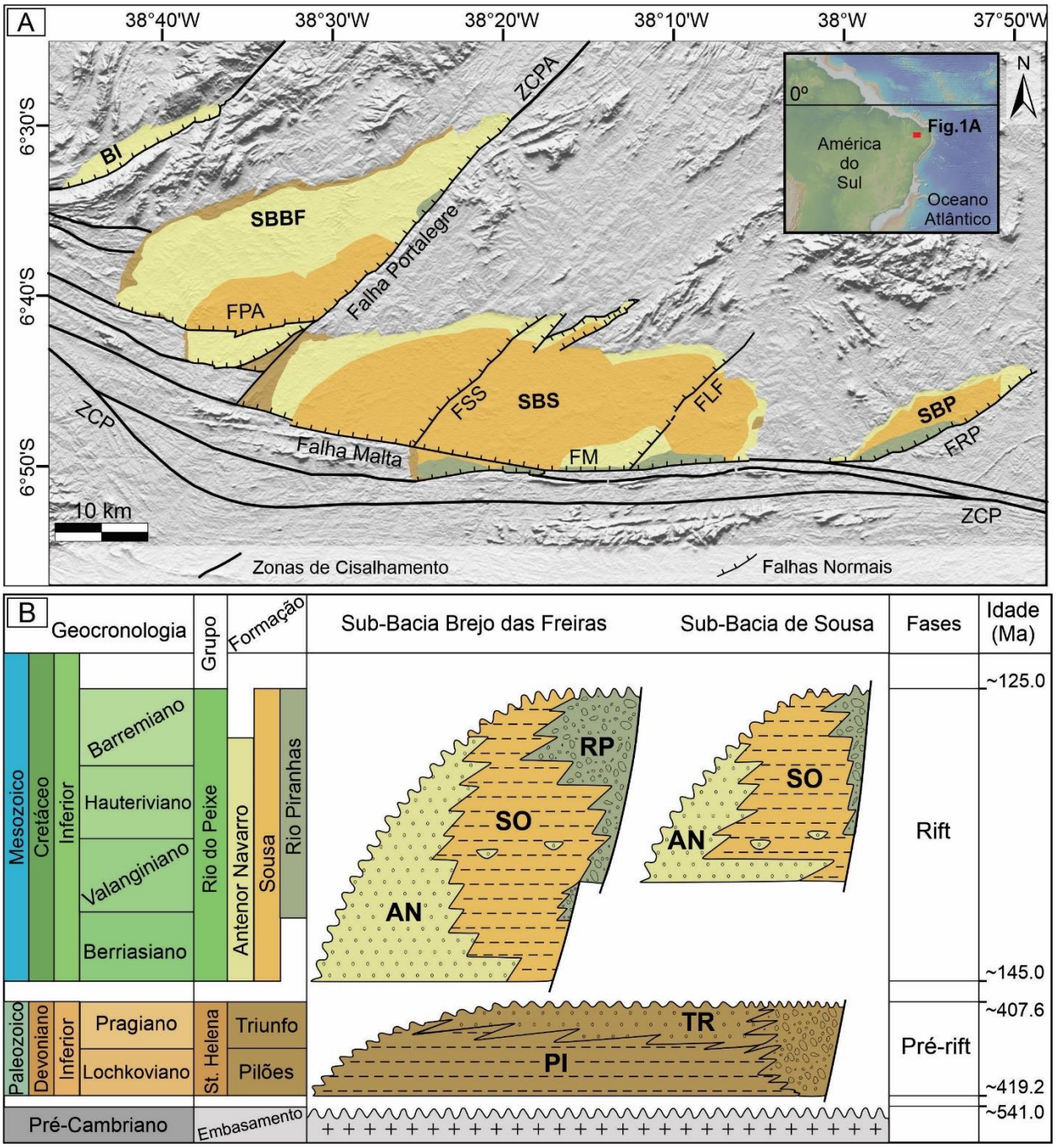

Figura 2 – (A) Mapa Geológico da BRP com estruturas e zonas de cisalhamento e (B) Carta estratigráfica da carta estratigrafica da BRP. Mapa adaptado de Françolin et al., 1994, Medeiros et al., 2005, Vasconcelos et al., 2021; Ramos et al., 2022. Carta estratigráfica modificada de Rapozo et al., 2022 e Ramos et al., 2022. Abreviações: BI, Bacia de Icozinho; SBBF, Sub-Bacia Brejo das Freiras; SBS, Sub-Bacia de Sousa; SBP, Sub-Bacia Pombal; ZCPA, Zona de Cisalhamento Portalegre; ZCP, Zona de Cisalhamento Patos; FSS, Falha Sítio Sagui; FM, Falha Malta; FPA, Falha Portalegre; FLF, Falha Lagoa do Forno; FRP, Falha Rio Piranhas.

2.2 Bandas de Deformação na BRP

Estudos recentes na RPB abordaram as bandas de deformação e a influência dessas estruturas nas propriedades petrofísicas da rocha hospedeira (e.g, Araujo et al., 2018; Maciel et al., 2018; Nicchio et al., 2018; Pontes et al., 2019; Souza et al., 2021; Nogueira et al., 2021; Torabi et al., 2021; Silva et al., 2022). Estes estudos propuseram que os processos de coalescência em microescala (microcracks) e de cataclase (como por exemplo: redução do tamanho dos grãos e cominuição das bordas dos grãos) são os principais mecanismos de deformação responsáveis pelo desenvolvimento da banda de deformação (Nicchio et al., 2018; de Souza et al., 2021). Além disso, dois tipos de zonas de falha são propostos na RPB: (i) zona de falha típica e (ii) zona de falha da banda de deformação (Araujo et al., 2018; Torabi et al., 2021; Silva et al., 2022). A diferença entre esses dois tipos de zona se distingue basicamente em o tipo (i) ser um núcleo de falha clássico, e o tipo (ii) seria como uma superfície de escorregamento principal. Em uma descrição mais resumida, o tipo (i) de zona de falha típica possui o plano de falha envolto de seus elementos arquiteturais, tendo, portanto, o núcleo de falha espacialmente definido. Em contrapartida, o tipo (ii) – zona de falha da banda de deformação – não se reconhece espacialmente a definição de um núcleo de falha, porém há uma maior concentração das bandas como em clusters, e o deslocamento da falha evidenciado por uma superfície de deslizamento principal. Em relação a disposição dessas estruturas, foi registrada uma diminuição logarítmica na frequência das bandas de deformação se afastando do núcleo da falha, para ambos tipos de zona de falha. Outro parâmetro que controla a distribuição espacial das bandas de deformação é o tamanho médio de grãos, que evidenciam que essas estruturas estão agrupadas

preferencialmente em arenitos grossos (Araujo et al., 2018). Em relação as alterações das propriedades petrofísicas, a resistência das rochas é três vezes maior nas zonas de falha com vários núcleos de falha do que nas zonas de falha com um único núcleo de falha, e quatro vezes maior do que as unidades não deformadas (Pontes et al., 2019). Além disso, uma redução de permeabilidade de até três ordens de magnitude e uma redução de porosidade de até duas ordens de magnitude foram registradas nas bandas de deformação em comparação com a rocha hospedeira (Pontes et al., 2019; Torabi et al., 2021; Silva et al., 2022). Assim como, em relação a intensidade da deformação cataclástica baseada na quantidade de matriz, registra-se uma redução na permeabilidade e porosidade atingindo até cinco e duas ordens de magnitude, respectivamente, em comparação com arenitos não deformados (Nogueira et al., 2021).

Referências:

Araujo, R. E. B., Bezerra, F. H. R., Nogueira, F. C. C., Carvalho, B. R. B. M., Souza, J. A. B., Sanglard, J. C. D., de Castro, D. L., Melo, A. C. C., 2018, Basement control on fault formation and deformation band damage zone evolution in the Rio do Peixe Basin, Brazil: Tectonophysics, 745, 117-131, accessed 13 September 2022; https://doi.org/10.1016/j.tecto.2018.08.011.

Bezerra, F.H.R., Rossetti, D.F., Oliveira, R.G., Medeiros, W.E., Brito Neves, B.B., Balsamo, F., Nogueira, F.C.C., Dantas, E.L., Aandrades Filho, C., Góes, A.M., 2014. Neotectonic reactivation of shear zones and implications for faulting style and geometry in the continental margin of NE Brazil. Tectonophysics 614, 78–90.

Brito Neves, B.B., Santos, E.J., Van Schmus, W.R., 2000. Tectonic history of the Borborema Province, northeastern Brazil. In: Cordani, U., Milani, E.J., Thomaz Filho, A., Campos, D.A. (Eds.), Tectonic Evolution of South America: Proceedings of the 31st International Geological Congress, Rio de Janeiro, 151–182.

Córdoba V. C., Antunes A. F., Jardim de Sá E. F., Nunes da Silva A., Sousa D. C., Lins F. A. P. L., 2008, Análise estratigráfica e estrutural da Bacia do Rio do Peixe Nordeste do Brasil: integração de dados a partir do levantamento sísmico pioneiro: Boletim de Geociências da Petrobras, 16, 53-68.

De Castro, D. L., Oliveira, D. C., Castelo Branco, R. M. G., 2007. On the tectonics of the Neocomian Rio do Peixe Rift Basin, NE Brazil: Lessons from gravity, magnetics, and radiometric data. J South Am Earth Sci. 24 (2–4): 184–202. https://doi.org/10.1016/j.jsames.2007.04.001.

De Castro, D. L., Bezerra, F. H. R., Souza, M. O. L., Fuck, R. A., 2012, Influence of Neoproterozoic tectonic fabric on the origin of the Potiguar Basin, northeastern Brazil and its links with West Africa based on gravity and magnetic data: Journal of Geodynamics, 54, 29-42. doi:10.1016/j.jog.2011.09.002.

Françolin, J. B. L., Cobbold, P. R., Szatmari, P., 1994. Faulting in the Early Cretaceous Rio do Peixe (NE Brazil) and its significance for the opening of the Atlantic. Journal of Structural Geology, v. 16, p. 647-661. https://doi.org/10.1016/0191-8141(94)90116-3.

Nicchio, M. A., Nogueira, F. C. C., Balsamo, F., Souza, J. A. B., Carvalho, B. R. B. M., Bezerra, F. H. R., 2018, Development of cataclastic foliation in deformation bands in feldspar-rich conglomerates of the Rio do Peixe Basin, NE Brazil: Journal of Structural Geology, 107, 132-141, accessed 13 September 2022; doi:10.1016/j.jsg.2017.12.013.

Nicchio, M. A., Balsamo, F., Cifelli, F., Nogueira, F. C. C., Aldega, L., Bezerra, F. H. R., Vasconcelos, D. L., Souza, J. A. B., 2022, An Integrated Structural and Magnetic Fabric Study to Constrain the Progressive Extensional Tectonics of the Rio do Peixe Basin, Brazil: Tectonics, **41**, accessed 17 Octuber 2022; https://doi.org/10.1029/2022TC007244.

Nogueira, F. C. C., Nicchio, M. A., Balsamo, F., Souza, J. A. B., Silva, I. V. L., Bezerra, F. H. R., Vasconcelos, D. L., Carvalho, B. R. B. M., 2021, The influence of the cataclastic matrix on the petrophysical properties of deformation bands in arkosic sandstones: Marine and Petroleum Geology, 124, 104825, accessed 13 October 2022; https://doi.org/10.1016/j.marpetgeo.2020.104825.

Nogueira, F. C. C., Nicchio, M. A., Balsamo, F., Souza, J. A. B., Silva, I. V. L., Bezerra, F. H. R., Vasconcelos, D. L., Carvalho, B. R. B. M., 2021. The influence of the cataclastic matrix on the petrophysical properties of deformation bands in arkosic sandstones. Marine and Petroleum Geology. https://doi.org/10.1016/j.marpetgeo.2020.104825.

Matos, R. M. D., 1992. The northeastern Brazilian Rift System. Tectonics 11 (4), 766–791. https://doi.org/10.1029/91TC03092.

Ramos, G. V., Vasconcelos, D. L., Marques, F. O., de Castro, D. L., Nogueira, F, C. C., Bezerra, F. H. R., Perez, Y. A. R., Souza, J. A. B., Medeiros, V. C., 2022, Relations between inherited basement fabric and fault nucleation in a continental setting: The Rio do Peixe Basin, NE Brazil: Marine and Petroleum Geology, 139, 105635, accessed 13 September 2022, https://doi.org/10.1016/j.marpetgeo.2022.105635.

Rapozo, B. F., Córdoba, V. C., Antunes, A. F., 2021.Tectono-stratigraphic evolution of a cretaceous intracontinental rift: Example from Rio do Peixe Basin, north-eastern Brazil. Marine and Petroleum Geology 126, 104899. https://doi.org/10.1016/j.marpetgeo.2021.104899.

Roesner, H. E., Lana, C. C., Le Herissé, A., Melo, J. H. G., 2011, Bacia do Rio do Peixe (PB): Novos resultados biocronoestratigráficos e paleoambientais. In: Carvalho I.S. et al. (eds.) Paleontologia: Cenários de Vida, 3: 135-141.

Sénant, J., Popoff, M., 1991. Early Cretaceous extension in northeast Brazil related to the South Atlantic opening. Tectonophysics, 198, 35–46.

Silva, J. G. F., Córdoba, V. C., Caldas, L. H. C., 2014, Proposta de novas unidades litoestratigráficas para o Devoniano da Bacia do Rio do Peixe, Nordeste 44, 561-578, accessed 13 September 2022; doi:10.5327/Z23174889201400040004.

Silva, M. E., Nogueira, F. C. C., Pérez, Y. A. R., Vasconcelos, D. L., Stohler, R. C., Sanglard, J. C. D., Balsamo, F., Bezerra, F. H. R., Carvalho, B. R. B. M., Souza, J. A. B., 2022. Permeability modeling of a basin-bounding fault damage zone in the Rio do Peixe Basin, Brazil. Marine and Petroleum Geology. V. 135, 105409. https://doi.org/10.1016/j.marpetgeo.2021.105409.

Souza, D. H. S., Nogueira, F. C. C., Vasconcelos, D. L. Torabi, A., Souza, J. A. B., Nicchio, M. A., Pérez, Y. A. R., Balsamo, F., 2021, Growth of cataclastic bands into a fault zone: A multiscalar process by microcrack coalescence in sandstones of Rio do Peixe Basin, NE Brazil: Journal of Structural Geology, 146, 104315; https://doi.org/10.1016/j.jsg.2021.104315.

Pontes, C. C. C., Nogueira, F. C. C., Bezerra, F. H. R., Balsamo, F., Miranda, T. S., Nicchio, M. A., Souza, J. A. B., Carvalho, B. R. B. M., 2019, Petrophysical properties of deformation bands in high porous sandstones across fault zones in the Rio do Peixe Basin, Brazil: International Journal of Rock Mechanics and Mining Sciences, 114, 153-163, accessed 13 September 2022; https://doi.org/10.1016/j.ijrmms.2018.12.009.

Torabi, A., Balsamo, F., Nogueira, F. C. C., Vasconcelos, D. L., Silva, A. C. E., Bezerra, F. H. R., Souza, J. A. B., 2021, Variation of thickness, internal structure and petrophysical properties in a deformation band fault zone in siliciclastic rocks: Marine and Petroleum Geology, 133, 105297, accessed 13 September 2022; https://doi.org/10.1016/j.marpetgeo.2021.105297.

Capítulo 3

Referencial Teórico

3 Referencial Teórico

Nesse capítulo serão apresentados em síntese os conceitos e definições acerca de: (1) zona de falhas e bandas de deformação, (2) estratigrafia mecânica, e (3) as bases conceituais da detecção de falhas utilizando dados de sísmica de reflexão.

3.1 Zona de falha e bandas de deformação

Processos geológicos formadores de estruturas tectônicas que ocorrem na escala mais rasa da terra são compreendidos dentro do regime rúptil. Nesse contexto, as falhas são estruturas extensas, complexas e volumétricas que deformam o protólito, o qual é a rocha que hospeda essa deformação. Espacialmente, as zonas de falhas são compostas por elementos arquiteturais representados por: núcleo de falha e a zona de dano (Heynekamp et al., 1999; Caine e Minor, 2009) (Figura 3).

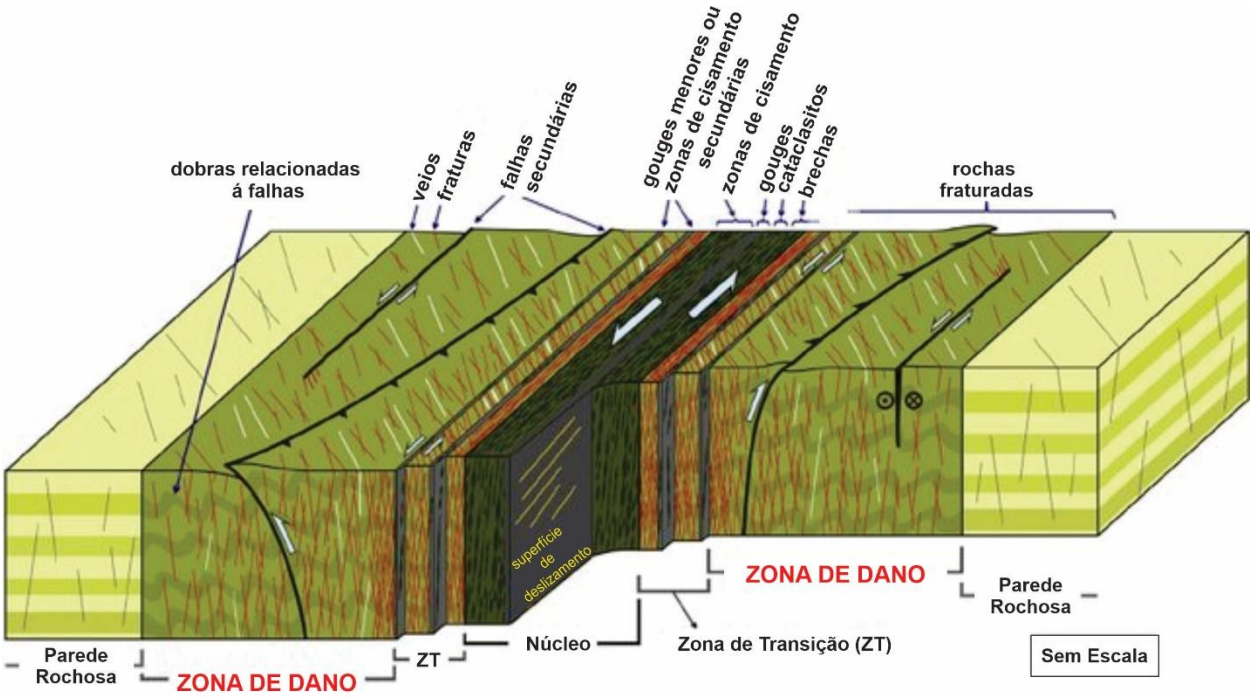

Figura 3 – Modelo esquemático de zona de falha e seus elementos arquiteturais, representadas a zona de dano, núcleo de falha e rocha hospedeira (modificado de Choi et al., 2016).

Em relação a disposição espacial desses elementos arquiteturais, a zona de dano localiza-se ao redor do núcleo da falha e se define com uma zona volumétrica de rochas compostas por diferentes tipos de estruturas deformacionais secundárias que podem se apresentar como fraturas menores, veios, dobras, bandas de deformação e fraturas (Caine et al., 1996; Choi et al., 2016). Nesse ínterim, o núcleo da falha pode ser compreendido como uma porção da zona de falha com estrutura, litologia e forma definidas, onde está localizado o plano de superfície da falha (ou superfície de deslizamento principal) e local do cisalhamento mais intenso, e, consequentemente, o maior rejeito da zona de falha (Caine et al., 1996; Fossen et al., 2010).

Zonas de falhas são estruturas complexas que podem ser compostas por rochas originadas durante o desenvolvimento dessa deformação, podendo apresentar brechas, gouges ou zonas cataclásticas fortemente endurecidas (Anderson et al., 1983; Sibson, 1977; Caine et al., 1996). As rochas formadas pela deformação dessas estruturas são conhecidas como rochas de falha, tendo textura e estrutura alterada em comparação a rocha que a hospeda (Sibson, 1977). Essas zonas podem ser classificadas em zonas de alta e baixa tensão/estiramento, em que a zona de maior estiramento é representada pelo núcleo da falha e aonde estão localizados o maior rejeito e deformação, ambos acomodados pela rocha hospedeira (Caine et al., 1996; Schultz e Fossen, 2008; Braathen et al., 2009; Childs et al., 2009; Torabi e Berg, 2011). Nesse processo, comprimento de um núcleo de falha pode variar de milímetros de espessura, representado por uma única superfície de deslizamento, a até uma zona intensamente cisalhada contendo superfícies de deslizamento mais desenvolvidas, na escala de metros de espessura. Em rochas siliciclásticas, o processo de falhamento pode

compreender a acomodação da deformação gerando estruturas secundárias como as bandas de deformação (Aydin and Johnson, 1978). As bandas de deformação podem evoluir no processo de deformação da falha e se tornar um tipo de falha denominada de '*deformation band fault'*, em que se compreende em uma superfície de deslizamento principal conjuntamente com clusters de bandas de deformação onde se localiza o resultado de uma deformação progressiva (Shipton et al., 2005; Torabi et al., 2021). De forma distinta, zonas de falha com bandas de deformação podem se apresentar como: falhas com largas zonas de dano contendo bandas de deformações dispersas espacialmente em dezenas de metros, incorporadas a clusters de bandas; falhas com núcleos bem desenvolvidos (espessura de até 1 metro) com bandas de deformação espalhadas espacialmente, demonstrando menor correlação entre a frequência das estruturas com o deslocamento da falha; e falhas reconhecidas através da maior frequência de bandas de deformação se aglomerando em clusters (Torabi et al., 2021). Portanto, uma zona de falha pode se apresentar uma correlação complexa em relação ao rejeito e espessura, podendo deslocar-se em dezenas às centenas de metros e localizar a deformação gerada por esse em diferentes dimensões espaciais, sendo essa composição de forma distinta em zonas de danos com bandas de deformação, núcleo e *slip surfaces*.

Ocorrendo mais comumente em arenitos porosos, as bandas de deformação foram descritas como estruturas planares com uma porosidade condicional de formação sendo igual ou superior a 15% (Aydin, 1978; Fossen et al., 2007). Contendo milímetros de espessura, essas estruturas deslocam na ordem de alguns milímetros a centímetros (Aydin e Jonhson, 1978). Além disso, as bandas de deformação possuem diferentes

estágios de deformação, podendo evoluir e se formar tanto em rochas como em sedimentos, com a condição de ter porosidade suficiente para ocorrer os processos de rotação, translação e quebra de grãos. O espaço de acomodação para esses tipos de deformação, descritos anteriormente, se mostra fundamental no processo de formação dessas estruturas, já que sem esse espaço são formadas estruturas como fraturas, estilólitos ou até superfícies de deslizamento (Fossen, et al., 2007).

Além dessas condições, há alguns fatores variáveis que também controlam o aparecimento das bandas deformação tais como: pressão confinante, ambiente tectônico, pressão de fluido dos poros, grau de litificação e mineralogia da rocha hospedeira, e parâmetros sedimentares como granulometria, selecionamento e formato de grão (Fossen et al., 2007). A presença dessas estruturas num reservatório pode alterar a produção de petróleo, uma vez que influenciam na porosidade e permeabilidade do sistema (Torabi e Alikarami, 2012).

Ao longo dos anos, as bandas de deformação foram classificadas por ordem de ocorrência (Aydin e Jonhson, 1978) – individuais, aglomerado e superfície de deslizamento; e por mecanismo de formação (Fossen et al., 2007) – fluxo cataclástico (moagem e fraturamento de grãos) que gera bandas de desagregação, fluxo granular (deslizamento e rotação de grãos) que forma bandas cataclásticas, lubrificação filossilicática que originam bandas filossilicáticas, e dissolução e cimentação que correlacionam-se a bandas de dissolução e cimentação, respectivamente. Além dessas, há também a classificação cinemática dessas estruturas, em que se apresentam as bandas de dilatação, cisalhamento, compactação ou por uma mistura desses tipos que varia de acordo com o principal componente cinemático (Figura 4) (Fossen et al., 2007).

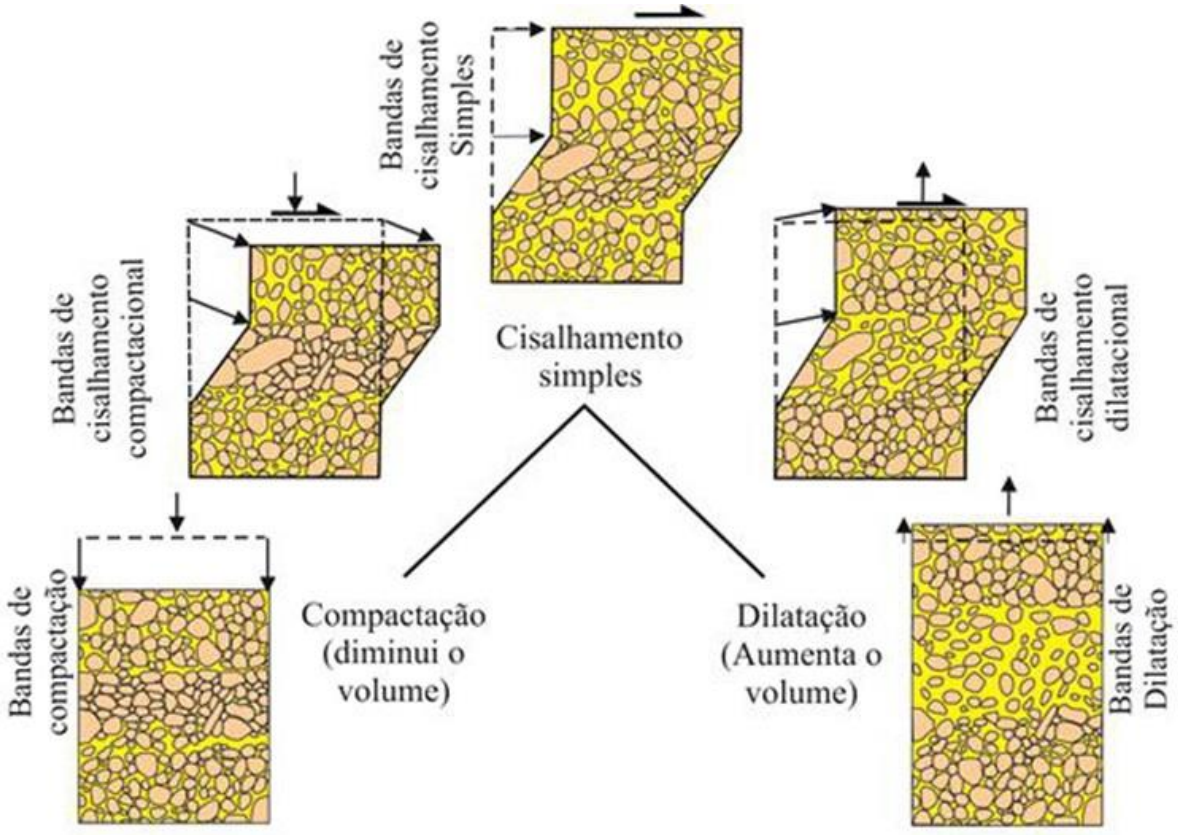

Figura 4 - Classificação cinemática de bandas de deformação, descrita por Fossen et al., 2007.

3.2 Estratigrafia Mecânica

Zonas de falhas contendo fraturas são foco de análise e estudo desde a escala de afloramento à compreensão de reservatórios, uma vez que essas estruturas podem controlar o fluxo de fluidos atuando como condutos e armadilha para esses. Dentro desse contexto, compreende-se que as estruturas podem se diferenciar em relação a dimensão, intensidade e propagação da deformação conforme a reologia da rocha afetada, assim como parâmetros mecânicos que controlam essa alteração na rocha. Nesse ínterim, tem-se o conceito da estratigrafia mecânica que foi inicialmente compreendida como a relação entre a espessura das camadas e a intensidade do processo de fraturamento (e.g., McQuillan, 1974; Bai e Pollard, 2000; Cooke et al., 2006;

Zahm et al., 2009). A estratigrafia mecânica elucida acerca da compreensão da deformação de uma falha e suas estruturas secundárias que se propagam cruzando camadas de rochas (e.g., Bertotti et al., 2007; Ferrill e Morris, 2008; Laubach et al., 2009; Roche et al., 2013; Ferrill et al., 2017;).

Dentro da estratigrafia mecânica tem-se os conceitos de unidades e interfaces mecânicas (Figura 5), as quais são definidas tais como: (1) unidade mecânica - sendo um agrupamento de camadas que permitem a propagação de estruturas rúpteis; ocorrendo o processo oposto para (2) as interfaces mecânicas - que podem ser compreendidas como camadas de rocha que impedem a passagem da deformação, e consequentemente, a presença de estruturas como fraturas (Cooke et al., 2006).

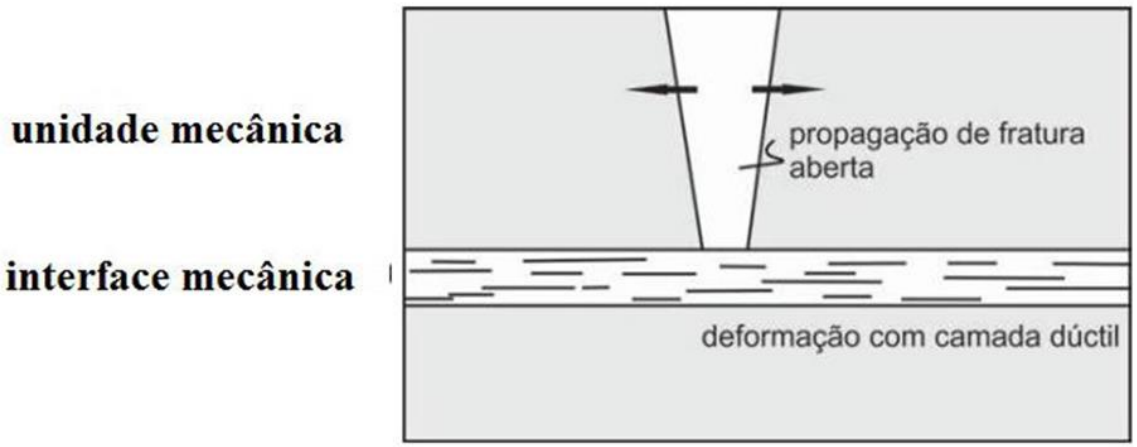

Figura 5 – Ilustração evidenciando a propagação da deformação através das camadas sedimentares, destacando a unidade e interface mecânica. Modificado de Cooke et al, 2006.

Ferril et al. (2017) realizaram uma revisão sobre os parâmetros considerados relevantes nas análises mecânico-estratigráficas e concluíram que as unidades mecânicas são determinadas pelo número, intensidade e espaçamento de fraturas, bem

como pela competência e resistência mecânica dos estratos, além das mudanças de mergulho e da predominância de direções.

Diante da diversidade de tipo de rochas afetadas pela deformação e das diferentes estruturas que as atingem, pode-se entender a análise dessa relação como o enfoque da estratigrafia mecânica, na qual investiga a relação entre a reologia de camadas sedimentares e a intensidade das fraturas (e.g., Mcquillan, 1974; Bai e Pollard, 2000; Bertotti et al., 2007; Cooke et al., 2006; Zahm e Hennings, 2009; Lavenu e Lamarche, 2018). Mais recentemente, a estratigrafia mecânica compreendeu parâmetros como a propriedades mecânicas da rocha hospedeira, as propriedades de fricção entre os limites mecânicos de uma camada rochosa e outra, e ainda a comparação da espessura das camadas (Ferrill et al.,2017). Com isso, a densidade de parâmetros para a compreensão do comportamento mecânico de cada camada por ser observado através das forças de compressão e tração (módulo de Young), a composição litológica e até processos secundários como de mineralização e dissolução das estruturas. Ainda, são considerados as disposições espaciais das estruturas que afetam as camadas de rocha, analisando assim a geometria das falhas, características de *linkagem*, nucleação e crescimento dessas estruturas, frequência e ângulo de mergulho das estruturas nas camadas sedimentares (Ferrill e Morris, 2003; Ferrill e Morris, 2008; Morris et al., 2009b; Roche et al.,2013).

3.3 Interpretação estrutural em dados de sísmica de reflexão

A intepretação sísmica com o foco em mapear estruturas, como falhas e superfícies estratigráficas, vem sendo fundamental para a compreensão das bacias

sedimentares ao longo da história da indústria do petróleo e gás (Hustoft et al., 2007). Na caracterização de reservatórios de hidrocarbonetos, estudos diversos vem caracterizando a conectividade dos corpos geológicos e suas extensões através do mapeamento convencional com a interpretação sísmica manual (Maul, 2005). Nesse contexto, diversas técnicas foram sendo criadas e desenvolvidas para otimizar a interpretação de feições geológicas através de dados sísmicos. No progresso da sismologia de reflexão, alguns estudos vêm utilizando de algoritmos como os atributos sísmicos com foco no imageamento e detecção de zonas de falhas e suas estruturas internas, incorporando dados de poço juntamente das propriedades dessas rochas (e.g Bahorich e Farmer, 1995; Chopra e Marfurt, 2007; Cohen et al., 2006; Xu e Sun, 2014; Yuan e Wang, 2013; Botter et al., 2014, 2016; Roden et al., 2015; Iacopini et al., 2016; Machado et al., 2016; Alaei and Torabi, 2017).

Os atributos sísmicos podem ser medidos ao longo de um único traço sísmico ou através de uma sequência de traços numa janela de interpretação definida. Em síntese, os atributos sísmicos podem se dar por mudanças na fase, frequência, impedância acústica, velocidade e polaridade dos dados sísmicos (Dorn, 1998). Em outras palavras, um atributo sísmico é uma quantidade extraída ou oriunda dos dados sísmicos que podem ser analisados para melhorar as imagens tradicionais que interpretamos da imagem sísmica. Historicamente, os primeiros atributos sísmicos estão relacionados a um traço sísmico em 1D, evoluindo a extração de zonas de falhas e *geobodies* em 3D nos dias de hoje. Alguns exemplos de atributos sísmicos amplamente utilizados são: coerência, azimute, dip, amplitude instantânea, resposta de amplitude,

resposta de fase, AVO e decomposição espectral. Brown (1996) classifica os atributos sísmicos os agrupando em tempo, amplitude, frequência e atenuação (Figura 6).

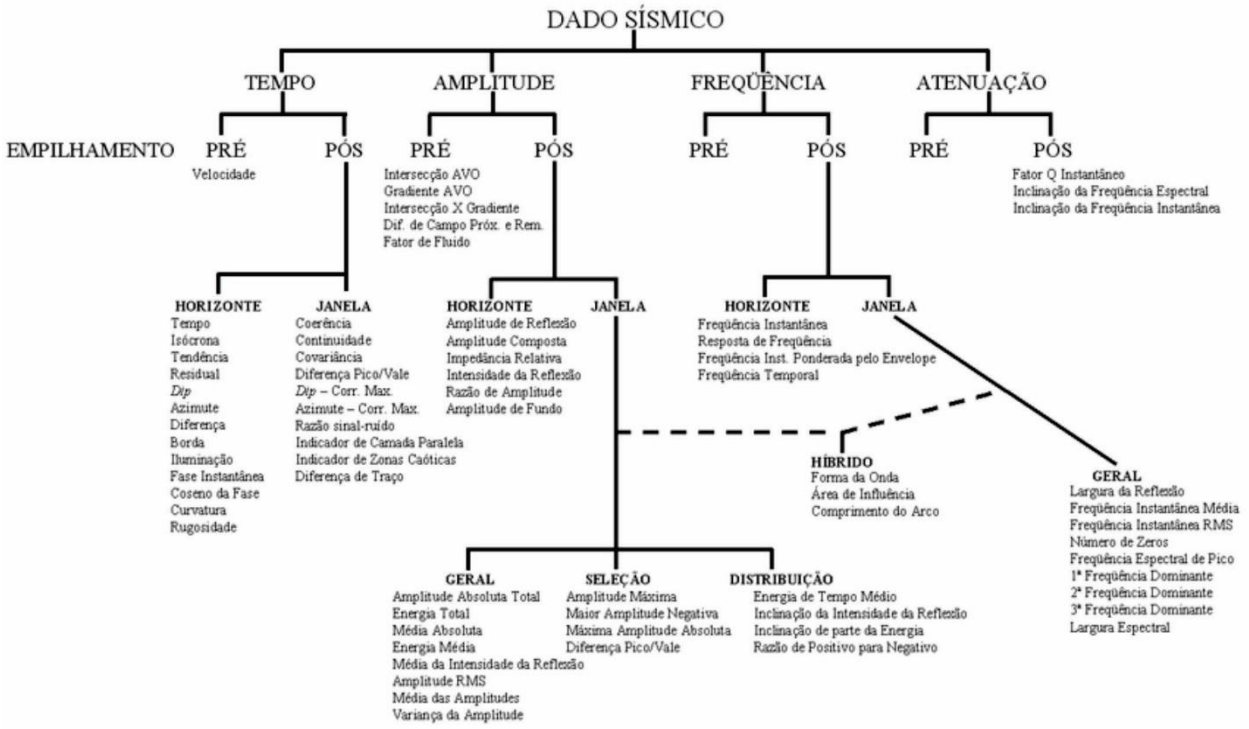

Figura 6 - Classificação dos atributos sísmicos por Brown, 1996. Tradução retirada de Maul, 2005.

Existem vários atributos sísmicos utilizados com as mais diversas aplicações na interpretação de feições geológicas, porém na presente Tese utilizamos atributos que destacam as descontinuidades entre os horizontes e que embasaram a detecção automática de falhas, dos quais são apresentadas as respectivas metodologias detalhadamente na seção dos resultados. Para a geração de resultados na interpretação automática de falhas, utilizamos atributos nomeados de Similarity, Ant Tracking, Variance, Fault Enhancement, os quais foram aplicados nos dados de sísmica de reflexão da Bacia Rio do Peixe. Ambos atributos são comumente utilizados para revelar zonas de falhas em diversos estudos recentes (Figura 7) (Odoh et al., 2014; Liao et al., 2020; Mousavi et al., 2022).

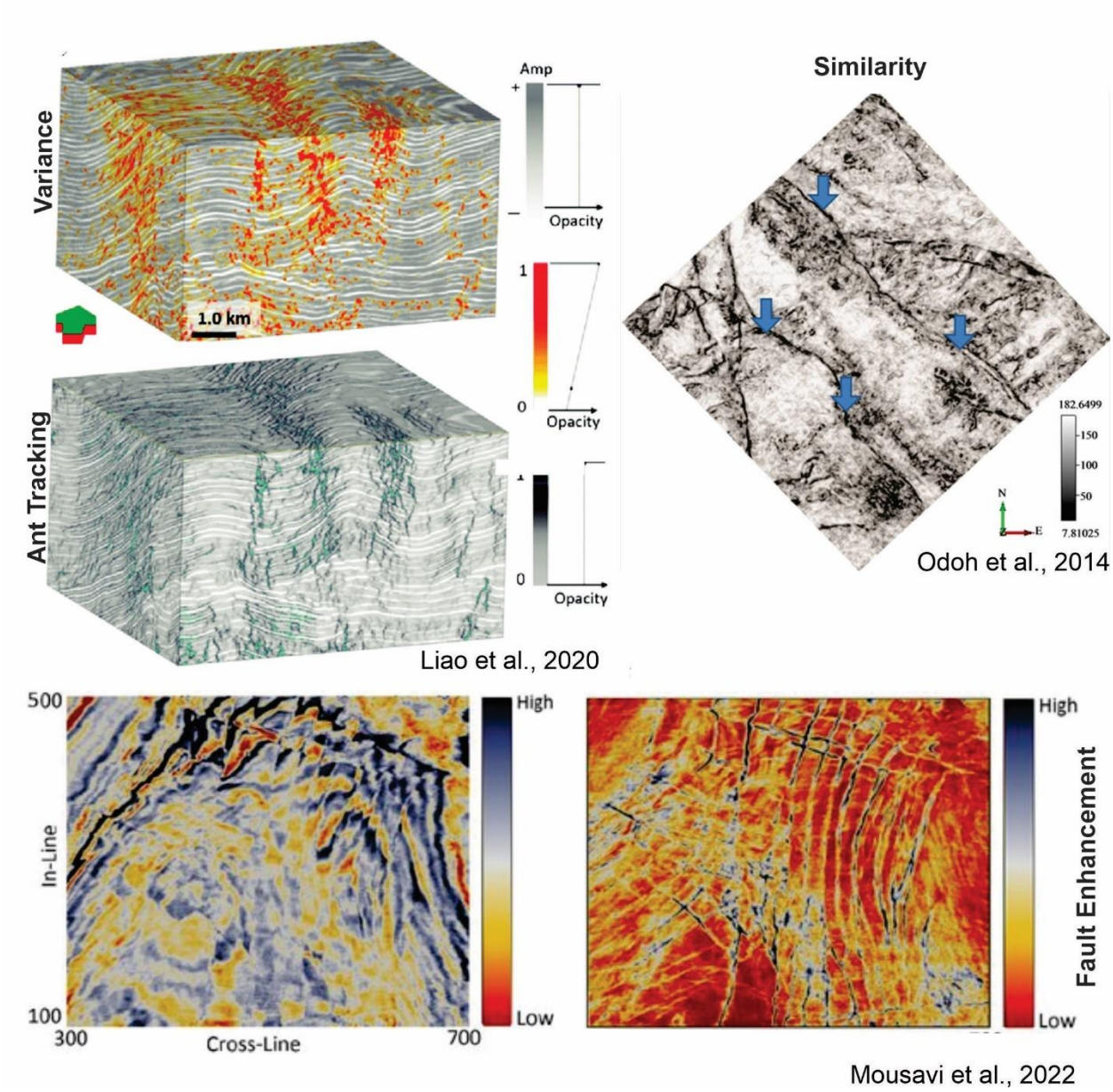

Figura 7 – Exemplos de atributos sísmicos aplicados com objetivo de revelar falhas, publicados em trabalhos recentes.

Os atributos sísmicos utilizados nessa pesquisa são baseados no atributo de coerência, ou *Coherence*, esse que vem sendo utilizado para destacar falhas e outras feições estratigráficas desde os anos de 1990 (Bahorich e Farmer, 1995), e revela característica estruturais medindo a semelhança entre dois traços sísmicos (Bahorich e Farmer, 1995; Marfurt et al., 1998, 1999; Gersztenkorn e Marfurt, 1999; Kluesner e

Brothers, 2015; Iacopini et al., 2016). Se apresentando sensível as descontinuidades dos horizontes sísmicos, formas de ondas sísmicas que apresentam altos valores de *Coherence* indicam que as litologias reconhecidas no dado sísmico estão lateralmente descontínuas, assim como a mudança brusca na forma da onda podem indicar falhas e fraturas nas rochas sedimentares, variando na escala de 0 a 1 (Figura ***8***7)

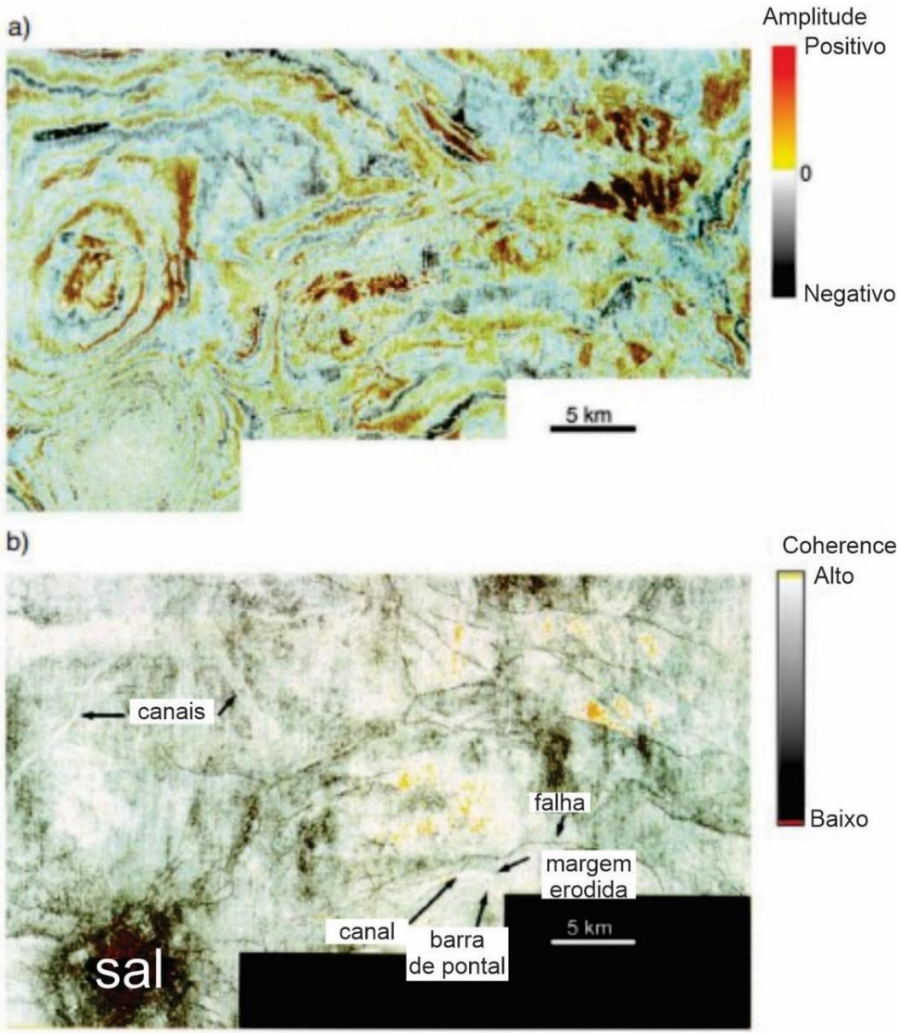

Figura 8 - Aplicação do atributo sísmico coherence para destacar feições geológicas em dados sísmica de reflexão (modificado de Chopra e Marfurt, 2007).

Referências:

Alaei, B., Torabi, A., 2017, Seismic imaging of fault damaged zone and its scaling relation with displacement: Interpretation, 5, 83-93, accessed 07 October 2022; http://dx.doi.org/10.1190/INT-2016-0230.1.

Anderson, L. J., Osborne, R. H., Palmer, D. F., 1983, Cataclastic rocks of the San Gabriel fault—An expression of deformation at deeper crustal levels in the San Andreas fault zones: Tectonophysics, 98, 209–251.

Aydin, A., 1978, Small faults formed as deformation bands in sandstone: Pure and Applied Geophysics PAGEOPH, v. 116, n. 4–5, p. 913–930.

Aydin, A., Johnson, A. M., 1978, Development of faults as zones of deformation bands and as slip surfaces in sandstone, Rock Friction and Earthquake Prediction, Springer, p. 931-942.

Bai, T., Pollard, D., 2000. Fracture Spacing in Layered Rocks: A New Explanation Based on the Stress Transition. Journal of Structural Geology 22(1):43-57. https://doi.org/10.1016/S0191-8141(99)00137-6.

Bahorich, M. S., Farmer, S. L., 1995, 3-D seismic discontinuity for faults and stratigraphic features: The coherence cube: SEG Technical Program Expanded Abstracts, Abstracts : 93-96, https://doi.org/10.1190/1.1887523.

Bertotti, G., Hardebol, N., Koppen, T. J. K., Luthi, S. M., 2007. Toward a quantitative definition of mechanical units: New techniques and results from an outcropping deep-water turbidite succession (Tanqua-Karoo Basin, South Africa), Geohorizons. https://doi.org/10.1306/03060706074.

Braathen, A., Tveranger, J., Fossen, H., Skar, T., Cardozo, N., Bastesen, E., Sverdrup, E., 2009, Fault facies and its application to sandstone reservoirs: AAPG Bulletin, v. 93, no. 7, pp. 891–917.

Botter, C., Cardozo, N., Hardy, S., Lecomte, I., Escalona, A., 2014, From mechanical modeling to seismic imaging of faults: A synthetic workflow to study the impact of faults

on seismic: Marine and Petroleum Geology, 57, 187-207, http://dx.doi.org/10.1016/j.marpetgeo.2014.05.013.

Botter, C., N. Cardozo, S. Hardy, I. Lecomte, G. Paton, and A. Escalona, 2016, Seismic characterization of fault damage in 3D using mechanical and seismic modeling: Marine and Petroleum Geology, 77, 973–990, accessed 23 October 2022; doi: 10.1016/j.marpetgeo.2016.08.002.

Brown, A. R., 1996, Seismic attributes and their classification. The Leading Edge, October, p.1090 (Interpreter's Corner).

Caine, J. S., Evans, J. P., Forster, C. B., 1996, Fault zone architecture and permeability structure: Geology, v. 24, p. 1025-1028.

Caine, J.S., Minor, S.A., 2009, Structural and geochemical characteristics of faulted sediments and inferences on the role of water in deformation, Rio Grande Rift, New Mexico: GSA Bulletin 121 (9 e 10), 1325 a 1340.

Childs, C., Manzocchi, T., Walsh, J. J., Bonson, C. G., Nicol, A., and Schöpfer, M. P., 2009, A geometric model of fault zone and fault rock thickness variations: Journal of Structural Geology, v. 31, p. 117-127.

Cohen, I., Coult, N., Vassilou, A. A., 2006, Detection and extraction of fault surfaces in 3D seismic data: Geophysics, 71, 21-27, accessed 13 September 2022; doi:10.1190/1.2215357.

Choi, J. H., Edwards, P., Ko, K., Kim, Y. S., 2016, Definition and classification of fault damage zones: a review and a new methodological approach: Earth-Science Reviews, v. 152, p. 70-87.

Chopra, S., Marfurt, K. J., 2007, Volumetric curvature attributes for fault/fracture characterization: First Break, 25, 19-30, accessed 13 September 2022; https://doi.org/10.1190/1.2756864.

Cooke, M. L., Simo, J. A., Underwood, C. A., Rijken, P., 2006. Mechanical stratigraphic controls on fracture patterns within carbonates and implications for groundwater flow.

Sedimentary Geology. Volume 184, Issues 3–4, 15, Pages 225-239. https://doi.org/10.1016/j.sedgeo.2005.11.004.

Dorn, G. A., 1998, Modern 3-D seismic interpretation: The Leading Edge, 17, 1177–1328, accessed 13 September 2022; https://doi.org/10.1190/1.1438121.

Ferrill, D. A., Morris, A. P., 2003. Dilational Normal Faults: Journal of Structural Geology, V. 25, P. 183–196. https://doi.org/10.1016/S0191-8141(02)00029-9.

Ferrill, D. A., Morris, A. P., 2008. Fault zone deformation controlled by carbonate mechanical stratigraphy, Balcones fault system, Texas. American Association of Petroleum Geologists. 92, 359-380. https://doi.org/10.1306/10290707066.

Ferrill, D. A., Morris, A. P., Mcginnis, R. N., Smart, K. J., Wigginton, S. S., Hill, N. J., 2017. Mechanical Stratigraphy and Normal Faulting. Journal of Structural Geology. https://doi.org/10.1016/j.jsg.2016.11.010.

Fossen, H., Schultz, R. A., Shipton, Z. K., and Mair, K., 2007, Deformation bands in sandstone: a review: Journal of the Geological Society, v. 164, p. 755-769.

Fossen, H., 2010, Deformation bands formed during soft-sediment deformation: Observations from SE Utah: Marine and Petroleum Geology, v. 27, n. 1, p. 215–222.

Gersztenkorn, A., Marfurt, K. J, 1999, Eigen structure-based coherence computations as an aid to 3-D structural and stratigraphic mapping. Geophysics 64:1468–1479.

Heynekamp, M. R., Goodwin, L. B., Mozley, P. S., Haneberg, W. C., 1999, Controls on fault-zone architecture in poorly lithified sediments, Rio Grande Rift, New Mexico: Implications for fault zone permeability and fluid flow. In: Haneberg, P.S., Mozley, P.S., Moore, J.C., Goodwin, L.B. (Eds.), Faults and Subsurface Fluid Flow in the Shallow Crust, vol. 113. American Geophysical Union Monograph, pp. 27e49.

Iacopini, D., Butler, R. W. H., Purves, S., McArdle, N., De Freslon, N., 2016, Exploring the seismic expression of fault zones in 3D seismic volumes: Journal of Structural Geology, 89, 54-73, accessed 13 September 2022; https://doi.org/10.1016/j.jsg.2016.05.005.

Kluesner, J. W., Brothers, D. S., 2016, Seismic attribute detection of faults and fluid pathways within an active strike-slip shear zone: New insights from high-resolution 3D P-Cable™ seismic data along the Hosgri Fault, offshore California: Interpretation, 4, 1F-T121, accessed 13 September 2022; https://doi.org/10.1190/INT-2015-0143.1.

Laubach, S. E., Olson, J. E., Gross, M. R., 2009. Mechanical and Fracture Stratigraphy. AAPG Bulletin, v. 93, no. 11, pp. 1413–1426. https://doi.org/10.1306/07270909094.

Liao, Z., Li, W., Zou, H., Hao, F., Marfurt, K. J., Reches, Z., 2020, Composite damage zones in the subsurface, Geophysical Journal International, Volume 222, Issue 1, p 225–230, https://doi.org/10.1093/gji/ggaa158.

Machado, G., A. Alali, B. Hutchinson, O. Olorunsola, K. J. Marfurt, 2016, Display and enhancement of volumetric fault images: Interpretation, 4, 51–61, accessed 13 September 2022; doi: 10.1190/INT-2015-0104.1.

Marfurt, K. J., Kirlin, R. L., Farmer, S., Bahorich, M., 1998, 3-D seismic attributes using a semblance-based coherency algorithm: Geophysics, 63, 1150-1165.

Marfurt, K. J., Sudhaker, V., Gerztenkorn, A., Crawford, K. D., Nissen, S. E., 1999, Coherency calculations and the presence of structural dip: Geophysics, 64, 104,111.

Maul, A. R., 2005, Delimitação de reservatórios delgados utilizando atributos sísmicos, Dissertação de Mestrado, Universidade Federal Fluminense.

Mcquillan, H., 1974. Fracture Patterns on Kuh-E Asmari Anticline, Southwest Iran. AAPG Bull. 1177 58, 236–246. https://doi.org/10.1306/83D913C1-16C7-11D7-8645000102C1865D.

Morris, A. P., Ferrill, D. A., McGinnis, R. N., 2009. Mechanical stratigraphy and faulting in Cretaceous carbonates. AAPG Bulletin, v. 93, no. 11, p. 1459–1470. doi: 10.1306/04080909011.

Mousavi, J., Radad, M., Monfared, M. S., Kahoo, A. R., 2022, Fault Enhancement in Seismic Images by Introducing a Novel Strategy Integrating Attributes and Image Analysis Techniques: Pure and Applied Geophysics, V. 179, 1645-1660; http://dx.doi.org/10.1007/s00024-022-03014-y.

Lavenu, A. P. C., Lamarche, J., 2018. What controls diffuse fractures in platform carbonates? Insights from Provence (France) and Apulia (Italy). Journal of Structural Geology. V. 108, pp. 94-107. https://doi.org/10.1016/j.jsg.2017.05.011.

Odoh, B. I., Ilechukwu, J. N., Okoli, N. I., 2014, The Use of Seismic Attributes to Enhance Fault Interpretation of OT Field, Niger Delta: International Journal of Geosciences, V. 5, DOI:10.4236/ijg.2014.58073.

Roche, V., Homberg, C., Rocher, M., 2013. Fault nucleation, restriction, and aspect ratio in layered sections: Quantification of the strength and stiffness roles using numerical modeling. J. Geophys. Res., Solid Earth, 118, 1–15. doi: 10.1002/jgrb.50279

Roden, R., Smith, T., Sacrey, D., 2015, Geologic pattern recognition from seismic attributes: Principal component analysis and self-organizing maps: Interpretation, 3, 59-83, accessed 13 September 2022; http://dx.doi.org/10.1190/INT-2015-0037.1.

Sibson, R.H., 1977. Fault rocks and fault mechanisms. Journal of Geological Society of London, 133, 191–213.

Schultz, R.A., Okubo, C.H., Fossen, H., 2010, Porosity and grain size controls on compaction band formation in Jurassic Navajo Sandstone: Geophysical Research Letters, v37.

Shipton, Z.K., Evans, J.P., Thompson, L.B., 2005. The geometry and thickness of deformation-band fault core and its influence on sealing characteristics of deformation-band fault zones. AAPG Memoir 85, 181–195. https://doi.org/10.1306/1033723M853135

Torabi, A., and Berg, S. S., 2011, Scaling of fault attributes: A review: Marine and Petroleum Geology, v. 28, p. 1444-1460.

Torabi, A., Alikarami, R., 2012, Heterogeneity within deformation bands in sandstone reservoirs: 46th American Rock Mechanics Association Symposium, Chicago 24th–27th June, 7 pp.

Torabi, A., Balsamo, F., Nogueira, F. C. C., Vasconcelos, D. L., Silva, A. C. E., Bezerra, F. H. R., Souza, J. A. B., 2021, Variation of thickness, internal structure and petrophysical properties in a deformation band fault zone in siliciclastic rocks: Marine and Petroleum

Geology, 133, 105297, accessed 13 September 2022; https://doi.org/10.1016/j.marpetgeo.2021.105297.

Xu, H., Sun, S. Z., 2014, Seismic singularity attribute and its applications in sub-seismic faults detection: Acta Geodaetica et Geophysica, 49, 403-414, accessed 20 October 2022; DOI: 10.1007/s40328-014-0071-7.

Yuan, S. Y., Wang, S. X., 2013, Edge-preserving noise reduction based on Bayesian inversion with directional difference constraints. Journal of Geophysics and Engineering, 10, 1-10, accessed 20 October 2022; http://dx.doi.org/10.1088/1742-2132/10/2/025001.

Zahm, C. K., Hennings, P. H., 2009.Complex fracture development related to stratigraphic architecture: Challenges for structural deformation prediction, Tensleep Sandstone at the Alcova anticline, Wyoming. AAPG Bulletin, V. 93, No. 11. doi: 10.1306/08040909110.

Capítulo 4

Resultados

4 Resultados

Os resultados da presente tese se dispõem na forma de artigos científicos nesta sessão. Seguindo a ordem de cronologia de publicação/submissão de trabalhos apresenta-se: (1) Mechanical Stratigraphy Influences Deformation Band Pattern in Arkosic Sandstones, Rio do Peixe Basin, Brazil - artigo publicado na *Journal of Structural Geology* em 4 de Janeiro de 2022; (2) Automatic 3D fault detection and characterization – a comparison between seismic attribute methods and deep learning – artigo submetido na *Interpretation* em 15 de Fevereiro de 2022;

This manuscript was published on Journal Structural Geology, since February 2022.

4.1 Artigo 1 - MECHANICAL STRATIGRAPHY INFLUENCES DEFORMATION BAND PATTERN IN ARKOSIC SANDSTONES, RIO DO PEIXE BASIN, BRAZIL

Lorenna Sávilla Brito Oliveira[a,b], Francisco Cézar Costa Nogueira[a], David Lino Vasconcelos[a], Fabrizio Balsamo[c], Francisco Hilário Rêgo Bezerra[b], Yoe Alain Reyes Perez[b]

[a] Federal University of Campina Grande, Brazil

[b] Federal University of Rio Grande do Norte, Brazil

[c] Department of Chemistry, Life Sciences and Environmental Sustainability, University of Parma, Parco Area delle Scienze 157/A, Campus Universitario, Parma, Italy

Abstract

This study shows how mechanical stratigraphy influences deformation bands' structural attributes in faulted, heterolithic arkosic sandstones in the Rio do Peixe Basin, northeastern Brazil. We combined the analyses of sedimentary units with rock properties measurements (porosity, permeability, Young's modulus, Poisson's ratio, and uniaxial compressive strength) and structural data to characterize the mechanical units and related deformation band pattern. Our results show that deformation bands have differences in frequency, geometry, thickness, and dip in different mechanical units. In addition, sedimentary parameters as grain size, layer thickness, stratification, cementation, and mineral composition impact the vertical propagation of deformation bands. In each layer, deformation bands frequency increases approaching a normal fault, and the dip of the deformation bands varies when passing through layers. In the studied mechanical units, deformation band density increases with increasing host rock porosity and decreasing Young's modulus. Finally, we document that the development of deformation bands increases the overall cohesion of the fault zone, particularly in units with coarser grain sizes. Our data may have implications for mechanical stratigraphy in faulted siliciclastic reservoirs.

Keywords: Mechanical stratigraphic; Deformation bands; Petrophysical properties; Fault zones; Geomechanics

4.1.1 Introduction

In sedimentary rocks, faults and fractures may change frequency, spacing and geometry in beds with different thicknesses and rheology (Laubach *et al*., 2009; Ferril *et al.*, 2017; Torabi *et al*., 2019). For instance, the mechanical stratigraphy of individual beds or bed packages can influence the dip angle of the faults, thus influencing the vertical propagation of deformation (Ferrill and Morris, 2003).

Nonetheless, several studies brought an understanding of fault deformation and its secondary structures when crossing rock layers (e.g., Ferrill and Morris, 2003; Bertotti *et al*., 2007; Ferrill and Morris, 2008; Laubach *et al*., 2009; Morris *et al*., 2009; Roche et al., 2013; Ferrill *et al*., 2017; Chandra *et al*., 2021; Araujo *et al.,* 2021). Furthermore, the mechanical and petrophysical properties could change considerably during volumetric deformation in porous sandstones (Del Sole and Antonelini, 2019) and deformation bands hosted in porous carbonates (Cilona *et al.,* 2012; Tondi *et al.,*2012; 2016; Zambrano *et al.,* 2018). In this sense, mechanical stratigraphy investigates the relationship between sedimentary bed rheology and fracture intensity (e.g., McQuillan, 1974; Bai and Pollard, 2000; Bertotti et al.,2007; Cooke *et al*., 2006; Zahm and Hennings, 2009; Lavenu and Lamarche, 2018). The structural and sedimentary analyses applied to mechanical stratigraphy allow to observe the linkage between the structure geometry (Ferrill and Morris, 2003; Morris *et al*., 2009b; La Bruna *et al.,* 2021) and fracture development of (Ferrill and Morris, 2008; Roche *et al*., 2013; Pontes *et al.,* 2021). However, the factors that define mechanical unit variety are still debated. For example, a mechanical unit could be defined by (a) layer where fractures start and end (Bertotti *et al*., 2007), (b) by the layer thickness and their rheological properties (Ferrill *et al*., 2017) or (c) by layered rocks subdivided into mechanical property intervals (Bai and Pollard, 2000; Bai *et al*., 2002; Cardozo *et al*., 2005; Balsamo *et al.,*2020).

In siliciclastic rocks with porosity greater than 10-15%, deformation bands are common structures (Fossen *et al.*, 2011, and references therein), usually associated with a localized decrease of porosity and permeability (Aydin, 1978; Antonellini and Aydin, 1994; Alikarami *et al*., 2013; Torabi *et al.,* 2020). On the other hand, in heterolithic siliciclastic sequences, opening-mode fractures (i.e., joints) tend to develop in low-porosity layers (e.g., Balsamo *et al*., 2013). Additionally, the development of deformation bands tends to increase the rock's cohesion (Pizzati et al., 2020), whereas joints and faults tend to decrease the bulk rock’s cohesion (Fossen *et al.*, 2007).

Recent studies indicate the importance and complexity of the deformation bands passing through different layers. They focus on understanding these structures in deformed beds, forming smears along the fault trace with a continuous displacement geometry (mixed fault zone) (e.g., Bense and Person, 2006; Lindsay *et al*., 1993; Loveless *et al*., 2011; Torabi *et al*., 2019). However, some essential aspects are still missing in understanding the behavior of deformation bands that cut across different

sedimentary beds. They are: (1) which parameters should be considered to define a mechanical unit crossed by deformation bands? (2) How do deformation bands change rock properties passing through a context with different rheological layers or different types of sandstones? (3) How do deformation bands in different mechanical units affect fluid flow in heterolithic siliciclastic reservoirs?

The present study investigates how mechanical stratigraphy influences the pattern and attributes of fault-related deformation bands in arkosic, poorly lithified sandstones. The study area is the intracontinental Rio do Peixe Basin (RPB) in northeastern Brazil, where the influence of local stratigraphy on the petrophysical properties of the siliciclastic rocks has not been addressed. We analyze the mechanic units using the following parameters: layer thickness, lithology, competency of the layers, the uniaxial compressive strength (UCS), porosity, permeability, Poisson's ratio, and Young's modulus. The present study shows that deformation bands have distinct structural attributes and geometry in different layers of sandstones, changing the physical properties of the host rock. These findings may have implications for mechanical stratigraphy and fluid flow modeling in faulted siliciclastic reservoirs.

4.1.2 Geological Setting

4.1.2.1 Tectonic and Stratigraphic Background of the RPB

The RPB belongs to a group of sedimentary basins generated during the South America-Africa breakup in the Early Cretaceous (Matos, 1992). The RPB is a rift basin composed of three half-grabens termed Brejo das Freiras, Sousa, and Pombal sub-basins, respectively bounded by the Portalegre, Malta, and Rio Piranhas faults (Françolin *et al*., 1994; de Castro *et al*., 2007) (Fig. 1A). The opening geometry and kinematics of these half-grabens were controlled by the brittle reactivation of the preexistent ductile Precambrian shear zones in the crystalline basement (Sénant and Popoff, 1991; Françolin *et al*.,1994; de Castro *et al*., 2007; Nogueira *et al*., 2015). The shallow brittle reactivation of these preexisting structures also occurred during the post-rift stage of the RPB (Nogueira *et al*., 2015; Vasconcelos *et al*., 2021).

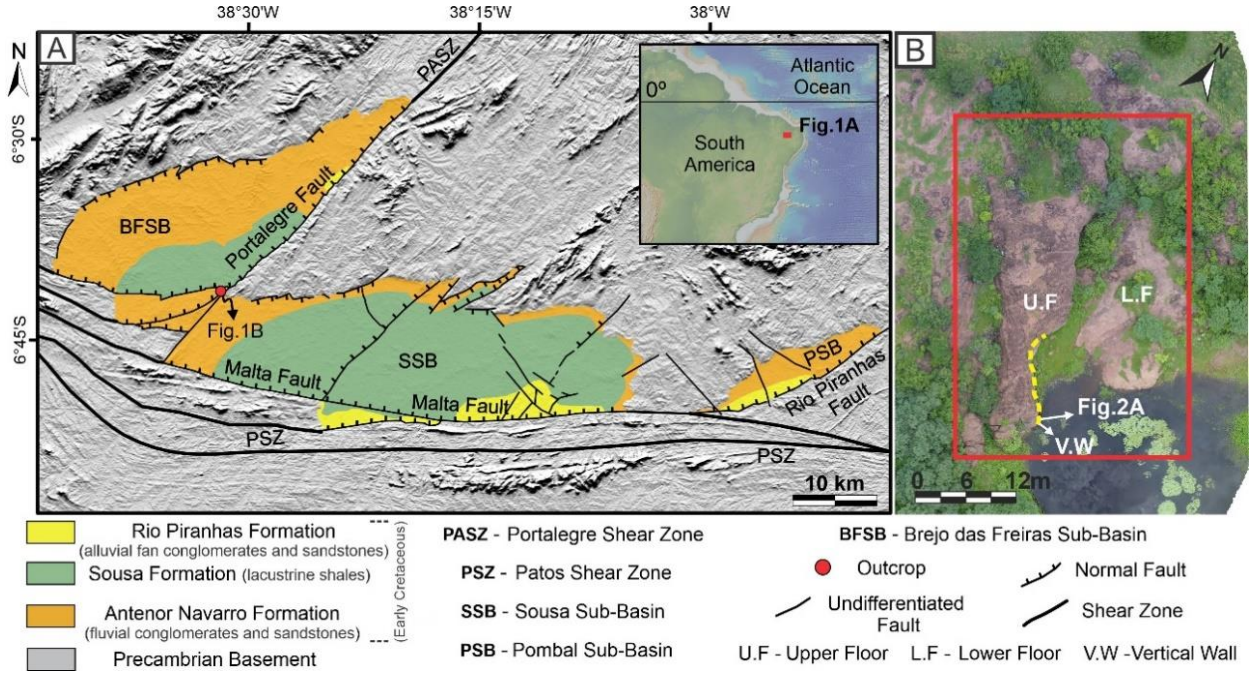

Figure 1 – (A) Geological map of the RPB with the studied outcrop location. (B) Drone Image of the outcrop. The red rectangle corresponds to the mapped area, and the dashed yellow line corresponds to the vertical wall of the outcrop shown in Fig. 2A.

The sediments filling the RPB pertain to three Early Cretaceous formations (Fig. 1A), from bottom to top: Antenor Navarro, Sousa, and Rio Piranhas (Sénant and Popoff, 1991; Carvalho *et al.,* 2013). This study investigated an outcrop at the top of the Antenor Navarro Formation, composed of conglomerates and arkosic to coarse lithic sandstones at the base and fine arkosic sandstones at the top (Araujo *et al*., 2018; Nogueira *et al*., 2021). The Antenor Navarro Formation interfingers towards the top with shale deposits in the Sousa Formation lacustrine system (Rapozo *et al*., 2021).

4.1.2.2 Previous Studies of Deformation Bands in the RPB

Recent studies in the RPB have addressed the deformation bands and their influence on the petrophysical properties of the host rock (e.g., Araujo *et al*., 2018; Maciel *et al*., 2018; Nicchio *et al*., 2018; Pontes *et al*., 2019; Souza *et al*., 2021; Nogueira *et al*., 2021; Torabi *et al.,* 2021; Silva *et al.,* 2022). These studies proposed that the microcrack coalescence and cataclasis processes (e.g., grain size reduction, grain rotation, and grain border comminution) are the main deformation mechanisms responsible for deformation band development (Nicchio *et al*., 2018; de Souza *et al*., 2021). Two types of fault zones are proposed in the RPB: (i) typical fault zone and (ii) deformation band fault zone (Araujo *et al*., 2018; Torabi *et al*., 2021; Silva *et al*., 2022). The difference is that the second type lacks a principal slip surface and a classical fault core. A logarithmic decrease in deformation bands frequency moves away from the fault core is recorded in both cases. Another parameter controlling the spatial distribution of deformation bands is the mean

grain size of sandstone, where clustered deformation bands are observed only in coarse sandstones (Araujo *et al*., 2018). Furthermore, the studies in the RPB also analyzed the influence of deformation bands on the petrophysical properties of the host rock. For instance, the rock resistance is three times higher in the fault zones with multiple fault cores than in fault zones with a single fault core and four times higher than the non-deformed units (Pontes *et al.,* 2019). In addition, a permeability reduction of up to three orders of magnitude and a porosity reduction of up two orders of magnitude in the deformations bands is recorded compared to the host rock (Pontes *et al*., 2019; Torabi *et al*., 2021; Silva *et al*., 2022). Finally, the intensity of cataclastic deformation, based on the amount of cataclastic matrix, exhibits a reduction in the permeability and porosity, reaching up to five and two orders of magnitude, respectively, concerning the undeformed sandstone (Nogueira *et al*., 2021).

4.1.3 Materials and Methods

This research integrates field mapping of an outcrop 28 m long and 36 m wide in the Portalegre Fault Zone (Fig. 1). We performed structural analysis, in situ UCS determination, petrography, and analysis of petrophysical and geomechanical properties of sedimentary units. Besides, using the obtained results as input data, we modeled the porosity and permeability properties of the 3D outcrop.

4.1.3.1 Field Mapping, Structural Analysis, and Sedimentary Unit Description

Two outcrop pavements (subdivided respectively in upper and lower), and vertical walls, were mapped to constrain the 3D geometry of the fault and related deformation bands using images from a high-precision Unmanned Aerial Vehicle (UAV) as support (Fig. 1B). Three scanlines oriented perpendicular to the principal sets of the deformation bands were performed to measure the frequency and length of the deformation bands using a comparator to measure length as Ortega *et al.* (2006) and their direction, except for the unit 3 thickness, which is not exposed in 3D but only in the vertical wall. Two scanlines were measured on the upper and lower pavements and a third in the wall orthogonal to the main fault.

The wall exposure shows four distinct sedimentary units (layers), allowing the description and sampling of individual beds. Furthermore, the units were described microscopically, using an optical petrographic microscope to determine grain size, mineralogy, porosity, and cementation.

4.1.3.2 Physical Rock Property Analyses and 3D Modeling

4.1.3.2.1 Uniaxial Compressive Strength (UCS) Analyses

We measured *in situ* rebound values using L-type Schmidt Hammer (Aydin and Basu, 2005). We performed these tests to quantity the parameter of UCS in the deformation bands and the host rock between bands (i.e., the space between individual

deformation bands of the same set). We performed these tests on the outcrop wall in three vertical profiles using metric tape to obtain geomechanical data from every sedimentary unit, following the *American Society for Testing and Materials* (ASMT, 2001). We performed ten rebound measurements at each point to identify possible irregularities in the plans to avoid reading errors in the equipment. In the cases of identified irregularities, a battery-powered polisher was used to rectify the surfaces and thus measure the rebounds. Then, we calculated the average (arithmetic mean) of these measurements. We investigated 43 points in both deformation bands (28 points) and their interspace (host rock) (15 points) in arkosic sandstone outcrops.

4.1.3.2.2 Porosity, Permeability, Young's modulus, Poisson's Ration Analyses

We sampled 14 plugs from the four sedimentary units for petrophysics analyses. All the samples were collected from sandstones with deformation bands on the hanging wall. The preparation of the samples used a saw to cut plugs 5 cm wide (1.5 inches in diameter); we used a perfect cylinder to make the ends of the plugs flat and parallel. Before starting the analyses, the plugs were placed in a drying oven for 24 hours at a constant temperature of 80ºC. Then, we weighted the samples using a precision electronic weight scale. The plug analyses were performed with the UltraPoroPerm 500 (Corelab) and Autolab 500 (New England Research) equipments at the Federal University of Campina Grande (Brazil). The first equipment measures porosity and permeability with ranges of 0-40 porosity units (%) and 0.001 to 20,000 mD using a permoporosimeter by gas expansion, which injects nitrogen gas into the samples applying Boyle law to measure the sample grain volume. The second equipment measures wave velocity relation (P and S-waves; however, only P-waves were used), derived from measuring Young's modulus and Poisson's Ration. During elastic measurements, the confining pressure varied between 5 to 40 MPa, while temperature and pressure were maintained at an ambient level.

Additionally, we performed a petrotyping classification (Corbett and Potter, 2004) of the plugs using the Global Hydraulic Elements (GHE) method to compare sample porosity and permeability. Then, we plotted the porosity and permeability results of the 14 plug on the GHE basemaps with the trends of the Flow Zone Indicator (FZI) (Amaefule *et al*., 1993).

4.1.3.2.3 3D modeling of petrophysical properties

This study adapted the workflow proposed by Caers (2005) and Pyrcz and Deutsch (2014) to the geologic and petrophysical data collected in the outcrop. We built the Digital Terrain Model (DTM) of the outcrop exposed area, filtering 15,497 points from the original 527,457 Digital Surface Model (DSM) points dataset obtained from UAV imagery. We transferred the DTM to a digital numerical subsurface with an accurate representation of depositional geometry and stratigraphic layers (Marques Jr *et al.,* 2020).

Using the Schlumberger Petrel® software, the 3D cell grid (I, J, K) was defined as a volume 0.1 x 0.1 x 0.36 m to represent the field data and the petrophysical heterogeneity. The petrophysical modeling uses the sequential Gaussian Simulation algorithm visiting each grid node in random order and doing the following: finding nearby data and previously simulated grid nodes; constructing the conditional distribution by kriging (calculating a mean and estimation variance by simple kriging); drawing a simulated value from the conditional distribution. This procedure is repeated with random numbers of seeds to generate multiple realizations (Pyrcz and Deutsch, 2014).

4.1.4 Results

4.1.4.1 Sedimentary Unit Description

The analyzed outcrop exhibits four sedimentary units exposed in the vertical wall (Fig. 2A). These sedimentary units consist mostly of very fine to conglomeratic arkosic sandstones, which occur both on the fault's hangingwall and footwall (Fig. 2). However, due to the normal kinematics of the main fault, the lower unit 1 observed in the footwall does not outcrop in the hangingwall block (Fig. 2A).

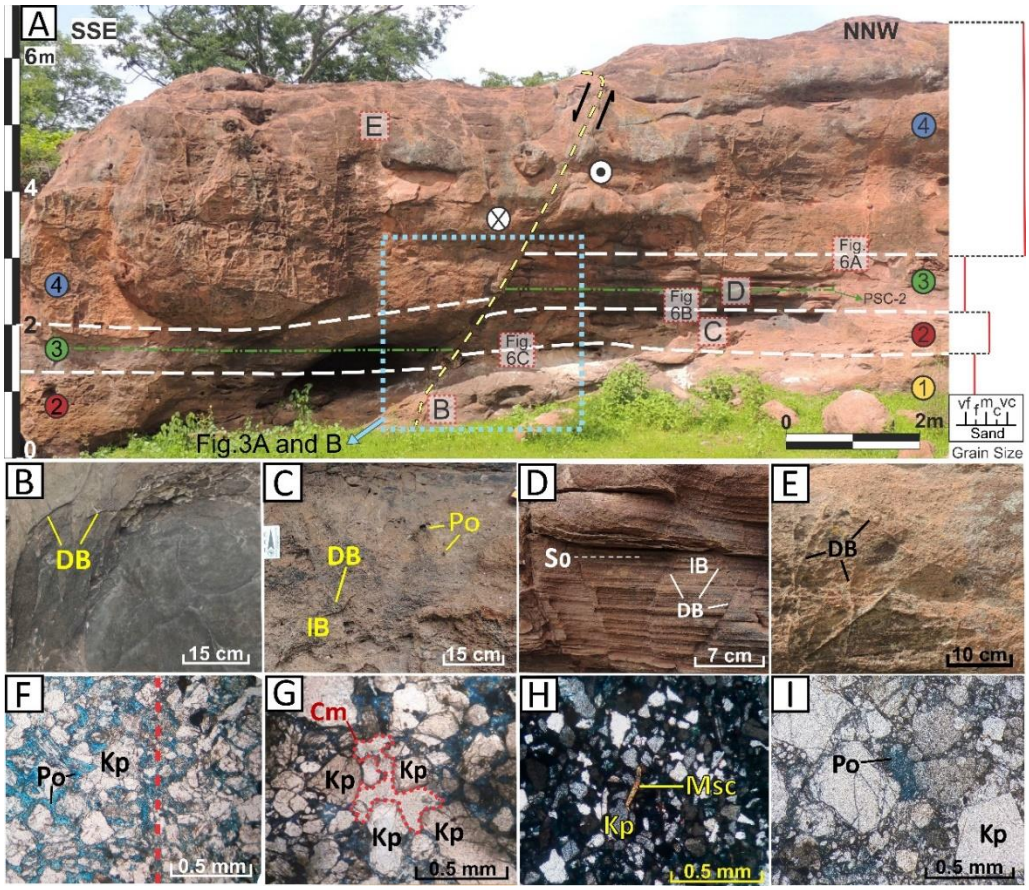

Figure 2 – (A) Vertical wall with sedimentary unit limits indicated by white dashed lines. The yellow dashed line indicates the main normal dextral fault. On the right side, a schematic grain size range for each unit.

Photos of each bed (B), (C), (D), and (E), and their respective microscopic features (F), (G), (H), and (I). (B) Unit 1 (yellow circle in Fig. 2A) is a fine sandstone with deformation bands. (C) Unit 2 (red circle in Fig. 2A) is a massif pebbly sandstone with vug porosity. (D) Unit 3 (green circle in Fig. 2A) is a very fine sandstone with a planar bedding stratification. (E) Unit 4 (blue circle in Fig. 2A) is a matrix-supported pebble sandstone with deformation bands. (F) Microscopic view of unit 1 with changes in porous space between K-feldspar grains in the host rock. This change is marked by variation from open to tight package (boundary of deformation band indicated by the red dotted line). (G) Microscopic view of unit 2, the red dotted area indicates carbonate cement between the K-feldspar grains. (H) Microscopic view of unit 3 showing muscovite grain between the K-feldspar grains. (I) Microscopic view of unit 4 showing a moldic porosity in a K-feldspar grain. DB: Deformation Band, IB: Interspace area between Bands, Po: Porosity, S_0: Bedding, Kp: K-feldspar, Cm: Carbonate cement, Msc – Muscovite.

The sedimentary unit 1 is a cohesive sandstone, varying from fine to medium grain size (Fig. 2B). We also identified muddy lenses along this unit. The sandstone is well sorted and mostly composed of feldspar and quartz grains and subordinately biotite and opaque minerals. Some deformation bands have a tight fabric in thin sections, with sharp boundaries with non-deformed porous sandstone (Fig. 2F). Sedimentary unit 2 is a massif pebbly sandstone with some clay lenses. Macroscopically, the porosity of this unit is greater than unit 1 with vugs and dissolved pores (Fig. 2C). The sandstone is poorly sorted locally with contact points between grains. Microscopically, this unit comprises fractured and dissolved grains of feldspar, quartz, and rock fragments with carbonate cement (Fig. 2G). Sedimentary unit 3 comprises sandstone with grain size varying from fine to very fine, with clay matrix and planar stratification. The sandstone is mainly composed of feldspar, opaque and micaceous minerals (Fig. 2H). In addition, sedimentary unit 3 is the most affected by thin deformation bands (Fig. 2D). The grains are fractured and dissolved, with tight packing marked by curved grain boundaries. Muscovite and biotite do not follow a structural trend like the other aligned grains within the deformation bands. Sedimentary unit 4, the thickest layer, is a matrix-supported pebble sandstone composed of very coarse sand located at the top of the section (Fig. 2E). The sandstone is poorly sorted and composed of fractured feldspar grains that show closed packing. In some thin sections, weathered feldspar grains exhibit moldic porosity (Fig. 2I).

Units 1 and 3 exhibit thicknesses roughly similar (120 cm and 110 cm, respectively); unit 4 is the thickest bed (320 cm), and unit 2 is the thinnest bed (65 cm). All layers are offset by the main fault (Fig. 2A), but unit 3 exhibits a drag geometry close to the main slip surface (Fig. 3A, B).

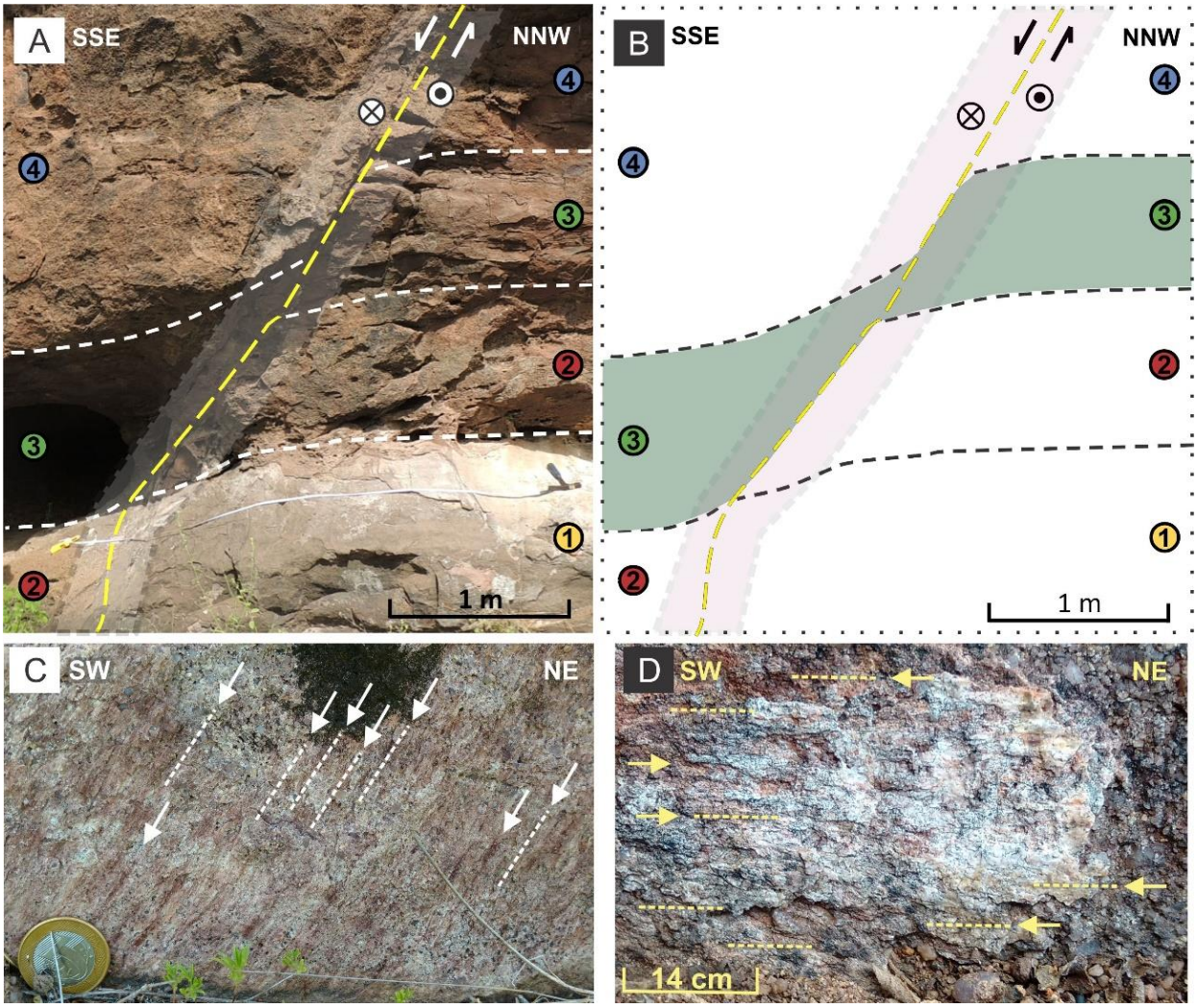

Figure 3 – (A) Central area from the vertical wall (see Fig. 2A for detailed location). (B) Line drawing of (A) showing the stratigraphic unit 3 brittle-ductile behavior. The yellow dotted line indicates the main fault, and the black dotted lines indicate the sedimentary unit limits. The main fault slickenlines are shown in (C) and (D).

4.1.4.2 Structural Mapping and Analyses

Drone imagery supported identifying deformation band location, orientation, and density (Fig. 4A). The deformation bands mostly strike NE-SW and secondarily E-W, NW-SE, and N-S (Fig. 4A). We verified the relationship between the structural data from the study area with the kinematics of major basin border faults (Fig. 4A). We named the antithetic normal fault the main fault (Fig. 4A). This antithetic normal fault strikes NE, cuts all the stratigraphic units, exhibits mostly normal movement with a minor dextral strike-slip component (Fig. 4A and 3C and D), and shows a displacement of 1.35 m (Figs 2A and 3).

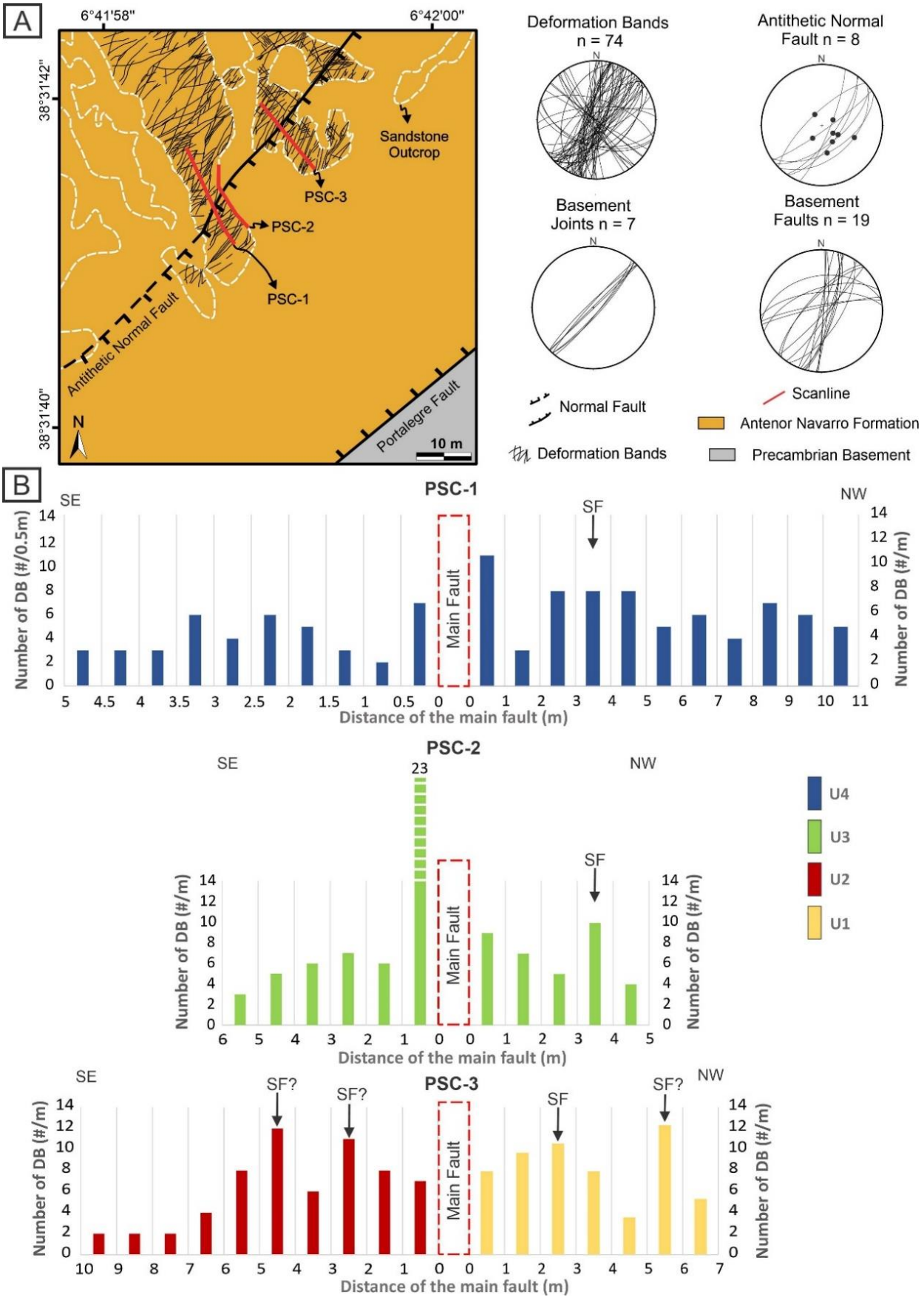
A
6°41'58"
6°42'00"
38°31'42"
38°31'40"
Sandstone Outcrop
PSC-3
PSC-2
PSC-1
Antithetic Normal Fault
Portalegre Fault
N
10 m
Deformation Bands n = 74
Antithetic Normal Fault n = 8
Basement Joints n = 7
Basement Faults n = 19
Normal Fault
Deformation Bands
Scanline
Antenor Navarro Formation
Precambrian Basement
B
PSC-1
SE
NW
SF
Main Fault
Number of DB (#/0.5m)
Number of DB (#/m)
Distance of the main fault (m)
PSC-2
23
U4
U3
U2
U1
PSC-3
SF?
SF?
SF
SF?

Figure 4 – (A) Structural map of the studied outcrop using the drone image with deformation bands and the normal basin border fault. The strikes of the mapped structures are shown in equal-area lower hemisphere stereographic projections. The red lines comprise the scanline locations. (B) Scanlines that we measured at each unit across the main fault. PSC-1 and PSC-3 were measured on the upper and lower floor, respectively, while the PSC-2 was measured in the vertical wall. The frequency of deformation bands increases near the main fault. Key: SF? – Possible Secondary Fault; SF – Secondary Fault.

Scanline data in Fig. 4B indicate that deformation bands' frequency is higher close to the main fault and tends to decrease moving away from it both in the hangingwall and footwall blocks. The average frequency of the deformation bands in units 4 (PSC-1 in Fig. 4B), 3 (PSC-2 in Fig. 4B), 2 (PSC-3 in Fig. 4B), and 1 (PSC-3 in Fig. 4B) are 5, 7, 6, and 6 deformation bands/m, respectively. However, this average frequency increases near the main fault (antithetic normal fault in Fig. 4A). For instance, unit 4 exhibits an average of 11 deformation bands/m (PSC-1 in Fig. 3B), unit 3 shows an average of 11 deformation bands/m (PSC-2 in Fig. 3B), whereas units 2 and 1 present an average of 8 and 7 deformation bands/m (PSC-3 in Fig. 4B), respectively. Furthermore, some local frequency increases are related to deformation band clusters, possibly associated with secondary faults (SF in Fig. 4B).

We reported that the deformation bands frequency decreased in the following unit order: 3, 1, 2, and 4 (Fig. 4). Units 1 and 2 were affected by deformation bands in similar dip analyses, distinguishing themselves in the frequency (7 and 4.7 bands/m, respectively). Unit 3 has the highest frequency of bands (8.8 bands/m). Consequently, it is the most intensely deformed compared to the others. In contrast, unit 4 is less deformed, with 3.5 bands/m. The scanline data also indicate that the deformation band frequency is higher in the footwall than the hangingwall (Fig. 5B).

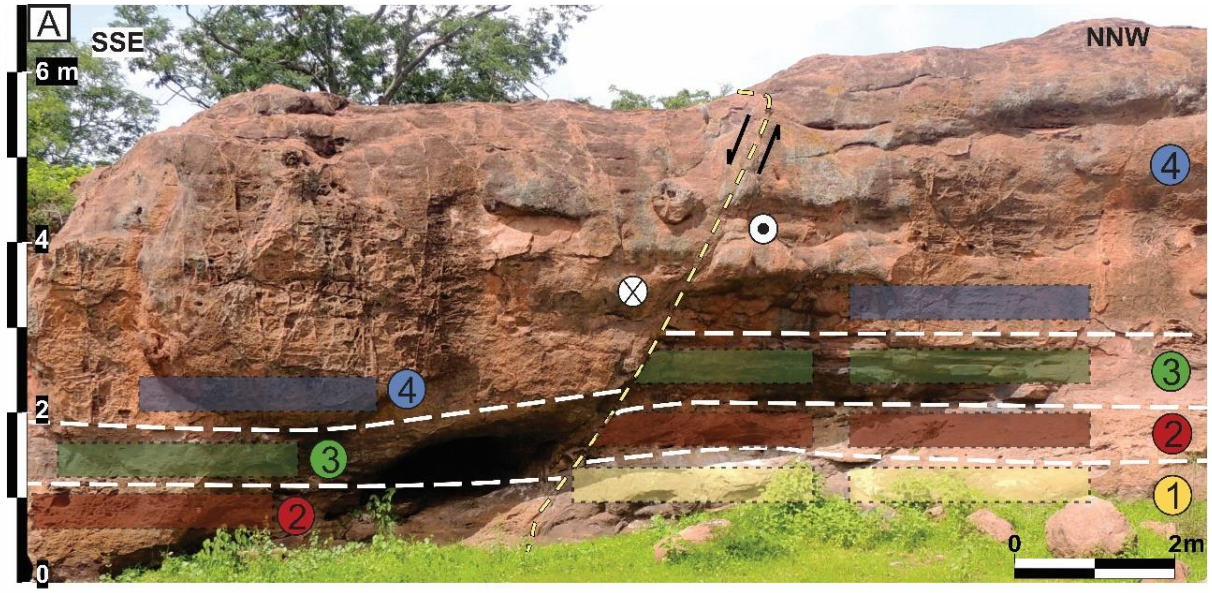
A
SSE
NNW
6 m
4
2
0
4
3
2
1
4
3
2
0
2m

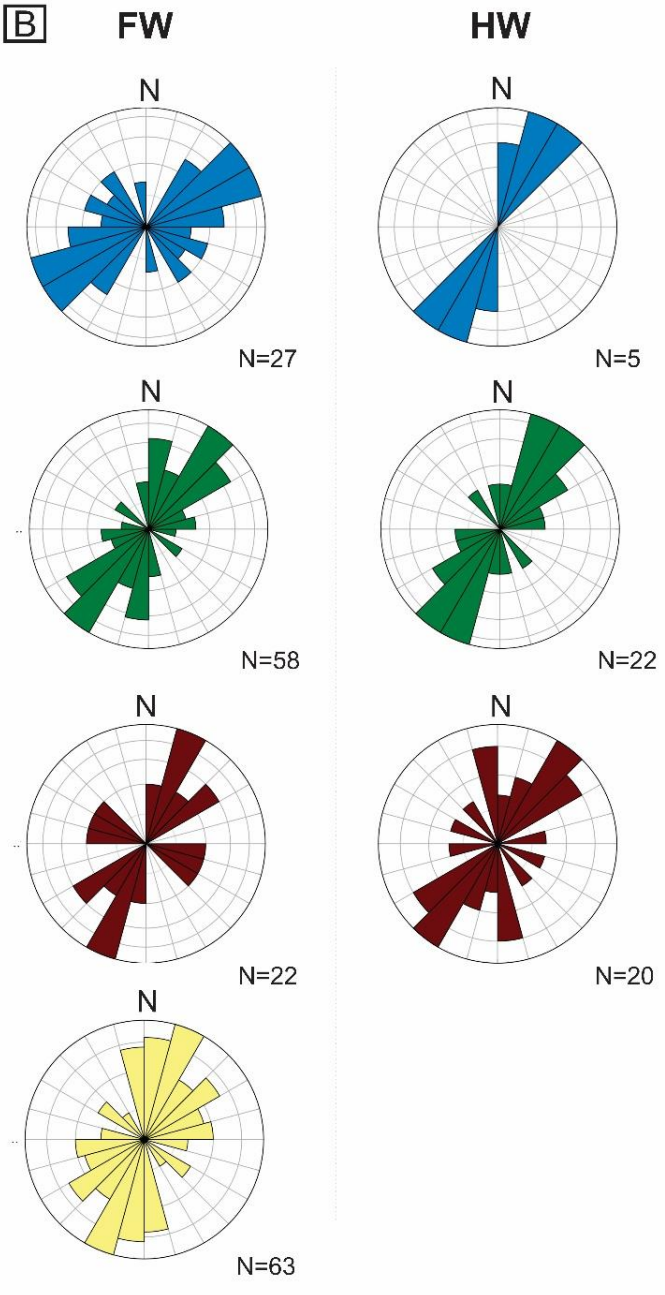
B
FW
HW
N
N=27
N
N=5
N
N=58
N
N=22
N
N=22
N
N=20
N
N=63

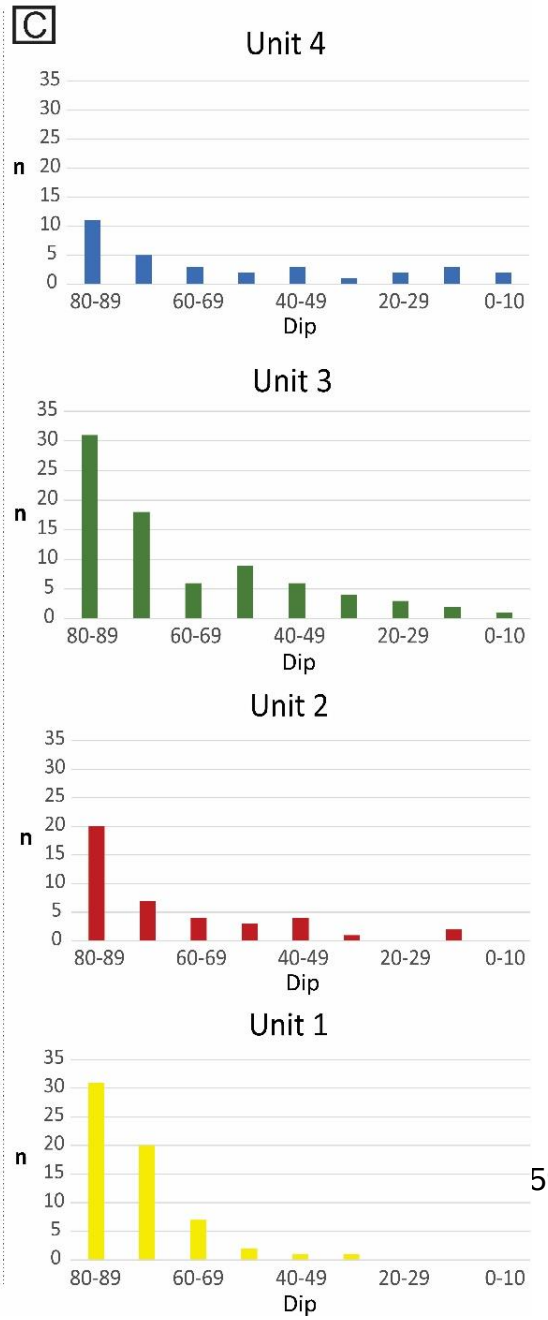
C
Unit 4
n
35
30
25
20
15
10
5
0
80-89
60-69
40-49
20-29
0-10
Dip
Unit 3
n
Dip
Unit 2
n
Dip
Unit 1
n
Dip

Figure 5 – Strike and dip behavior of deformation bands: (A) View of the vertical wall with layers, fault, and location of scanlines. (B) Rose diagrams of deformation band strike from the hangingwall (HW) and footwall (FW) (key: blue – unit 4, green – unit 3, red – unit 2, yellow – unit 1; N – number of measurements). (C) Diagrams of dip vs. the number of deformation bands (key – same colors used in (B). Also, the UCS analysis points were measured in the dashed areas.

We investigated the variation of the deformation bands strike and dip. For instance, the strike variations of the deformation bands are concentrated along the NE trend (Fig. 5B), which is the same regional trend of the Portalegre Fault. In addition, units 1 and 2 have a similar dip variation of deformation bands (Fig. 5). In contrast, units 3 and 4 exhibit a higher dip variation of deformation bands, but unit 3 has the highest frequency.

In the vertical wall, we analyzed the geometry and linkage characteristics of deformation bands (Fig. 6). Deformation bands display mutual abutting and crosscutting relationships (Figs. 6A, 6B, and 6C). Units 3 and 1 developed an anastomosed pattern of deformation bands. By contrast, units 2 and 4 produced singles linked deformation bands with no anastomosed pattern geometry (Fig. 6A and 6B).

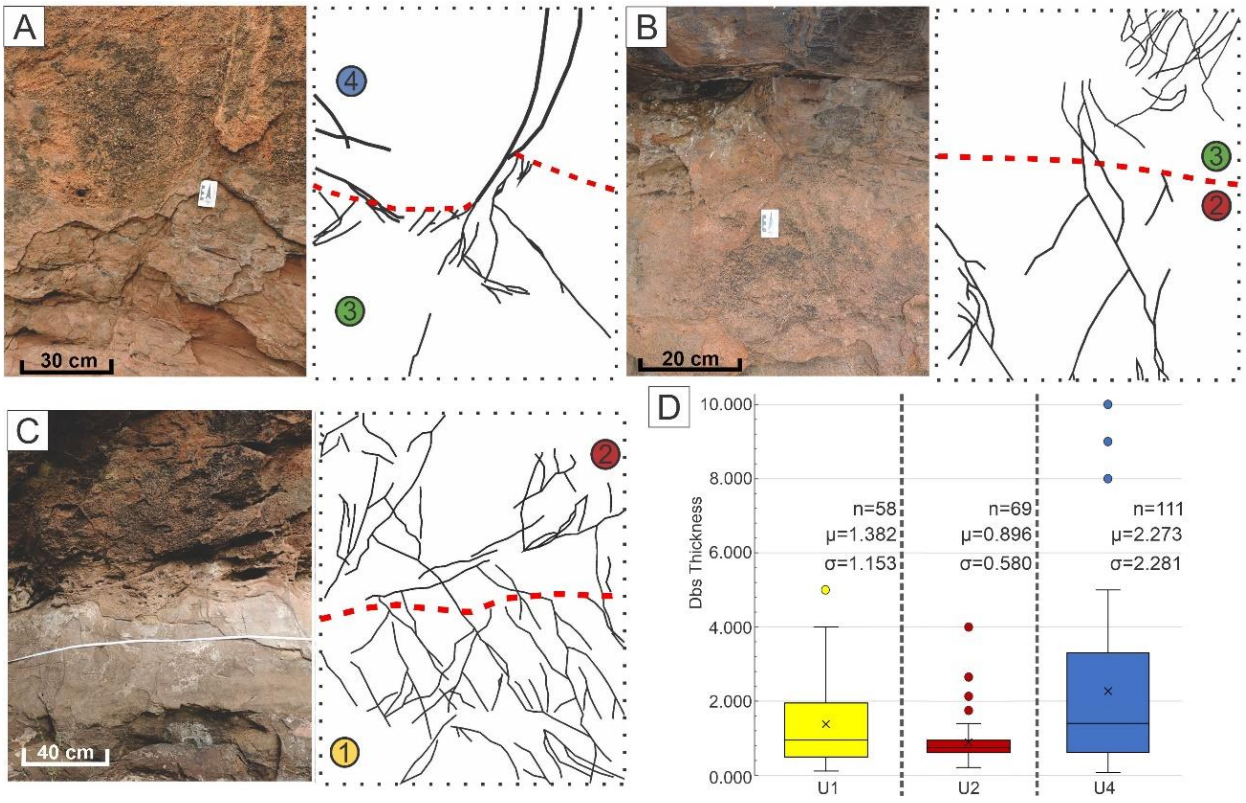

Figure 6 – Photos of the contacts between the units in the left column; lining drawings of the deformation bands and layer boundaries (red dashed line) in the central column; (A) Deformation bands crossing units 4 and 3. The thickness and the dip vary. (B) Deformation bands crossing units 3 and 2. The deformation bands in unit 3 exhibit a closed anastomosed pattern with a density of bands higher than unit 2. (C) Deformation bands crossing units 2 and 1. There is a continuous anastomosed pattern, but it is more closed and with more deformation bands in unit 1. (D) Deformation Bands Thickness from the horizontal scanlines performed in units 1, 2, and 4 are in the right column (thickness in millimeters). Fig. 2A provides photo

locations, and Fig. 4A the scanlines locations. n: number of plugs, x: medium value, σ: standard deviation, μ: average

The thickness of deformation bands changes where they cross layers and along each intersected bed (Fig. 6 A, B, and C). In this sense, unit 4 has the thicker, and unit 3 has the thinner deformation bands. Units 1 and 2 have a similar thickness variation in deformation bands. The thickness of the deformation bands was measured using scanlines PSC1 and PSC2 (Fig. 6D). PSC1 was measured on unit 4, where the thickness graphic shows the highest values to this unit. PSC2 was measured on units 1 and 2, where the thickness graphic shows higher values in unit 1 than values in unit 2.

4.1.4.3 Physical Rock Property Analyses

4.1.4.3.1 Uniaxial Compressive Strength (UCS)

We analyzed and compared the arithmetic mean of UCS in each bed (Fig. 7A). The UCS tests from the deformation bands were compared with those from the interspace area between adjacent bands. These comparisons were also performed in the hangingwall and footwall of the main fault (Fig. 7B).

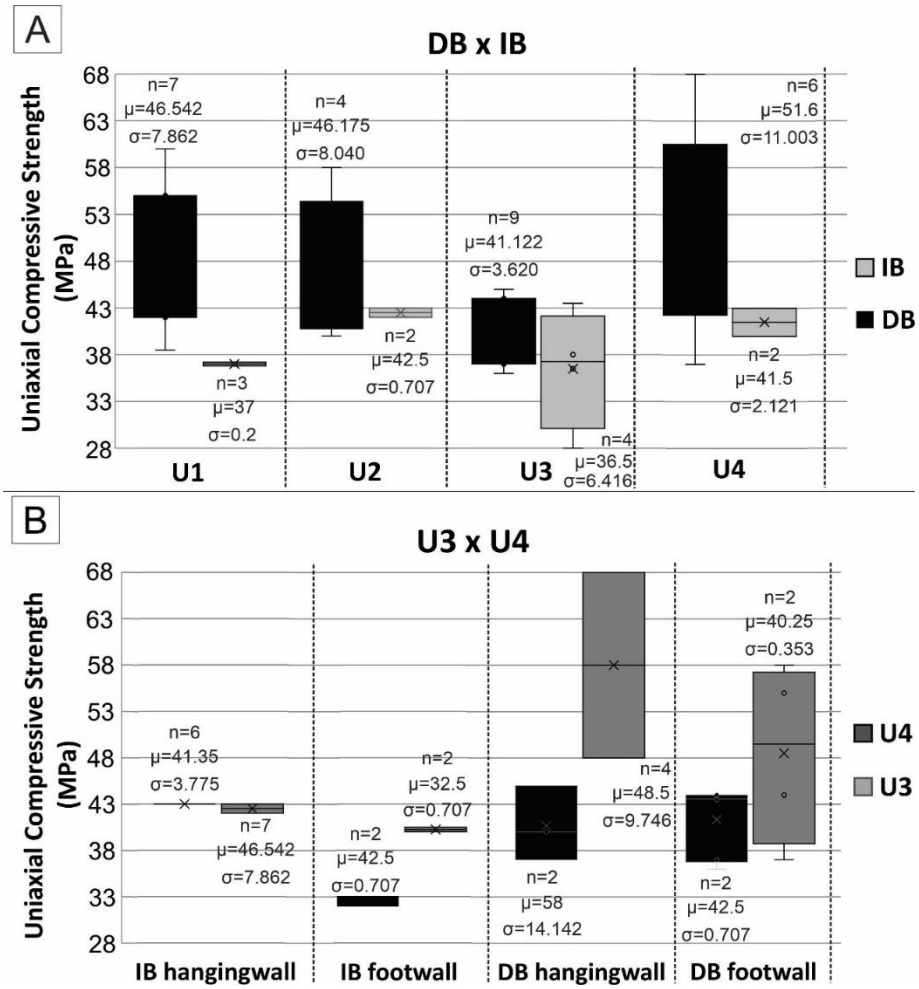

Figure 7 – Bar graphs representing the average Uniaxial Compressive Strength – UCS: (A) The average values measured at each unit on the deformation bands (DB) and in the interspace area between bands (IB). (B) Comparison of the UCS average values measured in units 3 and 4 in the hangingwall and footwall. U1: Unit 1; U2: Unit 2; U3: Unit 3; U4: Unit 4; x: medium value; σ: standard deviation; μ: average.

In the deformation bands, units 1 and 2 yielded average UCS equivalent values of 46.0 MPa, while units 4 and 3 yielded the highest and lowest values of 52.0 and 41.0 MPa, respectively (Fig. 7A). These UCS values increase with grain size. For example, coarse grain size (unit 4) yields high UCS values, whereas fine grain size (unit 3) yields low UCS values.

Unit 4 has deformation bands thicker than the other units, which yielded the highest UCS average values (58.0 MPa in the hangingwall; 48.0 MPa in the footwall) (Fig. 7B). Moreover, unit 4 is a pebbly sandstone and exhibits a grain size higher than other units. Although these sedimentary characteristics from unit 4 lead to more UCS resistance, they also lead to a higher UCS average value in unit 2 (43.0 MPa) on the deformation bands interspace.

We compared the UCS average values from units 3 and 4 of the fault hangingwall and footwall (Fig. 7B). Furthermore, units 1 and 2 were not accessed in this analysis because unit 1 is not exposed in the hangingwall, and unit 2 is partly eroded. In general, the hangingwall values are the highest than the footwall. This is consistent with the deformation bands (58.0 MPa - U4) and interspace area between bands (43.0 MPa - U3 and U4). Therefore, this portion is tougher than the footwall in both units.

In the interspace between deformation bands, the UCS values follow the same trend as those of the deformation bands. This trend shows that the UCS values increase with grain size (Fig. 7A). The deformation bands interspace in unit 3 exhibits the lowest average value of 35.0 MPa, which increases to 37.0 MPa in units 1, and 41.5 MPa in unit 4 (Fig. 7A). The only exception occurs in unit 2, with the highest UCS values (43.0 MPa).

We also compared the UCS behavior of deformation bands and their interspace in the hangingwall and footwall of the main fault using the data from units 3 and 4, exposed in the vertical wall. The UCS values of deformation bands interspace from units 3 and 4 have few variations (43.0 MPa – both units in hangingwall; 33.0 MPa in U3 and 40.0 MPa in U4 in footwall). Also, deformation bands from unit 4 have the highest average value (58.0 MPa) in the fault hangingwall. The opposite occurs in unit 3 (40.0 MPa), but with less variation of the UCS average values. Finally, two main piece of evidence were highlighted by this analysis: (a) the deformation bands in the hangingwall exhibit UCS average values higher than those in the footwall in both units 3 and 4; (b) the UCS values of the deformation bands and their interspace are directly proportional to the grain size.

4.1.4.3.2 Porosity, Permeability, Young's modulus, Poisson's Ratio Analyses, and 3D Modeling

We measured the arithmetic mean values of petrophysical properties in each unit, such as porosity, permeability, Young's modulus, and Poison ratio (Fig. 8A, 8B, 8C, and 8D). To measure these properties, the grain density used varies between 2.58 g/cm³ and 2.63 g/cm³. However, one of the samples from unit 1 has a different density (2.66 g/cm³) from the others due to carbonate cement, which we confirmed with hydrochloric acid.

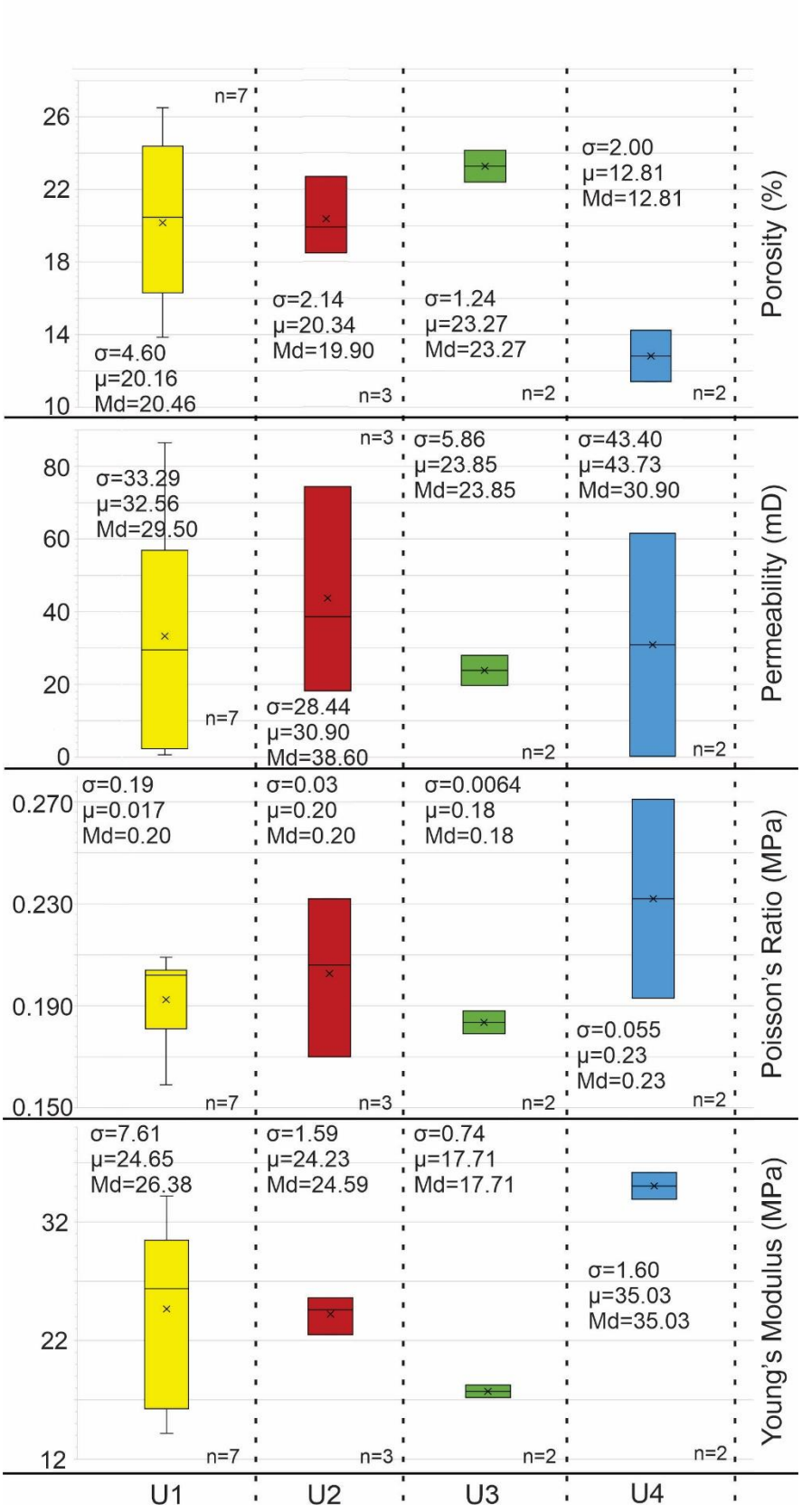
Porosity (%)
26
22
18
14
10
n=7
σ=4.60
μ=20.16
Md=20.46
σ=2.14
μ=20.34
Md=19.90
n=3
σ=1.24
μ=23.27
Md=23.27
n=2
σ=2.00
μ=12.81
Md=12.81
n=2
Permeability (mD)
80
60
40
20
0
σ=33.29
μ=32.56
Md=29.50
n=7
n=3
σ=28.44
μ=30.90
Md=38.60
σ=5.86
μ=23.85
Md=23.85
n=2
σ=43.40
μ=43.73
Md=30.90
n=2
Poisson's Ratio (MPa)
0.270
0.230
0.190
0.150
σ=0.19
μ=0.017
Md=0.20
n=7
σ=0.03
μ=0.20
Md=0.20
n=3
σ=0.0064
μ=0.18
Md=0.18
n=2
σ=0.055
μ=0.23
Md=0.23
n=2
Young's Modulus (MPa)
32
22
12
σ=7.61
μ=24.65
Md=26.38
n=7
σ=1.59
μ=24.23
Md=24.59
n=3
σ=0.74
μ=17.71
Md=17.71
n=2
σ=1.60
μ=35.03
Md=35.03
n=2
U1
U2
U3
U4

Figure 8 – Result of petrophysical properties (porosity, permeability, Poisson's ratio, and Young's modulus) measured in plugs of each sedimentary unit with deformation bands –. N: number of plugs, Md: median, x: medium value, *σ: standard deviation,* μ: average.

4.3.2.1 Porosity and Permeability

The average porosity values of sedimentary units 1 and 2 are similar (porosity 20.16 and 20.34 %, respectively) (Fig. 8A). The average porosity values indicate that stratigraphic unit 3 exhibits the highest average porosity (23.27 %), whereas unit 4 shows the lowest average porosity (12.81 %). Besides, the standard deviation values of units 2 and 4 are similar (2.14 and 2.00, respectively), and unit 1 shows the highest value (4.60) while unit 3 shows the lowest (1.24) standard deviation value.

Regarding the permeability measurements, unit 4 shows the highest average values (43.73 mD), whereas unit 3 exhibits the lowest values (23.85 mD) (Fig. 8B). Thus, even though unit 3 indicates the highest porosity, their average permeability value is the lowest, possibly related to their unconnected porosity. However, like the porosity values, the permeability values are similar in units 1 and 2 (33.29 mD and 30.90 mD). Moreover, the standard deviation values of units 1 and 2 are medium values (33.29 and 28.44, respectively) and unit 4 (43.40) shows the highest value while unit 3 (5.86) shows the lowest standard deviation value.

4.1.4.3.2.1*Poisson's Ratio and Young's Modulus*

Regarding the Poisson ratio, the lowest average values were documented in units 1 and 3 (0.19 MPa and 0.18 Mpa, respectively). Differently, the highest average values were measured in units 4 and 2 (0.23 Mpa and 0.20 Mpa, respectively) (Fig. 8C). Therefore, units 2 and 4 have the highest means of UCS and Poisson's ratio. We attributed these higher values to carbonate cement in unit 2, giving the rock greater cohesion. In addition, these units have the thickest deformation bands (see item 4.1.1), which correspond to sandstones with the highest grain size. Also, the standard deviation values of units 2 and 4 are similar (0.03 and 0.05, respectively), and unit 1 shows the highest value (0.19) while unit 3 shows the lowest standard deviation value (0.0064). Concerning Young's modulus, the highest average value occurs in unit 4 (35.04 MPa), and the lowest average value occurs in unit 3 (17.71 MPa), whereas units 1 and 2 shows intermediate values (24.66 MPa and 24.23 MPa, respectively) (Fig. 8D). We can relate porosity with Young's modulus by comparing the average petrophysical parameter values from units 1 and 2. These results vary less than 1. In addition, the standard deviation values of units 2 and 4 are similar (1.59 and 1.60, respectively), and unit 1 shows the highest value (7.61) while unit 3 shows the lowest standard deviation value (0.74).

4.1.4.3.2.2 Petrotyping

We compared the petrophysical data with typical reservoir values. The petrophysical parameters of permeability and porosity plot in the GHE basemaps (Fig. 9) are located in the lower 3 GHE bands, resulting in three petrotypes. However, these results exhibit low permeability. The porosity of units varies between 11.40% to 26.50%, and the permeability varies between 0.21 mD to 86.50 mD. Some plugs are plotted outside the basemap area because they exhibit very low permeability values, which correspond to pores that are not connected or the cementation that fills the rock porous. The results plot in the trends GHE 1, 2, and 3 correspond to 3 petrotypes of rocks with the lowest porosity and permeability in the basemap (Fig. 9).

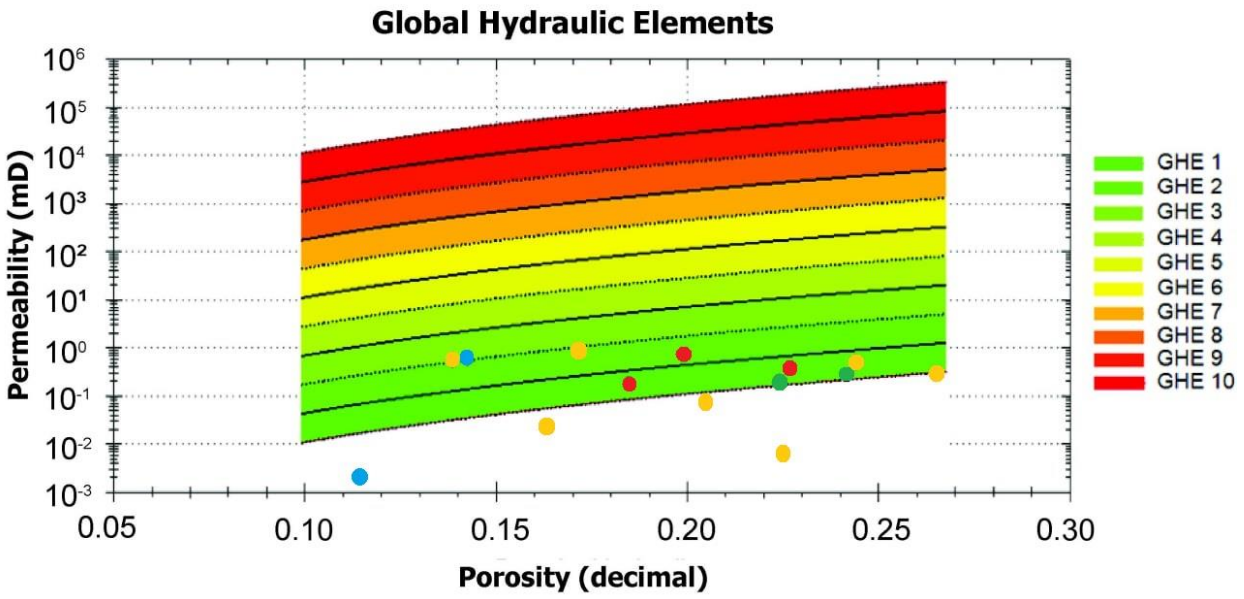

Figure 9 – GHE classification to the 14 plugs from the four sedimentary units. The GHE limits were defined by the Flow Zone Indicator (FZI) parameter. Units 1, 2, 3, and 4 are represented to the point with colors yellow, red, green, and blue, respectively.

4.1.4.3.2.3 Porosity and Permeability 3D Models

There are many methods for simulating the spatial distribution of a regionalized variable. The Gaussian, however, is the simplest way to create a regionalization that honors local data and a variogram (Pyrcz and Deutsch, 2014). To build the 3D model, we used the DTM (Fig. 10A) processed from drone imagery from the outcrop (Fig. 10B). A point dataset was created using the permeability information of different rock plugs collected in the field to populate the static model with estimated reservoir permeability values (Fig. 10C). The 3D geologic model (Fig. 10D) was divided into four zones, totalizing 17360 cells (40 x 31 x 14). These data were upscaled to the grid and populated with a geostatistical Sequential Gaussian Simulation algorithm (Deutsch and Journel, 1998) in the petrophysical modeling process (Fig. 10D, 10E, and 10F). Petrophysical

properties are modeled according to the scale of heterogeneities and the amount of data available and must be assigned to every cell in the geological model.

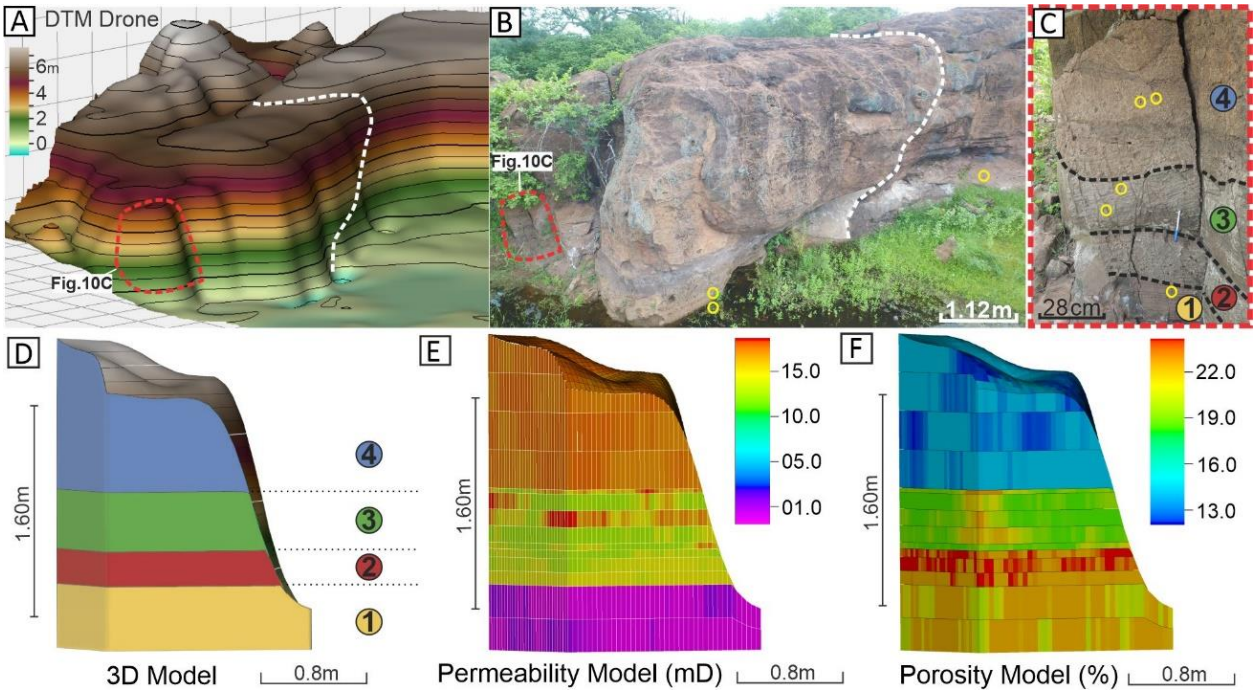

Figure 10 – The 3D model of the outcrop: (A) Digital Terrain Model (DTM) where the petrophysical data were collected (dotted area in red). The main fault is drawn in the white dashed line. (B) Drone view of the outcrop showing the modeled area. (C) Part of the outcrop where we collected the plugs in each layer (layer boundaries dashed in black), modeled and represented in (D), (E), and (F). (D) The 3D model with topography data and layers. (E) Permeability model. (F) Porosity model.

The porosity model shows that units 1 and 2 have the highest and similar values, decreasing in units 3 and 4 (Fig. 10F). Although unit 4 exhibits the lowest porosity, it has the highest permeability values in the model (Fig. 10E). Units 2 and 3 have similar permeability values. The plug used for petrophysical data of unit 1 has carbonate cement and presents the lowest permeability value.

4.1.5 Discussion

4.1.5.1 Mechanical Units and Deformation Bands

According to Laubach *et al*. (2009), it is essential to consider the host rock properties to understand the role of mechanical stratigraphy in controlling fracture attributes. In the present work performed in porous sandstones, we found that layers with different properties (thickness, competency, UCS, grain size, porosity, permeability, Poisson's ratio, and Young's moduli) have deformation bands with different structural attributes (i.e., dip values, frequency, geometry, and thickness) (Fig. 11). The above mentioned parameters were already described in mechanical stratigraphy studied from different rock types in outcrops or well data (Bai *et al.,*2002; Cawood and Bond, 2018;

Dashit *et al*., 2018; Lavenu and Lamarche, 2018; Giuffrida *et al.*, 2019; Balsamo *et al.*, 2020; Skurtveit *et al*., 2021).

The four sedimentary layers identified in this study have different thicknesses and correspond to mechanical units hosting deformation bands with different attributes, as summarized in Figure 11. For instance, coarse-grained unit 4 has the lowest frequency of thick deformation bands, while fine-grained unit 3 has a greater frequency of thin deformation bands.

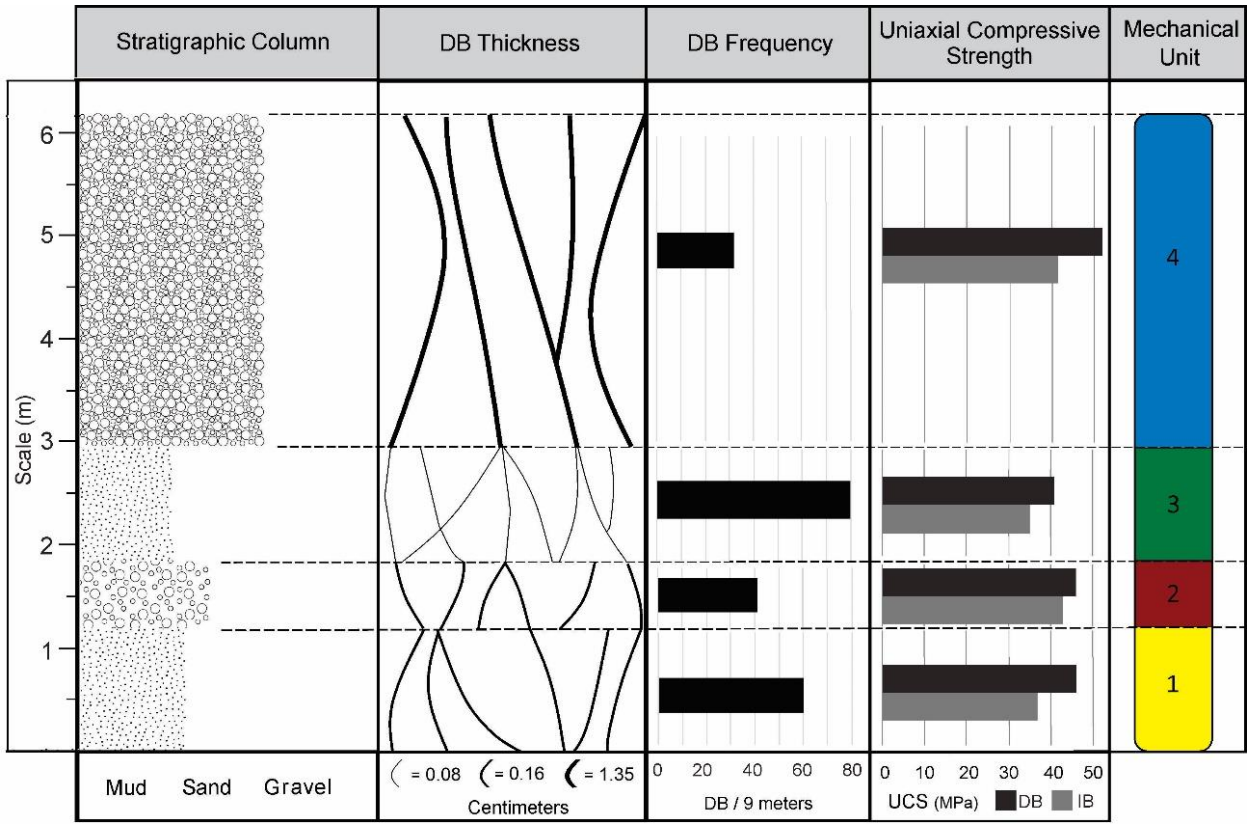

Figure 11 – Mechanical units compare the layer's mechanical behavior and the average parameters as deformation bands frequency, thickness, geometry, and Uniaxial Compressive Strength. DB: Deformation Bands, IB: Interspaces of Deformation bands.

Recent studies in faulted sandstone suggest that the spacing of deformation bands may be controlled by layer thickness (Saillet and Wibberley, 2010). A relationship between the spacing of strata-bound deformation bands and layer thickness is also recently described by Elphick *et al.* (2021). In our study, the correlation of mechanical unit thickness versus deformation bands density in Figure 12 suggests that thickness does not directly control the deformation bands frequency, as shown by the data scattering. This finding is different from low porosity layered sedimentary rocks, where layer thickness is commonly the main parameter controlling the fracture spacing, with a greater number of faults/fractures in the thinnest layers, although such a simple relationship is

not always valid, particularly in fault zones (Ackermann *et al.,* 2001; Benedicto *et al.,* 2003; Dempsey *et al.,* 2012; Ferril *et al.,* 2017; Laubach *et al.,* 2018; Ortega *et al.,* 2010).

Figure 12 indicates that deformation band frequency shows a positive linear correlation with the host rock porosity and an inverse correlation with the Young's modulus. Mechanical units with the smaller grain size, highest porosity, and lowest Young's modulus average values result in the highest frequency of the deformation bands.

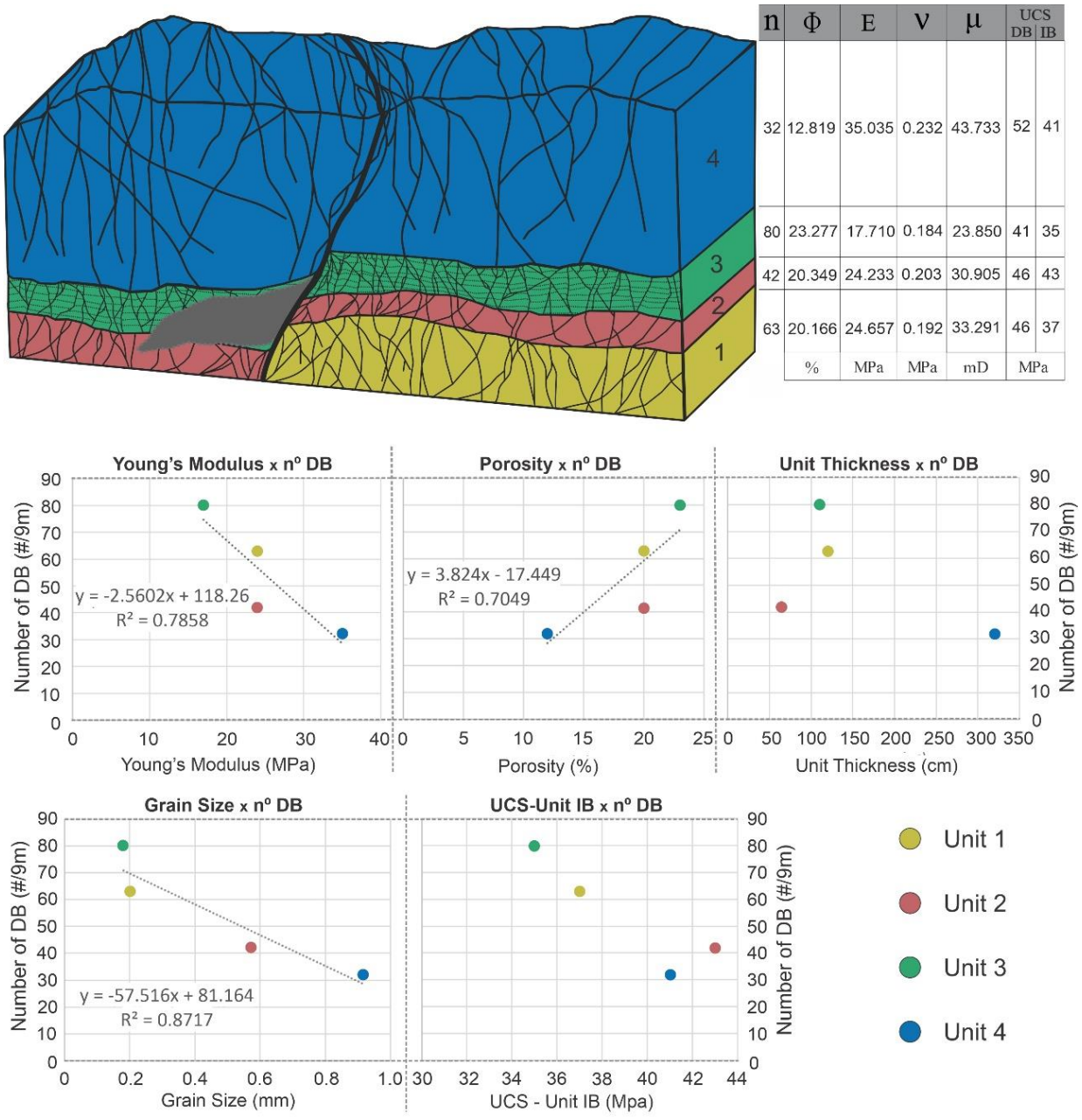

n	Φ	E	ν	μ	UCS DB	UCS IB
32	12.819	35.035	0.232	43.733	52	41
80	23.277	17.710	0.184	23.850	41	35
42	20.349	24.233	0.203	30.905	46	43
63	20.166	24.657	0.192	33.291	46	37
	%	MPa	MPa	mD	MPa	

Figure 12 – 3D outcrop model shows the relationship between the deformation bands and layers. The mechanical units are defined with all structural, sedimentary, and physical parameters described in the right

column. The graphics compare the density of deformation bands to Young's modulus, porosity, unit thickness, grain size, and UCS interspace between bands average values for each layer. Each color indicates the different layers described in our study. n: number of deformation bands/9 meters, Φ: average porosity, E: average Young's modulus; v: average Poisson ratio; μ: average permeability.

4.1.5.2 Influences of Different Mechanical Units in Deformation Bands Development

Sedimentary structure as the planar bedding is present in the mechanical unit with greater deformation bands frequency (Fig. 2D). The present study indicates that internal stratifications also form weakness plans that behave as an anisotropic medium. This sedimentary effect was also documented in other studies, showing that sedimentary parameters such as internal stratification and the nature of bed-to-bed interface influence deformation (Ringrose and Corbett, 1994; Loveless *et al*., 2011). Muscovites and biotites can contribute to the greater accommodation of deformation in the layer because they are more malleable minerals that respect feldspar and quartz that make up the other layers. This deformation was also shown in studies discussing how important is the mineralogy control on deformation band mechanisms (Fossen *et al.,* 2017; Araujo *et al*., 2018).

The thickest sedimentary package, which corresponds to unit 4, has the lowest deformation band frequency (Fig. 5). Preview study shows shear bands in sandstones layers are not influenced by grain size or bed thickness (Ballas *et al*., 2014). Torabi *et al*. (2019) showed different mechanical properties from layers of sandstones and shales that the deformation behaved ductility. (Fig. 5). Based on our results, we suggest that thicker layers may inhibit deformation bands development and attitude changes.

In our study, the most porous layer (unit 3) has a greater number of deformation bands. This unit, which also has the smallest grain size, shows a competence contrast compared with other beds, which also influences UCS behavior, decreasing this mechanical property. Therefore, we propose that in an heterolithic siliciclastic sequence, the most porous and incompetent layers tend to deform relatively more easily via deformation band development, accommodating significant deformation before breaking or bending (Willis, 1893).

Though the deformation bands described in the four units derive from the same deformation event, we reported variations in the deformation band dip from one mechanical unit to another (Figs. 4 and 5). Previews studies confirm that the variation of the fault planes could occur due to contrasting bed competencies (Antonellini and Aydin, 1995; Rawling and Goodwin, 2006). This behavior was also observed in faults by Ferrill and Morris (2003) and Morris *et al*. (2009b), showing that different properties of the mechanical units influence fault geometry and linking characteristics. The units with the greatest grain size (2 and 4) also display the geometry of deformation bands and mutual abutting and crosscutting relationships, which show as single structures linking each other. Therefore, the deformation bands frequency is directly correlated to the

anastomosed pattern of deformation bands. Besides, the anastomosed deformation bands occur in the units with the lowest grain size – unit 3, which indicates that the grain size of host rock also influences the linkage process of these structures. The anastomosed geometry of the deformation bands can significantly impact the fluid flow in siliciclastic reservoirs (Fossen and Bale, 2007; Fossen *et al*., 2007; Zuluaga *et al*., 2016; Fossen *et al*., 2017; Romano *et al*., 2020).

In our study, the mechanical unit with the highest frequency of deformation bands exhibits the lower deformation bands UCS, not showing greater cohesion as expected when increasing deformation (Figs. 11 and 12). We observed that unit 4 has a high UCS and low porosity. These characteristics may be related to the larger grain size, as confirmed by recent studies (Del Sole and Antonellini, 2019; Del Sole *et al*., 2020). It is worth mentioning the same to the Pontes *et al*. (2019) results, who stated a reduction in porosity with an increase in UCS by increasing the rock's cohesion in the arkosic sandstones of the RPB, the same geological unit analyzed in this study. The highest UCS value is related to unit 2, which is assigned to the coarser grain size with the cementation or the greatest cohesion caused by deformation (Fig. 2G). Additionally, in our interpretation, the process that resulted in the generation of the deformation bands occurred before the cementation process. We based this interpretation on the fact that the cementation process, if it occurs first, would reduce the porosity of the host rock and may preclude the formation of deformation bands, which require around 15% porosity to form (Fossen *et al*., 2017).

In addition, Nicchio *et al.* (2018) and Araujo *et al*. (2018) confirmed that (1) significant porosity reduction occurs inside the cataclastic band in the RPB; (2) the clustered zones of deformation bands and slip surfaces are observed only in coarse sandstones. Besides the grain size, the grain shape variations are also documented as a relevant parameter for the formation and development of rock deformation (Rawling and Goodwind, 2003; Aydin *et al*., 2006; Zambrano *et al.,* 2017). In our study, comparing the porosity and grain size to deformation bands density in each layer, we observed that where the layer has greater porosity and smaller grain size, there is a higher density of thinner deformation bands. Therefore, we suggest that grain size impacts deformation bands thickness and the deformation development in the finer grain of feldspar, confirming previous studies (Fossen *et al.*, 2007; Enxer and Tschegg *et al.,* 2012; Ballas *et al.,* 2014).

4.1.5.3 Implications for Siliciclastic Reservoirs

The petrophysical characteristics of our study area are consistent with Type 4 fractured reservoirs (Nelson, 2001). This type of reservoir exhibit fractures that act as flow barriers, inducing compartmentalization and anisotropy in the reservoir. In our case, deformation bands play the role of these fractures and potentially impact the fluid flow acting as fluid barriers (e.g., Caine and Minor, 2009; Balsamo and Storti, 2010) or provide

partial fluid compartmentalization (Medeiros *et al*., 2010). Some studies analyzed the parameters of porosity and permeability of deformation bands to understand how they affect the petrophysical properties of the host rocks (Antonellini and Aydin, 1994; Alikarami *et al*., 2013; Del Sole *et al*., 2020; Torabi *et al*., 2020). Our study compared porosity and permeability using the GHE method and built 3D models of these properties. Sedimentary layers with distinct mechanical behavior can present different petrophysical properties, which occur when these layers are affected by deformation bands (Underhill and Woodcock, 1987). The distribution of deformation bands varies according to the sedimentary parameters such as internal stratification, the nature of the bed-to-bed interface, and their mineralogy arrangement (Ringrose and Corbett, 1994; Loveless *et al*., 2011; Fossen *et al.,* 2017; Araujo *et al*., 2018; this study). Our 3D models (Figure 10) show a vertical variation of petrophysical properties controlled by the mechanical-stratigraphic parameters of each layer. For instance, units 1 and 4 show high and low porosity values, respectively. In contrast, units 1 and 4 exhibit low and high permeability values, respectively (Figure 10E and F). The relation between porosity and permeability shows a power-law distribution (Torabi *et al*., 2013). Additionally, we found that the thickness of sedimentary layers influences petrophysical properties. Therefore, we assume that mechanical-stratigraphic parameters (internal stratification, bed thickness, grain size) influence petrophysical properties (Fig. 10).

Also, we observed these impacts in the petrophysical properties are demonstrated using petrotyping analysis. The GHE method was used for different rocks in other studies (Corbett and Potter, 2004; Vik *et al*., 2013; Corbett *et al*., 1987). Our results showed that most samples plot in the GHE 1, 2, and 3 trends (Fig. 8). It indicates petrotypes with the lowest porosity/permeability. We assign that deformation bands and sedimentary parameters induce a reduction of these properties and indicate compaction concerning the host rock. Despite the compaction process, it would not fit entirely to Type 4 of the classification of fractured reservoirs (Nelson, 2001) since the deformation bands do not behave strictly as barriers considering that they allow flow fluids (Medeiros *et al*., 2010). Thus, the distribution and abundance of deformation bands affect reservoir production (Gibson, 1998). However, understanding how porosity/permeability reductions in deformation bands affect reservoir production needs data beyond outcrop analog analyses.

The thickness variations of the deformation bands represent an essential control on how these structures affect fluid flow (Fossen and Bale, 2007; Fossen *et al*., 2007; Torabi and Fossen, 2009; Rotevatn *et al*., 2013; Saillet and Wibberley, 2013; Fossen *et al*., 2017). According to Caine and Minor (2009), deformations can strengthen the rock through mechanical compaction and loss of porosity, which could be caused by deformation bands compaction (Del Sole and Antonellini, 2019; Pizzati et al., 2020). The mechanical unit 4 has a higher UCS on the deformation bands, and its deformation bands

are also thicker (Fig. 6), with less porosity (Fig. 8). These characteristics are consistent with bed compaction.

The porosity/permeability 3D models in the RPB (Fig. 10) allow us to analyze how the mechanical layers could be grouped according to different parameters (Fig. 12). Our model also can represent the vertical heterogeneities, such as the petrophysical properties of the stratigraphic layers with deformation bands. Other studies used the 3D modeling approach with petrophysics data to understand mechanical stratigraphy at the reservoir scale (Smart *et al*., 2014; Aldred and Sritongthae, 2015; Ali *et al*., 2019). Although it is not possible to predict the behavior of stratigraphy on porosity and permeability values exactly, this information can be used to improve prediction accuracy.

4.1.6 Conclusion

This study analyzes the influence of mechanical stratigraphy in the development and petrophysical properties of deformation band in arkosic sandstones of the RPB, Brazil. We proposed that the main parameters that control the mechanical stratigraphic units are based mainly on the following parameters: petrophysical, UCS, layer thickness, lateral layer continuity, grain size, and frequency, dip, thickness, geometry, and linkage of the deformation bands.

The following conclusions support that mechanical stratigraphy influences deformation band development and petrophysics. (a) Layer interfaces do not hamper the propagation of deformation bands across layers but a change in the deformation bands pattern. (b) The layer thickness does not exclusively control deformation bands. (c) Host rock grain size, porosity, and Young modulus control the frequency of deformation bands. This influence is more effective where porosity is high, grain size is fine, and the Young modulus is low. The cohesion (UCS) is higher in the deformation bands than in the host rock (interspace between DBS). Additionally, the rock cohesion (UCS) increases in the deformation bands in units with greater grain size and greater thickness. The mechanical properties of layers strongly impact the mechanical behavior of sedimentary units. These findings may have implications for fluid flow in faulted layered siliciclastic reservoirs.

4.1.7 Acknowledgments

We thank two anonymous reviewers and JSG editor Fabrizio Agosta for the careful revision and criticism, which greatly improved our manuscript. We acknowledge Schlumberger that provided the Petrel software license to the Federal University of Campina Grande. LSBO thanks Professor Patrick Cobertt from the Heriot-Watt University for allowing access to the Global Hydraulic Elements software license used in this study and his constructive comments. Our study was sponsored by Petrobras/Federal University of Campina Grande project (TC 5850.0109438.18.9) coordinated by Francisco C. C. Nogueira.

4.1.8 References

Ackermann, R. V., Schlische, R.W., Withjack M.O., 2001. The geometric and statistical evolution of normal fault systems: an experimental study of the effects of mechanical layer thickness on scaling laws. Journal of Structural Geology 23, 1803-1819. https://doi.org/10.1016/S0191-8141(01)00028-1.

Aldred, R. D., Sritongthae, W., 2015. 3D Petrophysical Modelling to Resolve Complex Reservoir Interpretation Problems: A Case Study from South East Asia. SPE/IATMI Asia Pacific Oil & Gas Conference and Exhibition. https://doi.org/10.2118/176243-MS.

Ali, M., Abdelmaksoud, A., Essa, M. A., Abdelhady, A., Darwish, M., 2019. 3D Structural, Facies and Petrophysical Modeling of C Member of Six Hills Formation, Komombo Basin, Upper Egypt. Natural Resources Research. https://doi.org/10.1007/s11053-019-09583-5.

Alikarami, R., Torabi, A., Kolyukhin, D., Skurtveit, E., 2013. Geostatistical relationship between mechanical and petrophysical properties of deformed sandstone. International Journal of Rock Mechanics & Mining Sciences. 63; 27-38. https://doi.org/10.1016/j.ijrmms.2013.06.002

Antonellini, M. A., Aydin, A., Pollard, D. D., 1994. Microstructure of deformation bands in porous sandstone at Arches National Park, Utah. Journal of Structural Geology. 16;941-959. https://doi.org/10.1016/0191-8141(94)90077-9.

Amaefule, J. O., Altunbay, M., Tiab, D., Kersey, D. G., Keelan, D. K., 1993. Enhanced reservoir description: using core and log data to identify hydraulic (flow) units and predict permeability in uncored intervals/wells. Paper SPE 26435 presented at the 68th Annual Technical Conference and Exhibition, Houston, TX, USA. https://doi.org/10.2118/26436-MS.1993.

Araujo, R. E. B., Bezerra, F. H. R., Nogueira, F. C. C., Balsamo, F., Carvalho, B. R. B. M., Souza, J. A. B., Sanglard, J. C. D., De Castro, D. L., Melo, A. C. C., 2018. Basement control on fault formation and deformation band damage zone evolution in the Rio do Peixe Basin, Brazil. Tectonophysics. https://doi.org/10.1016/j.tecto.2018.08.011.

ASTM, 2001. Standard test method for determination of rock hardness by rebound hammer method. West Conshohocken: ASTM International.

Aydin, A., Basu, A., 2005. The Schmidt hammer in rock material characterization. Engineering Geology 81, 1–14. https://doi.org/10.1016/j.enggeo.2005.06.006.

Aydin, A., Borja, R.I., Eichhubl, P., 2006. Geological and mathematical framework for failure modes in granular rock. Journal of Structural Geology 28, 83–98. https://doi.org/10.1016/j.jsg.2005.07.008.

Aydin, A., 1978. Small Faults Formed as Deformation Bands in Sandstone. Pure and Applied Geophysics, 116, 913–930. https://doi.org/10.1007/BF00876546.1978.

Bai, T., Maerten, L., Gross, M. R., Aydin, A., 2002. Orthogonal cross joints: do they imply a regional stress rotation?. Journal of Structural Geology. V. 24, pp. 77-88. https://doi.org/10.1016/S0191-8141(01)00050-5.

Bai, T., Pollard, D., 2000. Fracture Spacing in Layered Rocks: A New Explanation Based on the Stress Transition. Journal of Structural Geology 22(1):43-57. https://doi.org/10.1016/S0191-8141(99)00137-6.

Ballas, G., Soliva, R., Benedicto, A., Sizun, J.-P., 2014. Control of tectonic setting and large-scale faults on the basin-scale distribution of deformation bands in porous sandstone (Provence, France), Marine and Petroleum Geology, V. 55, p. 142-159. http://dx.doi.org/10.1016/j.marpetgeo.2013.12.020.

Balsamo, F., Storti, F., 2010. Grain size and permeability evolution of soft-sediment extensional sub-seismic and seismic fault zones in high-porosity sediments from the Crotone basin, southern Apennines, Italy. Marine and Petroleum Geology, 27, p. 822-837. https://doi.org/10.1016/j.marpetgeo.2009.10.016.

Balsamo, F., Bezerra, F. H. R., Vieira, M. M., Storti, F., 2013. Structural control on the formation of iron oxide concretions and Liesegang bands in faulted, poorly lithified Cenozoic sandstones of the Paraiba basin, Brazil. Geological Society of America Bulletin, v. 125, p. 913-931, doi:10.1130/B30686.1.

Balsamo, F., Bezerra, F. H. R., Klimchouk, A. B., Cazarin, C. L., Auler, A. S., Nogueira, F. C., Pontes, C. C. C., 2020. Influence of fracture stratigraphy on hypogene cave development and fluid flow anisotropy in layered carbonates, NE Brazil. Marine and Petroleum Geology. V. 114, 104207. https://doi.org/10.1016/j.marpetgeo.2019.104207.

Benedicto, A., Schultz, R. A., Soliva, R., 2003. Layer thickness and the shape of faults, Geophys. Res. Lett., 30(20), 2076, doi:10.1029/2003GL018237.

Bense, V. F., Person, M. A., 2006. Faults as conduit-barrier systems to fluid flow in siliciclastic sedimentary aquifers. Water Resources Research 42, W05421. https://doi.org/10.1029/2005WR004480.

Bertotti, G., Hardebol, N., Koppen, T. J. K., Luthi, S. M., 2007. Toward a quantitative definition of mechanical units: New techniques and results from an outcropping deep-water turbidite succession (Tanqua-Karoo Basin, South Africa), Geohorizons. https://doi.org/10.1306/03060706074.

Caers, J., 2005. Petroleum Geostatistics. 1 Ed. Society of Petroleum Engineers, Texas, 88 P.

Caine, J. S., Minor, S. A., 2009. Structural and geochemical characteristics of faulted sediments and inferences on the role of water in deformation, Rio Grande Rift, New Mexico. Geological Society of America Bulletin, v. 121; no. 9/10; p. 1325–1340. https://doi.org/10.1130/B26164.1.

Cardozo, N., Allmendinger, R. W., Morgan, J. K., 2005. Influence of mechanical stratigraphy and initial stress state on the formation of two fault propagation folds. Journal of Structural Geology. V 27, 1954- 1972. Doi:10.1016/j.jsg.2005.06.003.

Carvalho, I. S., Mendes, J. C., Costa, T., 2013. The role of fracturing and mineralogical alteration of basement gneiss in the oil exhsudation in the Sousa Basin (Lower Cretaceous), Northeastern Brazil. Journal of South American Earth Sciences 47, 47–54. https://doi.org/10.1016/j.jsames.2013.06.001.

Cawood, A. J., Bond, C. E., 2018. 3D mechanical stratigraphy of a deformed multi-layer: Linking sedimentary architecture and strain partitioning. Journal of Structural Geology. V. 106, pp. 54-69. https://doi.org/10.1016/j.jsg.2017.11.011.

Cilona, A., Baud, P., Tondi, E.,Agosta, F., Vinciguerra, S., Rustichelli, A.,Spiers, C. J., 2012. Deformation bands in porous carbonate grainstones: field and laboratory observations. Journal Structural Geology, V. 45, Pages 137-157. Doi: 10.1016/j.jsg.2012.04.012.

Cooke, M. L., Simo, J. A., Underwood, C. A., Rijken, P., 2006. Mechanical stratigraphic controls on fracture patterns within carbonates and implications for groundwater flow. Sedimentary Geology. Volume 184, Issues 3–4, 15, Pages 225-239. https://doi.org/10.1016/j.sedgeo.2005.11.004.

Corbett, K., Friedman, M., 1987. Fracture Development and Mechanical Stratigraphy of Austin Chalk, Texas. AAPG Bulletin, 71. https://doi.org/10.1306/94886D35-1704-11D7-8645000102C1865D.

Corbett, P. W. M., Potter, D. K., 2004. Petrotyping: a basemap and Atlas for navigating through permeability and porosity data for reservoir comparison and and permeability

prediction. Paper SCA 2004-30 presented at the International Symposium of the Society of Core Analysts, 5–9, Abu Dhabi, UAE.

Dashti, R., Rahimpour-Bonab, H., Zeinali, M., 2018. Fracture and mechanical stratigraphy in naturally fractured carbonate reservoirs-A case study from Zagros region. Marine and Petroleum Geology. V. 97, pp. 466-479. https://doi.org/10.1016/j.marpetgeo.2018.06.027.

de Castro, D. L., Oliveira, D. C., Castelo Branco, R. M. G., 2007. On the tectonics of the Neocomian Rio do Peixe Rift Basin, NE Brazil: Lessons from gravity, magnetics, and radiometric data. J South Am Earth Sci. 24 (2–4):184–202. https://doi.org/10.1016/j.jsames.2007.04.001.

Del Sole, L., Antonellini, M., 2019. Microstructural, petrophysical, and mechanical properties of compactive shear bands associated to calcite cement concretions in arkose sandstone. Jornal Structural Geology. 126, 51–68. https://doi.org/10.1016/j.jsg.2019.05.007.

Del Sole, L., Antonellini, M., Calafato, A., 2020. Characterization of sub-seismic resolution structural diagenetic heterogeneities in porous sandstones: Combining ground-penetrating radar profiles with geomechanical and petrophysical in situ measurements (Northern Apennines, Italy). Marine and Petroleum Geology, V. 117, July, n 104375. https://doi.org/10.1016/j.marpetgeo.2020.104375.

Dempsey, D. E., Ellis, S. M., Rowland, J. V., Archer, R.A., 2012. The role of frictional plasticity in the evolution of normal fault system. Journal of Structural Geology 39, pp. 122-137. https://doi.org/10.1016/j.jsg.2012.03.001.

de Souza., D. H., Nogueira, F. C. C., Vasconcelos, D. L., Torabi, A., Souza, J. A. B., Nicchio, M. A., Pérez, Y. A. R., Balsamo, F., 2021. Growth of cataclastic bands into a fault zone: A multiscalar process by microcrack coalescence in sandstones of Rio do Peixe Basin, NE Brazil. Journal of Structural Geology 146, 104315. https://doi.org/10.1016/j.jsg.2021.104315

Deutsch, C. V., Journel, A. G. Gslib: Geostatistical Software Library and Users Guide. Oxford University Press, New York, 2 Editions, 1998.

Elphick, K. E., Lv, A., Roshan, H., Sloss, C. R., Regenauer-Lieb, K., Schrank, C. E., 2021. Regular spacing of deformation bands in sandstone: Layer-thickness control or constitutive instability? Journal of Structural Geology, Volume 147,104335. https://doi.org/10.1016/j.jsg.2021.104335.

Exner, U., Tschegg, C., 2012. Preferential cataclastic grain size reduction of feldspar in deformation bands in poorly consolidated arkosic sands. Journal of Structural Geology, V. 43, P. 63-72. https://doi.org/10.1016/j.jsg.2012.08.005.

Ferrill, D. A., Morris, A. P., 2003. Dilational Normal Faults: Journal of Structural Geology, V. 25, P. 183–196. https://doi.org/10.1016/S0191-8141(02)00029-9.

Ferrill, D. A., Morris, A. P., 2008. Fault zone deformation controlled by carbonate mechanical stratigraphy, Balcones fault system, Texas. American Association of Petroleum Geologists. 92, 359-380. https://doi.org/10.1306/10290707066.

Ferrill, D. A., Morris, A. P., McGinnis, R. N., 2009. Crossing conjugate normal faults in field exposures and seismic data. American Association of Petroleum Geologists. 93, 1471-1488. https://doi.org/10.1306/06250909039.

Ferrill, D. A., Morris, A. P., Mcginnis, R. N., Smart, K. J., Wigginton, S. S., Hill, N. J., 2017. Mechanical Stratigraphy and Normal Faulting. Journal of Structural Geology. https://doi.org/10.1016/j.jsg.2016.11.010.

Fossen, H., Bale, A., 2007. Deformation bands and their influence on fluid flow. The American Association of Petroleum Geologists, v. 91, no. 12, pp. 1685–1700. https://doi.org/10.1306/07300706146.

Fossen, H., Schultz, R., Shipton, Z. K., Mair, K., 2007. Deformation bands in a sandstone: a review. Journal of the Geological Society of London. v. 164, p. 755-769. http://dx.doi.org/10.1144/0016-76492006-036.

Fossen, H., Schultz, R.A., Torabi, A., 2011. Conditions and implications for compaction band formation in the Navajo Sandstone, Utah. Journal of Structural Geology, 33: 1477-1490. https://doi.org/10.1016/j.jsg.2011.08.001.

Fossen, H., Soliva, R., Ballas, G., Trzaskos, B., Cavalcante, C., Schultz, R. A., 2017. A review of deformation bands in reservoir sandstones: geometries, mechanisms and distribution. Subseismic-Scale Reservoir Deformation. Geological Society, London, Special Publications, 459. https://doi.org/10.1144/SP459.4.

Françolin, J. B. L., Cobbold, P. R., Szatmari, P., 1994. Faulting in the Early Cretaceous Rio do Peixe (NE Brazil) and its significance for the opening of the Atlantic. Journal of Structural Geology, v. 16, p. 647-661. https://doi.org/10.1016/0191-8141(94)90116-3.

Gibson, R.G., 1998. Physical character and fluid-flow properties of sandstone-derived fault zones. Structural Geology in Reservoir Characterization. Geological Society,

London, Special Publications, 127, 83-97. https://doi.org/10.1144/GSL.SP.1998.127.01.07.

Giuffrida, A., La Bruna, V., Castelluccio, P., Panza, E., Rustichelli, A., Tondi, E., Giorgini, M., Agosta, F., 2019. Fracture simulation parameters of fractured reservoirs: Analogy with outcropping carbonates of the Inner Apulian Platform, southern Italy. Journal of Structural Geology. V. 123, pp. 18-41. https://doi.org/10.1016/j.jsg.2019.02.007.

Laubach, S. E., Olson, J. E., Gross, M. R., 2009. Mechanical and Fracture Stratigraphy. AAPG Bulletin, v. 93, no. 11, pp. 1413–1426. https://doi.org/10.1306/07270909094.

Laubach, S. E., Lamarche, J., Gauthier, B. D., Dunne, W. M., Sanderson, D. J., 2018. Spatial arrangement of faults and opening-mode fractures. Journal of Structural Geology, 108, pp. 2-15. https://doi.org/10.1016/j.jsg.2017.08.008.

Lavenu, A. P. C., Lamarche, J., 2018. What controls diffuse fractures in platform carbonates? Insights from Provence (France) and Apulia (Italy). Journal of Structural Geology. V. 108, pp. 94-107. https://doi.org/10.1016/j.jsg.2017.05.011.

Lindsay, N. G., Murphy, F. C., Walsh, J. J., Watterson, J., 1993. Outcrop studies of shale smears on fault surfaces. In: Fint, S.S., Bryant, I.D. (Eds.), The Geological Modelling of Hydrocarbon Reservoirs and Outcrop Analogues, vol. 15. Blackwell Scientific Publications, Oxford, pp. 11 and 123. https://doi.org/10.1002/9781444303957.ch6.

Loveless, S., Bense, V., Turner, J., 2011. Fault architecture and deformation processes within poorly lithified rift sediments, Central Greece. Journal of Structural Geology 33, 1554 -1568. https://doi.org/10.1016/j.jsg.2011.09.008.

Maciel, I. B., Dettori, A., Balsamo, F., Bezerra, F. H. R., Vieira, M. M., Nogueira, F. C. C., Salvioli-Mariani, E., Sousa J. A. B. 2018. Structural control on clay mineral authigenesis in faulted arkosic sandstone of the Rio do Peixe Basin, Brazil. Minerals 8, pp. 1-17, https://doi.org/10.3390/min8090408.

Marques Jr, A., Horota, R. K., Souza, E. M., Kupssinsku, L., Rossa, P., Aires, A. S., Bachi, L., Veronez, M. R., Gonzaga Jr, L., Cazarin, C. L., 2020. Virtual And Digital Outcrops In The Petroleum Industry: A Systematic Review. Earth-Science Reviews, 208. https://doi.org/10.1306/07270909094.

Matos, R. M. D., 1992. The northeastern Brazilian Rift System. Tectonics 11 (4), 766–791. https://doi.org/10.1029/91TC03092.

Mcquillan, H., 1974. Fracture Patterns on Kuh-E Asmari Anticline, Southwest Iran. AAPG Bull. 1177 58, 236–246. https://doi.org/10.1306/83D913C1-16C7-11D7-8645000102C1865D.

Medeiros, W. E., do Nascimento, A. F., Alves da Silva, F. C., Destro, N., Demétrio, J. G. A., 2010. Evidence of hydraulic connectivity across deformation bands from field pumping tests: Two examples from Tucano Basin, NE Brazil. Journal of Structural Geology 32, 1783–1791. https://doi.org/10.1016/j.jsg.2009.08.019

Morris, A. P., Ferrill, D. A., McGinnis, R. N., 2009. Mechanical stratigraphy and faulting in Cretaceous carbonates. AAPG Bulletin, v. 93, no. 11, p. 1459–1470. doi: 10.1306/04080909011.

Nelson, R. 1983. Geologic Analysis of Naturally Fractured Reservoir. Gulf Professional Publishing. ISBN: 9780080507293.

Nicchio, M. A., Nogueira, F. C. C., Balsamo, F., Souza, J. A. B., Carvalho, B. R. B. M., Bezerra, F. H. R., 2018. Development of cataclastic foliation in deformation bands in feldspar-rich conglomerates of the Rio do Peixe Basin, NE Brazil. Journal. Structural. Geology 107, pp. 132-141. https://doi.org/10.1016/j.jsg.2017.12.013.

Nogueira, F. C. C.; Marques, F. O., Bezerra, F. H. R., de Castro, D. L., Fuck, R. A., 2015. Cretaceous intracontinental rifting and post-rift inversion in NE Brazil: Insights from the Rio do Peixe Basin. Tectonophysics; 644: 92–107. https://doi.org/10.1016/j.tecto.2014.12.016.

Nogueira, F. C. C., Nicchio, M. A., Balsamo, F., Souza, J. A. B., Silva, I. V. L., Bezerra, F. H. R., Vasconcelos, D. L., Carvalho, B. R. B. M., 2021. The influence of the cataclastic matrix on the petrophysical properties of deformation bands in arkosic sandstones. Marine and Petroleum Geology. https://doi.org/10.1016/j.marpetgeo.2020.104825.

Ortega, O. J., Marrett, R. A., Laubach, S. E., 2006. A scale-independent approach to fracture intensity and average spacing measurement. American Association Petroleum Geology. Bullet 90, p. 193-208. doi: http://dx.doi.org/10.1306/08250505059.

Ortega, O. J., Galem J. F., Marret, R., 2010. Quantifying diagenetic and stratigraphic controls on fracture intensity in platform carbonates: an example from the Sierra Madre Oriental, northeast Mexico. Journal of Structural Geology, 32, pp. 1943-1959. https://doi.org/10.1016/j.jsg.2010.07.004.

Pizzati, M., Balsamo, F., Storti, F., Lacumin, P., 2020. Physical and chemical strain-hardening during faulting in poorly lithified sandstone: the role of kinematic stress field

and selective cementation (Crotone Basin, Italy). Geological Society of America Bulletin, v. 132 (5-6), p. 1183-1200. https://doi.org/10.1130/B35296.1

Pontes, C. C. C., Nogueira, F. C. C., Bezerra, F. H. R., Balsamo, F., Miranda, T. S., Nicchio, M. A., Souza, J. A. B., Carvalho, B. R. B. M., 2019. International Journal of Rock Mechanics and Mining Sciences 114, 153–163. https://doi.org/10.1016/j.ijrmms.2018.12.009.

Pontes, C. C. C., Bezerra, F. H. R., Bertotti, G., La Bruna, V., Audra, P., De Waela, J., Auler, A. S., Balsamo, F., De Hoop, S., Pisani, L., 2021. Flow pathways in multiple-direction fold hinges: Implications for fractured and karstified carbonate reservoirs. Journal of Structural Geology. V. 146, 104324. https://doi.org/10.1016/j.jsg.2021.104324.

Pyrcz, M. J., Deutsch, C. V., 2014. Geostatistical Reservoir Modeling. 2 Ed. Oxford University Press, 433 P.

Qu, D., Tveranger, J., Fachri, M., 2017. Influence of deformation-band fault damage zone on reservoir performance. Interpretation; 5 (4): SP41–SP56. https://doi.org/10.1190/INT-2016-0229.1.

Rapozo, B. F., Córdoba, V. C., Antunes, A. F., 2021.Tectono-stratigraphic evolution of a cretaceous intracontinental rift: Example from Rio do Peixe Basin, north-eastern Brazil. Marine and Petroleum Geology 126, 104899. https://doi.org/10.1016/j.marpetgeo.2021.104899.

Rawling, G. C., Goodwin, L. B., 2003. Cataclasis and particulate flow in faulted, poorly lithified sediments. Journal of Structural Geology 25, 313–331. https://doi.org/10.1016/S0191-8141(02)00041-X.

Rawling, G. C., Goodwin, L. B., 2006. Structural record of the mechanical evolution of mixed zones in faulted poorly lithified sediments, Rio Grande rift, New Mexico, USA. Journal of Structural Geology, V 28, I9, 1623-1639. doi:10.1016/j.jsg.2006.06.008.

Ringrose, P. S., Corbett, P. W. M.,1994. Controls on two-phase fluid flow in heterogeneous sandstones. Geological Society, London, Special Publications, 78, 141-150, 1. https://doi.org/10.1144/GSL.SP.1994.078.01.12.

Roche, V., Homberg, C., Rocher, M., 2013. Fault nucleation, restriction, and aspect ratio in layered sections: Quantification of the strength and stiffness roles using numerical modeling. J. Geophys. Res., Solid Earth, 118, 1–15. doi: 10.1002/jgrb.50279.

Romano, V., Bigi, S., Carnevale, F., Hyman, J. D., Karra, S., Valocchi, A. J., Tartarello, M. A., Battaglia, M., 2020. Hydraulic characterization of a fault zone from fracture

distribution. Journal of Structural Geology 135, 104036. http://dx.doi.org/10.1016/j.jsg.2020.104036.

Rotevatn, A. Sandve, T. H., Keilegavlen, E., Kolyukhin, D., Fossen, H., 2013. Deformation bands and their impact on fluid flow in sandstone reservoirs: the role of natural thickness variations. Geofluids, Volume 13, Issue 3 p. 359-371. https://doi.org/10.1111/gfl.12030.

Saillet, E., Wibberley, C. A. J., 2010. Evolution of cataclastic faulting in high-porosity sandstone, Bassin du Sud-Est, Provence, France. Journal Structural Geology, 32, pp. 1590-1608. https://doi.org/10.1016/j.jsg.2010.02.007.

Saillet, E., Wibberley, C. A. J., 2013. Permeability and flow impact of faults and deformation bands in high-porosity sand reservoirs: southeast Basin, France, analog. AAPG Bull. 97, 437–464. http://dx.doi.org/10.1306/09071211191.

Schueller, S., Braathen, A., Fossen, H., Tveranger, J., 2013. Spatial distribution of deformation bands in damage zones of extensional faults in porous sandstones: statistical analysis of field data. Journal of Structural Geology, 52, 148–162. https://doi.org/10.1016/j.jsg.2013.03.013.

Sénant, J., Popoff, M., 1991. Early Cretaceous extension in northeast Brazil related to the South Atlantic opening. Tectonophysics 198, 35–46. https://doi.org/10.1016/0040-1951(91)90129-G.

Silva, M. E., Nogueira, F. C. C., Pérez, Y. A. R., Vasconcelos, D. L., Stohler, R. C., Sanglard, J. C. D., Balsamo, F., Bezerra, F. H. R., Carvalho, B. R. B. M., Souza, J. A. B., 2022. Permeability modeling of a basin-bounding fault damage zone in the Rio do Peixe Basin, Brazil. Marine and Petroleum Geology. V. 135, 105409. https://doi.org/10.1016/j.marpetgeo.2021.105409.

Skurtveit, E., Torabi, A., Sundal, A., Braathen, A., 2021. The role of mechanical stratigraphy on CO2 migration along faults – examples from Entrada Sandstone, Humbug Flats, Utah, USA. International Journal of Greenhouse Gas Control. V. 109, 103376. https://doi.org/10.1016/j.ijggc.2021.103376

Smart, K. J., Ofoegbu, G. I., Morris, A. P., McGinnis, R. N., Ferrill, D. A., 2014. Geomechanical modeling of hydraulic fracturing: Why mechanical stratigraphy, stress state, and preexisting structure matter. AAPG Bulletin, v. 98, no. 11, p. 2237–2261. doi:10.1306/07071413118.

Souza, D. H. S., Nogueira, F. C. C., Vasconcelos, D. L., Torabi, A., Souza, J. A. B., Nicchio, M. A., Perez, Y. A. R., Balsamo, F., 2021. Growth of cataclastic bands into a fault zone: A multiscalar process by microcrack coalescence in sandstones of Rio do Peixe Basin, NE Brazil. Journal Structural Geology 146, 104315. https://doi.org/10.1016/j.jsg.2021.104315.

Tondi, E., Cilona, A., Agosta, F., Aydin, A., Rustichelli, A., Renda, P., Giunta, G., 2012. Growth processes, dimensional parameters and scaling relationships of two conjugate sets of compactive shear bands in porous carbonate grainstones, Favignana Island, Italy. Journal Structural Geology, V. 37, pp. 53-64. https://doi.org/10.1016/j.jsg.2012.02.003.

Tondi, E., Rustichelli, A., Cilona, A.,Balsamo, F., Storti, F., Napoli, G., Agosta, F., Renda, P., Giorgioni, M., 2016. Hydraulic properties of fault zones in porous carbonates, examples from central and southern Italy. Italian Journal of Geosciences, V, 135, 68-79. https://doi.org/10.3301/IJG.2015.08.

Torabi, A., Fossen, H., 2009. Spatial variation of microstructure and petrophysical properties along deformation bands in reservoir sandstones. AAPG Bulletin 93, 919–938. https://doi.org/10.1306/03270908161.

Torabi, A., Johannessen, M. U., Ellingsen, T. S. S., 2019. Fault Core Thickness: Insights from Siliciclastic and Carbonate Rocks. Geofluids, 1–24. doi: 10.1155/2019/2918673.

Torabi, A., Balsamo, F., Nogueira, F. C. C., Vasconcelos, D. L., Silva, A. C. E., Bezerra, F. H. R., Souza, J. A. B., 2021. Variation of thickness, internal structure and petrophysical properties in a deformation band fault zone in siliciclastic rocks. Marine and Petroleum Geology. V. 133, 105297. DOI: 10.1016/j.marpetgeo.2021.105297.

Torabi, A., Jiménez-Millán, J., Jiménez-Espinosa, R., García-Tortosa, F. R., Abad, I., Ellingsen, T. S. S., 2020. Effect of Mineral Processes and Deformation on the Petrophysical Properties of Soft Rocks during Active Faulting. Minerals, 10, 444. https://doi.org/10.3390/min10050444.

Underhill, J. R., Woodcock, N. H. Faulting mechanisms in high porosity sandstones: New Red Sandstone, Arran, Scotland, in M. E. Jones and R. M. F. Preston, eds., deformation of sediments and sedimentary rocks: Geological Society Special Publication, v, 29, p. 91–105. https://doi.org/10.1144/GSL.SP.1987.029.01.09. 1987.

Vasconcelos, D., Marques, F. O., Nogueira, F.C.C., Perez, Y.A.R., Bezerra, F. H. R., Stohler, R. C., Souza, J. A. B., 2021. Tectonic inversion assessed by integration of geological and geophysical data: The intracontinental Rio do Peixe Basin, NE Brazil. Basin Research 33, 705–728. https://doi.org/10.1111/bre.12491

Vik, B., Bastesen, E., Skauge, A., 2013. Evaluation of representative elementary volume for a vuggy carbonate rock—Part: Porosity, permeability, and dispersivity. Journal of Petroleum Science and Engineering 112:36–47. doi: 10.1016/j.petrol.2013.03.029.

Zambrano, M., Tondi, E., Mancini, L., Arzilli, F., Lanzafame, G., Materazzi, M., Torrieri, S., 2017. 3D Pore-network quantitative analysis in deformed carbonate grainstones. Marine and Petroleum Geology, V. 82, P. 251-264. https://doi.org/10.1016/j.marpetgeo.2017.02.001.

Zahm, C. K., Hennings, P. H., 2009.Complex fracture development related to stratigraphic architecture: Challenges for structural deformation prediction, Tensleep Sandstone at the Alcova anticline, Wyoming. AAPG Bulletin, V. 93, No. 11. doi: 10.1306/08040909110.

Zuluaga, L.F., Rotevatn, A., Keilegavlen, E. Fossen, H., 2016. The effect of deformation bands on simulated fluid flow within fault-propagation fold trap types: Lessons from the San Rafael monocline, Utah. American Association of Petroleum Geologists Bulletin 100 (10), 1523–1540. https://doi.org/10.1306/04151614153.

Willis, B., 1894. The Mechanics of Appalachian Structure. US Geological Survey, 13th 1393 Annual 1394 Report, p pt. 2, 211-281.

This manuscript was submitted to Interpretation on February, 2023.

4.2 Artigo 2 - AUTOMATIC 3D FAULT DETECTION AND CHARACTERIZATION – A COMPARISON BETWEEN SEISMIC ATTRIBUTE METHODS AND DEEP LEARNING

Oliveira, L. S. B.[1], Alaei, B.[2,3], Torabi, A. [3], Oliveira, K. M. L.[4], Vasconcelos, D. L.[5] Bezerra, F. H. R. [1], Nogueira, F. C. C. [5]

1 Laboratory of Seismology, Federal University of Rio Grande do Norte, Universitary Campus - Lagoa Nova, CEP 59078-970, Natal, Rio Grande do Norte, Brazil. lorenna_savilla@hotmail.com; hilario.bezerra@ufrn.br

2 Earth Science Analytics, Strandveien 37, 1366 Lysaker, Norway. behzad.alaei@earthanalytics.no

3 Department of Geosciences, University of Oslo, postboks 1047, Blindern 0316, Oslo, Norway. anita.torabi@geo.uio.no

4 Geophysics of Prospection and Remote Sensing Laboratory, Federal University of Ceará, Pici Campus, Bloco 1011, Fortaleza, Ceará, CEP 60440-760, Brazil. karenleopoldino@ufc.br

5 Federal University of Campina Grande, Aprígio Veloso, 882, Universitário, Campina Grande, Paraíba, CEP 58429-900, Brazil. davidgeologia2006.1@hotmail.com; cezar@uaepetro.ufcg.edu.br

Abstract

Seismic interpretation is a crucial tool for identifying faults, fluid concentrations, and flow migration pathways in the oil and gas industry. Algorithms have been developed to identify faults using seismic data and attributes such as changes in amplitude, phase, polarity, and frequency. Despite technological advancements, challenges remain in seismic interpretation due to noise, quality of data, and ault dimensions. Recently, deep learning has been applied to image faults from seismic data, which makes the process faster and more reliable. The aiming is to evaluate the performance of Deep Neural Networks (DNN) in fault interpretation by comparing the results with traditional seismic attributes in onshore seismic data. Our results indicate that the DNN results reveal more structural detail which is essential in characterizing the 3D fault geometry. In addition, DNN results show better continuity, less false positives, and less affected by the noise in the onshore seismic data used in this case. The 3D fault model from DNN identifies faults and their fault segments with greater variability of strikes, as well as revealing more minor faults. Based on the DNN fault model we characterized the 3D geometry of a new fault in the Rio do Peixe Basin, without noise influence.

Keywords: Seismic Attributes; Neural Network; Faults; Noise; 3D

4.2.1 Introduction

Seismic interpretation has been widely used to map the geometry of geologic features, such as stratigraphic surfaces and faults in sedimentary basins. This technique has become fundamental to the oil and gas industry since it helps to identify faults, fluid concentrations, and flow migration pathways (e.g., Ligtenberg, 2005; Hustoft et al., 2007). Examples are the identification of faults using seismic data to detect fluid migration, building advanced geological models and studying fault fluid flow behavior (e.g., Berndt, 2005; Hustoft et al., 2007; Kluesner and Brothers, 2016), mapping fault zones and their internal structures (e.g., Jones and Knipe, 1996; Cohen et al., 2006; Botter et al., 2014; Liao et al., 2019), measuring fault throw and displacement (e.g., Walsh and Watterson, 1987; Hale, 2013; Ma et al., 2019), and predicting fault growth (e.g., Mansfield and Cartwright, 1996; Preuss et al.,2019).

Seismic attributes are changes in the amplitude, phase, polarity, frequency, and velocity of seismic data (Dorn, 1998). As a quantitative measure of a seismic feature of interest (Chopra and Marfurt, 2005), seismic attributes have been an essential tool in seismic interpretation. Various studies have used seismic attributes with a different focus to automatically trace the fault plane geometry (Bahorich and Farmer, 1995; Chopra and Marfurt, 2005, 2007, 2010b; Brouwer and Huck, 2011; Libak et al., 2017; Qi et al., 2019), deformation surrounding fault structures based on disturbance zones (Liao et al., 2020; Iacopini et al., 2016), and fluid pathways in fault zones (Berndt, 2005; Kluesner and Brothers, 2016).

Even with the advancement in technology using seismic data to identify faults, some challenges remain, such as the resolution, noise, quality of the seismic data, and fault dimensions. In this regard, several studies have developed tools to remove or suppress noise in seismic data and attenuate this effect with different types of processing (Stehly et al., 2006; Chopra and Marfurt, 2007; Iacopini et al., 2011; Yuan and Wang, 2013; Anvari et al., 2017; Birnie et al., 2021). Applying seismic attributes for automatic recognition of the fault can create artifacts (Chopra and Marfurt, 2007) or structural leakage (Iacopini et al., 2016). These challenges in seismic interpretation using attributes make the characterization of the fault geometry more complex. Some geometric parameters of the faults, such as length, matter for reservoir analysis since the fault permeability affects the fluid flow in such reservoirs (Lohr et al., 2008; Xu and Sun, 2014).

Among different seismic attributes, those that highlight the discontinuities between the seismic reflectors or geological horizons are the best ones to image faults. Coherence is one of these attributes that reveals structural features and measures the similarity between neighboring seismic traces (Bahorich and Farmer, 1995; Marfurt et al., 1998, 1999; Gersztenkorn and Marfurt, 1999). Seismic attributes such as coherence are sensitive to discontinuities, making this quantity unique and suitable for imaging structures such as faults (Libak et al., 2017). Coherence attributes alone may image other geological features than faults (e.g. channel edges) or artifacts and therefore need to be geologically sense checked. To further enhance the quality of fault images on coherence

attributes and highlight smaller faults with more detail of fault geometry, some studies combined frequency decomposition with coherence calculation (Alaei, 2012; Li and Lu, 2014; Botter et al., 2016; Alaei and Torabi, 2017; Mahadik and Routray, 2022).

Recently, supervised deep learning has been utilized to image and interpret faults from seismic data, making the process of seismic interpretation faster and more reliable (Wu et al., 2019, 2020; Torabi and Alaei, 2022). Since the publication of AlexNet by Krizhevsky et al. (2012), the application of deep learning has spread in many disciplines, including geosciences. Deep learning can be used for classification, object detection, and semantic segmentation. Deep learning includes large networks of functions and parameters in architectures containing interconnected neurons in layers (Goodfellow et al., 2016). In supervised deep learning, it is possible to provide the computer with seismic data as input (feature) and instruct the data by adding some interpretation as output (label) examples. In this way, different deep-learning networks can be used to identify and interpret salt bodies and faults (Di et al., 2018; Wu and Zhang, 2018) and fault zones (Wu et al., 2019; Wrona et al., 2020; An et al., 2021). Recent studies compared approaches such as Deep Neural Networks (DNN) and seismic attributes to predict faults, showing the challenge of identifying fault geometry and the sensitivity to the seismic noise or facies (Qi et al., 2019; Lorentzen et al., 2022; Lubo-Robles et al., 2022). However, the number of studies comparing (DNN) and conventional interpretation of seismic data is limited, and more study cases are needed.

In this study, we (a) compare seismic interpretations of faults utilizing seismic attributes with the results from deep learning, (b) map and characterize faults using the best automatic seismic tools to recognize their 3D geometry, (c) add the new mapped faults in the structural framework of the basin, and (d) highlight the advantages and disadvantages of each approach used in the seismic interpretation. Here, we present a comparison of results from seismic interpretation using seismic attributes and supervised deep learning applied to onshore 3D seismic data from the Rio do Peixe Basin (RPB), Brazil. We applied seismic attributes such as variance, ant tracking, similarity, and fault enhancement. The pretrained DNN model we used is trained using TransUnet (Chen et al., 2021) networks, customized to predict faults in seismic data. The comparisons we made between attributes and deep learning reveals, in our case, that deep learning is more successful in identifying faults and their geometry than results from seismic attributes. The differences are better continuity of the fault segments, variability of strikes, and detection of a greater quantity of minor faults. In addition, our study highlights that the seismic noise influences the quality of seismic attributes (and therefore imaged faults) more than fault prediction from deep learning.

4.2.2 Geological Setting

Our study area was located in the Rio do Peixe Basin (RPB), an intracontinental basin in northeastern Brazil. This basin inherited the geometry of NE-SW- and E-W-striking Precrambian shear zones, which were reactivated as faults in the Cretaceous. The main faults are the NE-SW-striking Portalegre and the E-W-striking Patos (Sénant and Popoff, 1991; Françolin et al., 1994; Nicchio et al., 2022; Ramos et al., 2022) (Fig. 1). These major rift faults control the depocenters in the RPB.

Nogueira et al. (2015) and Vasconcelos et al. (2021) identified two major tectonic phases, synrift and postrift. The first was responsible for the generation of the basin during the extensional phase that created E-W- and NE-SW-oriented faults. The second was a tectonic inversion associated with ENE-WNW late to post Cretaceous compression. More recently, Nicchio et al. (2022) used paleomagnetic data and concluded that two stretching directions gradually shifted from NNE-SSW to NW-SE during basin development in the Early Cretaceous as a consequence of clockwise rotation in South America.

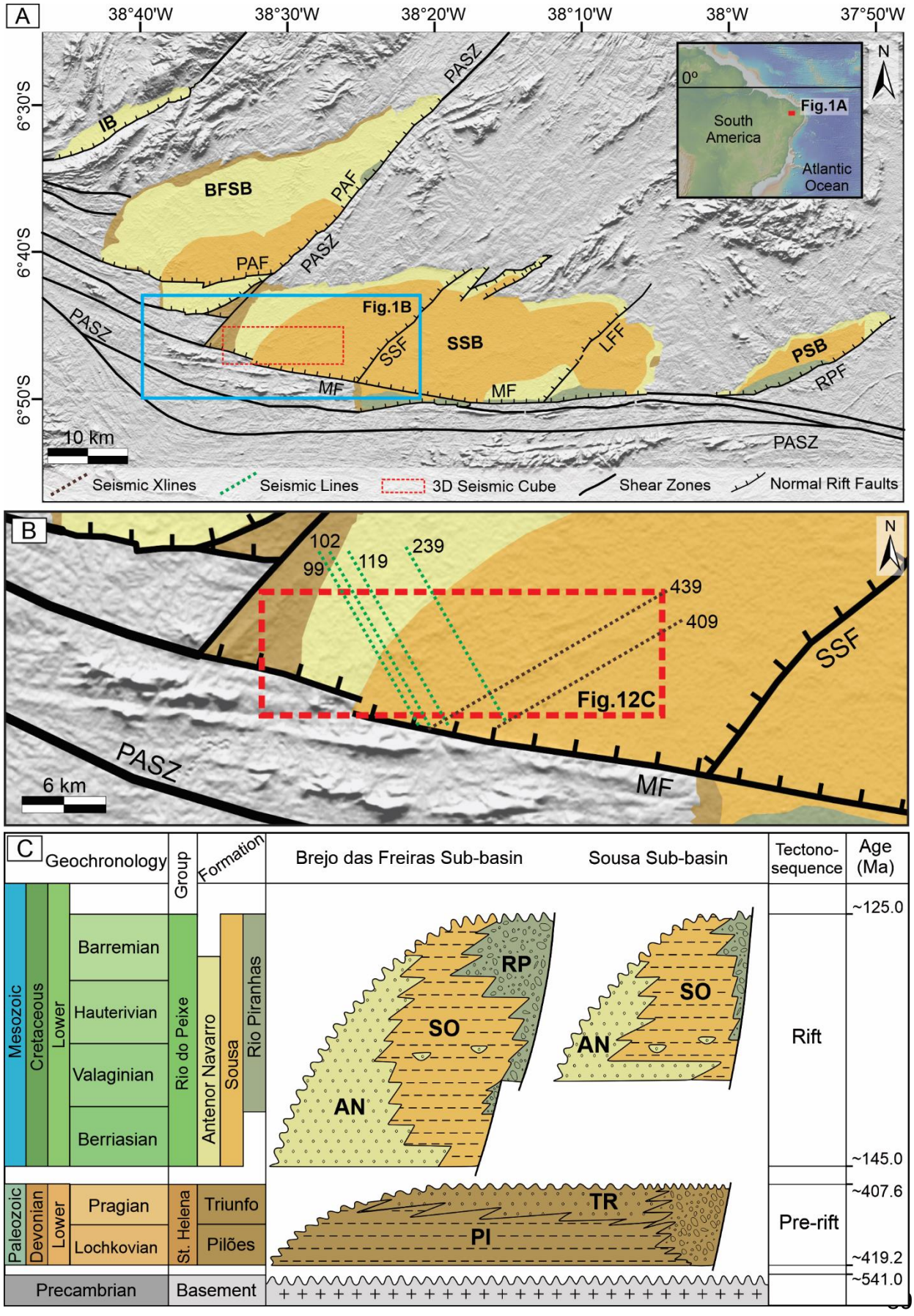
A
38°40'W
38°30'W
38°20'W
38°10'W
38°W
37°50'W
6°30'S
6°40'S
6°50'S
IB
BFSB
PAF
PASZ
Fig.1B
SSF
SSB
LFF
PSB
RPF
MF
10 km
Seismic Xlines
Seismic Lines
3D Seismic Cube
Shear Zones
Normal Rift Faults
0º
Fig.1A
South America
Atlantic Ocean
N
B
102
99
119
239
439
409
Fig.12C
6 km
C
Geochronology
Group
Formation
Brejo das Freiras Sub-basin
Sousa Sub-basin
Tectono-sequence
Age (Ma)
Mesozoic
Cretaceous
Lower
Barremian
Hauterivian
Valaginian
Berriasian
Rio do Peixe
Antenor Navarro
Sousa
Rio Piranhas
RP
SO
AN
Rift
~125.0
~145.0
Paleozoic
Devonian
Lower
Pragian
Lochkovian
St. Helena
Triunfo
Pilões
TR
PI
Pre-rift
~407.6
~419.2
~541.0
Precambrian
Basement

Figure 1 – (A) Geological map of the RPB (adapted from Françolin et al., 1994; Medeiros et al., 2005; Vasconcelos et al., 2021; Ramos et al., 2022) (B) Location of the 3D seismic survey (dashed red rectangle). (C) Stratigraphic chart of RPB (modified from Rapozo et al., 2022; Ramos et al., 2022). Basin and subbasins: IB, Icozinho; BFSB, Brejo das Freiras; SSB, Sousa; PSB, Pombal. Shear zones: PASZ, Portalegre; PSZ, Patos. SSF. Faults: Sítio Sagui; MF, Malta; PAF, Portalegre; LFF, Lagoa do Forno; RPF, Rio Piranhas.

The RPB comprises the Brejo das Freiras, Sousa, and Pombal subbasins and has the following stratigraphic units: two Devonian units (Pilões and Triunfo Formations) and three Early Cretaceous units (Antenor Navarro, Sousa, Rio piranhas Formations) from bottom to top (Córboda et al., 2008; Françolin et al.,1994; Sénant and Popoff, 1991; Silva et al., 2014). The Pilões Formation predominantly consists of siltstones and shales related to deltaic to fluvial systems, overlaid by the Triunfo Formation, mainly composed of fluvial-deltaic gray-to-white sandstones and conglomerates. The Antenor Navarro Formation is composed of fluvial fine to conglomeratic sandstones and conglomerates. It is overlain by the Sousa Formation, which is composed of lacustrine intercalations of shales and siltstones. The Rio Piranhas Formation occurs at the top of the stratigraphic column and is predominantly composed of alluvial fan conglomerates.

The RPB exhibits good exposures of faults, fractures, and deformation bands, which have been the target of several studies (e.g., Nicchio et al., 2018; Vasconcelos et al., 2021; Souza et al., 2021; Lourenço et al., 2021). These subsidiary fault structures deformed the host rock and changed its petrophysical properties (e.g., Araujo et al., 2018; Pontes et al., 2019; Nogueira et al., 2021; Oliveira et al., 2022; Silva et al., 2022). In addition, several studies revealed the variation in damage zone width and the arrangement of the structures as clusters, singles, and anastomosed patterns influencing the fluid flow behavior of faults (Torabi et al., 2021; Lourenço et al., 2021; Oliveira et al., 2022; Silva et al., 2022). Furthermore, different fault zone configurations in the basin such as flower structures were reported at a subseismic scale (Nogueira et al., 2015).

4.2.3 Data and Methods

We used seismic reflection data to characterize the structural framework in the seismic survey area, which was provided by the Brazilian Agency of Petroleum, Natural Gas, and Biofuels (ANP). The 3D seismic reflection dataset is displayed with reverse polarity, following the SEG convention. The seismic survey extends down to 2000 ms (TWT). The seismic data are time migrated and have a dominant frequency of approximately 30 Hz and an interval velocity of approximately 3,200 m/s, which indicates a vertical resolution of approximately 26 m. In the seismic sections, the horizons are continuous from 150 ms to 930 ms, facilitating the identification of faults. The relatively continuous reflectivity is observed from 150 to 930 ms, whereas data is noisy from 0 to 150 ms and close to the basement.

4.2.3.1 Conventional seismic interpretation and attributes

We used conventional seismic data interpretation techniques, such as the detection of abrupt terminations of reflections and dip changes due to faulting and 3D seismic attributes, to identify the faults in the southeastern part of the Rio do Peixe Basin. The seismic inlines trend NE-SW, whereas the cross lines are aligned along NW-SE. In addition, the seismic horizons strike NE-SW. The coincidence between faults and seismic horizons along the NE-SW trend makes it difficult to identify the former. We used a structurally constrained approach based on the local dip and azimuth calculation of the 3D seismic data to derive seismic attributes. We generated the following attributes to enhance the identification of faults: (i) Semblance-based similarity attribute, (ii) variance, (iii) ant tracking, and (iv) eigen structure-based fault enhancement

The coherence attributes have been widely used in seismic interpretation to highlight faults and stratigraphic features since the 1990s (Bahorich and Farmer 1995). The coherence attribute measures the similarity of the seismic waveform between neighboring traces using coherence coefficient estimation (Alaei, 2015; Chopra and Marfurt, 2007). This methodology was applied to detect discontinuities in seismic horizons and characterize structures (Bahorich and Farmer, 1995; Chopra, 2002; Dutzer et al., 2010; Iacopini et al., 2011,2016; Qi et al. 2017; Libak et al., 2017; Ma et al., 2019). For example, highly coherent seismic waveforms indicate laterally continuous lithologies, while abrupt changes in the waveform can indicate faults and fractures in sedimentary rocks. We generated semblance-based similarity attributes in this study using Attribute-Assisted Seismic Processing & Interpretation software. Widely applied in previous studies, the semblance is understood as the ratio between the analysis window and the average energy of all trace samples along the dip of the reflector within the energy of the average trace (Marfurt et al., 1998; Chopra and Marfurt, 2007; Libak et al., 2017).

The second coherence attribute we generated is variance, another measure of waveform discontinuity and lateral changes in seismic amplitude (Chopra and Marfurt, 2007). These lateral changes are represented as traces over a sample interval, which is calculated in 3D. Therefore, similar traces produce low variance values, while discontinuities (faults, fractures, channel edges) have high variance values. As variance is considered a reverse version of semblance, this seismic attribute is commonly used to highlight seismic breaks in previous studies (Iacopini et al., 2012; Liao et al., 2019, 2020; Phillips et al., 2019). We applied this attribute, focusing on revealing the fault traces.

Following the generation of two coherence attributes, we applied a fault enhancement process using the ant tracking approach (Randen et al., 2001). Ant tracking is based on the principles of swarm intelligence that connect and skeletonize the discrete discontinuities generated by the coherence family of attributes. The variance attribute provides the seed points we generated in the previous stage for ant tracking. The variance attribute was generated using the following filter sizes: Inline and cross line range: 3; and vertical sample size: 15. Dip information was not used in the variance calculation. In order

to map faults in seismic data, we applied ant tracking to highlight these structures as many authors have previously noted (Jansen, 2005; Basir et al., 2013; Liao et al., 2020).

The last attribute we generated aimed to enhance fault traces; where coherence is used as input. The enhancement was achieved by applying Eigen structure analysis to compare the dip and azimuth of linear discontinuities from a volumetric perspective. After the eigenvector application, the directional LoG filter was applied to the workflow, followed by the skeletonization techniques proposed by Machado et al. (2016) and Qi et al. (2019b). The input to the fault enhancement process was the similarity attribute.

4.2.3.2 Fault interpretation with DNN

The interpretation of faults using DNNs in general and CNNs, in particular has received much attention in the last five years (e.g., Wu et al., 2019, 2020; Yang et al., 2021; Liu et al., 2020; Torabi and Alaei, 2022). The fundamental concept of using DNNs is to train DNN models that classify seismic data into two classes: faults and background or host rock. By providing examples of faults (fault sticks) on seismic slices, DNN networks learn to perform semantic segmentation and assign one class (either fault or background) to each seismic data point in the seismic survey data. This is a supervised approach, and the quality of imaged or predicted faults by the DNN network depends to a large degree on the quality and amount of provided fault sticks or labels for training. The labeling or fault-picking step to provide the training examples for the DNN networks is the most time-consuming part of imaging faults using machine learning approaches. This time-consuming step has been significantly reduced by replacing manual fault picking with fault picks predicted by DNN models that are already trained on either real or synthetic seismic data with corresponding faults. In this study, Earth Science Analytics provided a pretrained model from EarthNet (Oikonomou et al., 2019) to predict faults in our survey area. The model trained on more than 40 seismic surveys represents different geological settings. No seismic data from Brazil were used in the model training. The DNN architecture used in the pretrained fault interpretation model is the TransUnet network (Chen et al., 2021), which has been customized to train for fault interpretation. The architecture of the model consists of 4 layers, a 320 by 320 pixels patch size, 4 number of transformers, and two types of loss functions (Jacard loss and categorical cross entropy). We have applied this model to the survey area in this research along the inline and cross-line directions. The fault probability volume used later in the result section was generated by taking the average fault volume along the inline and cross-line directions. The ideal workflow is to refine the model by training on fault sticks from our studied area. Since we have only applied a pre trained model to generate fault probability volume and have not done any further refinement of the model (no manual work), comparing faults derived from fault attributes is relevant. The averaged 3D fault probability volume (taken from inline and cross line directions) was then used as input to carry out fault characterization. The main purpose of using ML-derived fault volumes is to identify the faults and structural framework of the basin, show their geometry and small segments and compare them with faults derived from ant tracking.

4.2.4 Results

The results of this study are presented in four parts. First, we present the applied seismic attributes, which reveal some of the fault trends. Second, the fault model from DNN shows a 3D perspective of the detected faults with different orientations and sizes. Therefore, we present a comparison between the DNN and seismic attribute results. Then, we characterize as an example, a dextral fault with a normal component and its 3D geometry based on the 3D fault model from DNN.

4.2.4.1 Fault interpretation results from seismic attributes

Four different seismic attributes are presented in this section. Figure 2 shows the results of all four attributes at 280 ms. The two coherence attributes (similarity in Fig. 2b and variance in Fig. 2c) show some faults with mainly NW-SE trends. The continuity of the imaged fault on the similarity attribute is slightly better than the variance. The results from two fault enhancement approaches (in fault enhancement Figure 2d and ant tracking in Figure 2e) revealed a few more faults than the similarity and variance attributes (Fig. 2b and c). Faults detected strike E-W, NW-SE, NE-SW, and N-S, with respect to the longest fault segment length and the largest distribution in the seismic cube. Figure 3 shows the same attributes shown in Figure 2 for a deeper time slice (420 ms). At 420 ms, the similarity (Fig. 3b) and variance attributes (Fig. 3c) show almost the same faults, but the similarity attribute has more noise or false-positives in the western part of the survey. Ant-tracking (Fig. 3e) and fault enhancement (Fig. 3d) display more faults than their input volume (variance and similarity attributes). The NNW-SSE faults imaged on the eastern part of the survey area in the ant tracking results (Fig. 3e) are almost absent in the fault enhancement results (Fig. 3d).

In general, seismic attributes showed the majority of E-W-oriented faults with continuous traces, displayed in the entire seismic cube from the basement to the surface (Figs. 2 and 3). In some areas, the E-W-striking faults can have a strike variation to WNW-ESE. The NW-SE-striking faults form the second most common set, being the second most continuous trace of faults, and appear in greater quantity near the surface in the seismic volume (Figs. 2 and 3).

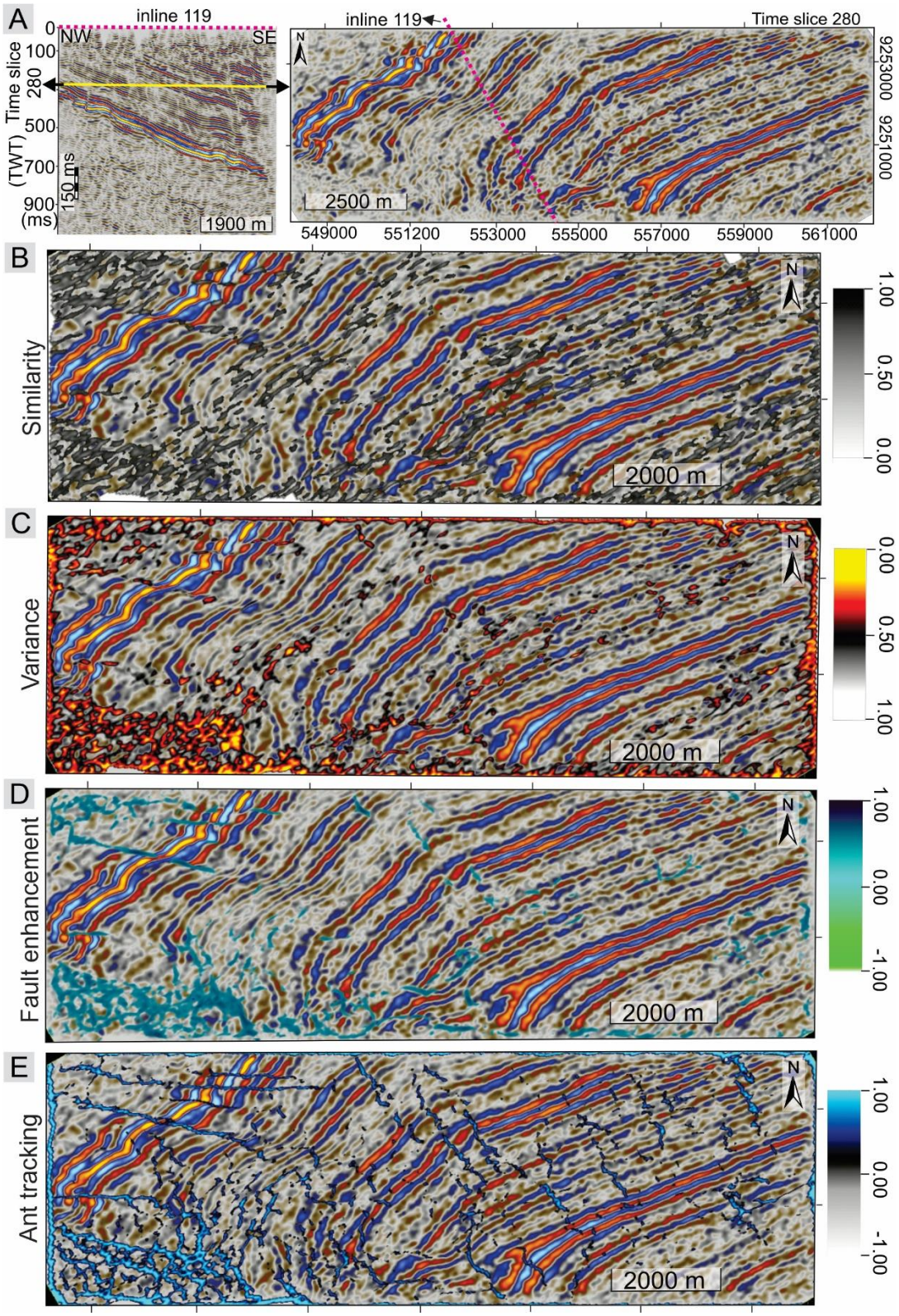

Figure 2 – (A) Time slice (280 ms) together with (B) similarity, (C) variance, (D) fault enhancement, (E) ant tracking, revealing the faults, highlighted for the most positive values in color tables (using 60 Hz frequency as input).

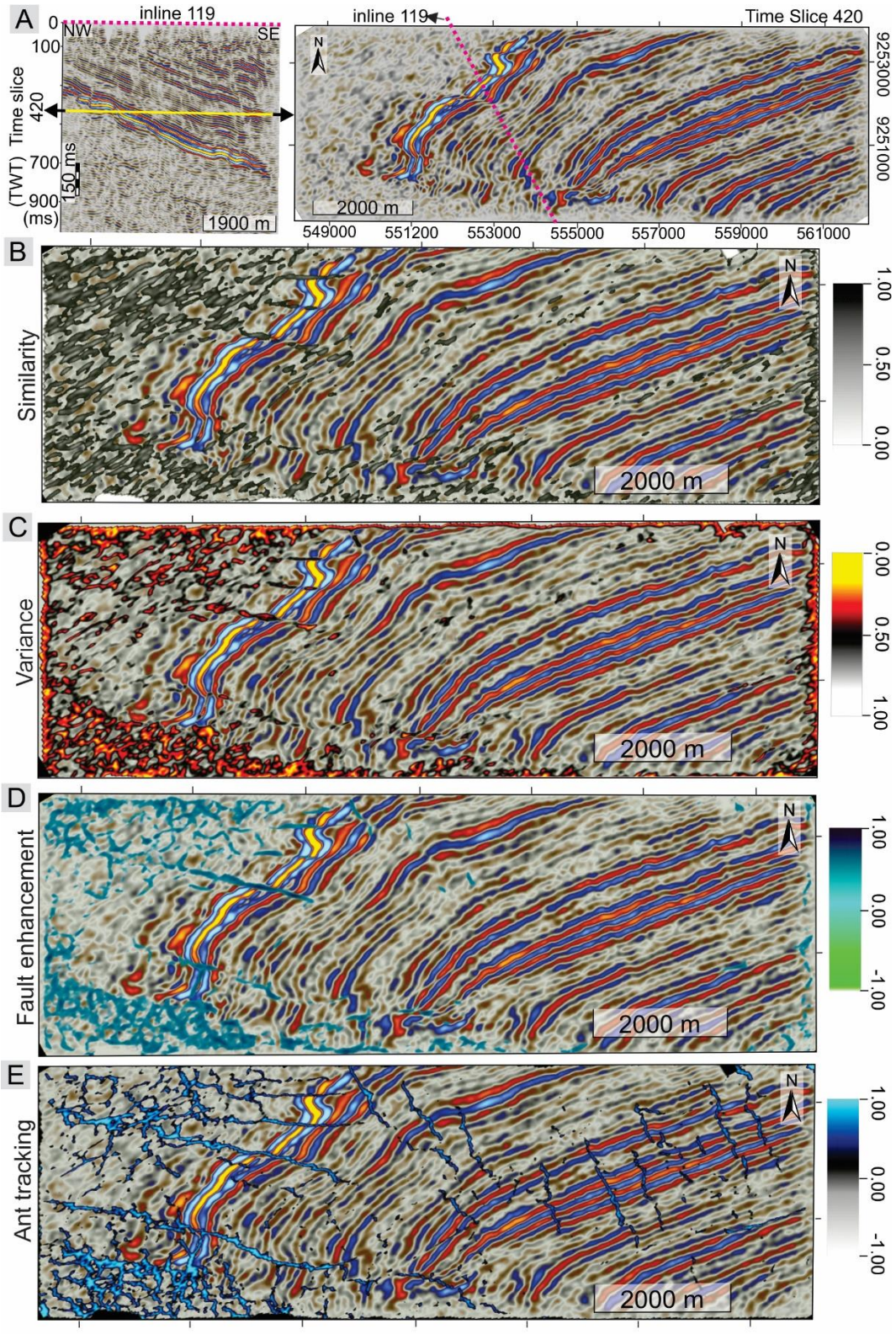

Figure 3 – (A) Time slice (420 ms) together with (B) similarity, (C) variance, (D) fault enhancement (E) ant tracking, revealing the fault traces, featured in the most positive values in the color tables.

It is more difficult to use the results from the seismic attributes for fault analysis from a 3D perspective since all of them are significantly influenced by noise. The possible fault discontinuities are mixed with the noisy data in superficial or deeper areas in the basin close to the basement.

4.2.4.2 Fault interpretation results from DNN

The fault interpretation results from the DNN are illustrated in Figure 4. The results are the average of the applied model in the inline and cross-line directions. A review of the results shows that the quality of the predicted faults is less affected by the near-surface noise in the shallow section and the scattered signal near the basement. The results from the two time slices show continuous and long fault segments along the E-W and NW-SE directions, which are concentrated in the western and eastern parts of the seismic cube, respectively (Fig. 4). The fault traces cut across the entire basin from the Lower Devonian to the Upper Cretaceous sedimentary package. The small fault segments (strike NE-SW) are concentrated close to the surface, located in the Cretaceous sedimentary package.

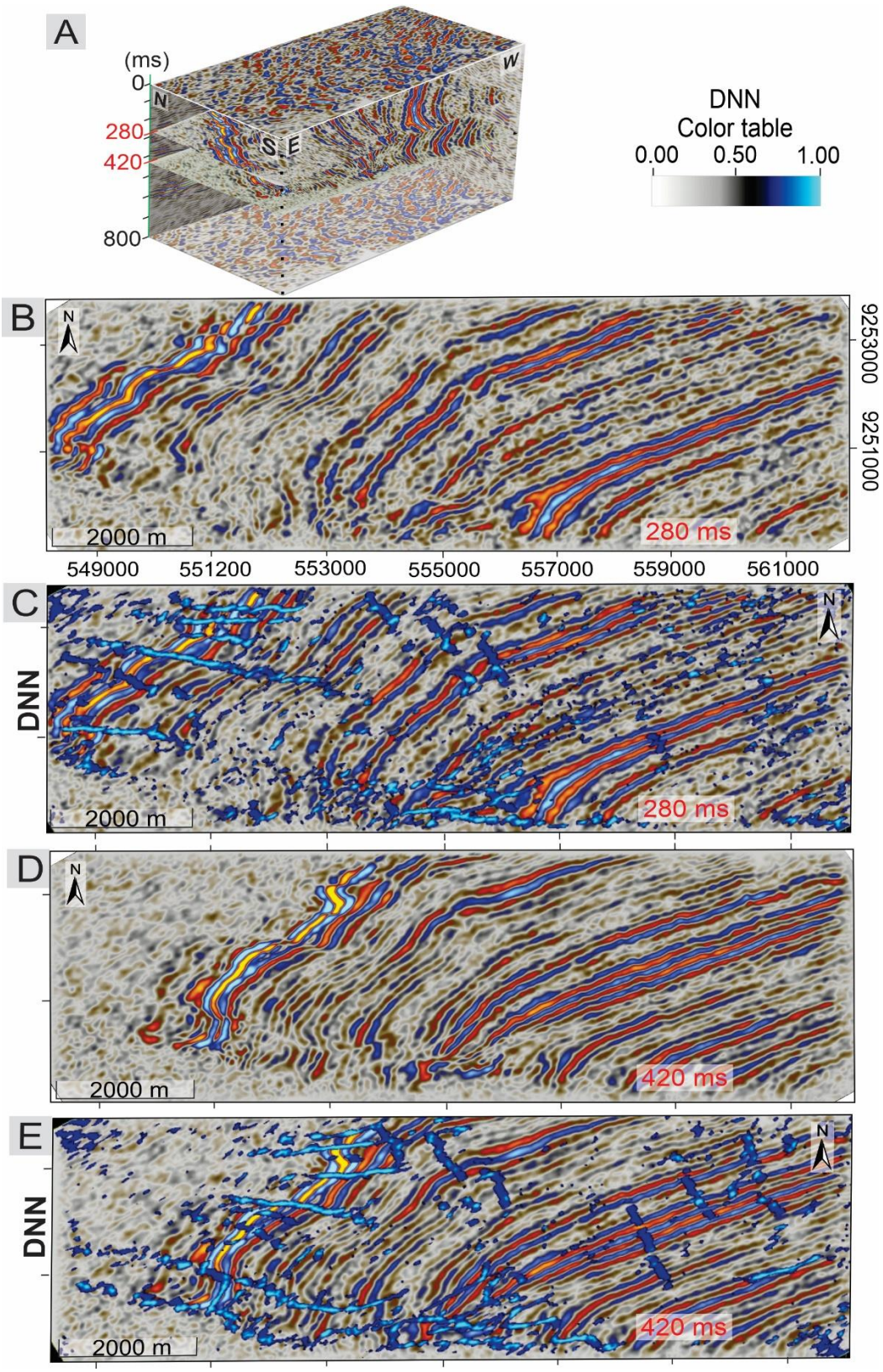

Figure 4 - (A) Seismic data showing time slices (B) 280 and (D) 420 ms, and (C) and (E from the DNN model.

Visualizing faults derived from the DNN approach with seismic data in the horizontal and vertical directions reveals the faults from a 3D perspective (Fig. 5). The faults with the longest segments mostly have a vertical to subvertical dip, while small subsidiary faults are dipping less than (Fig. 5).

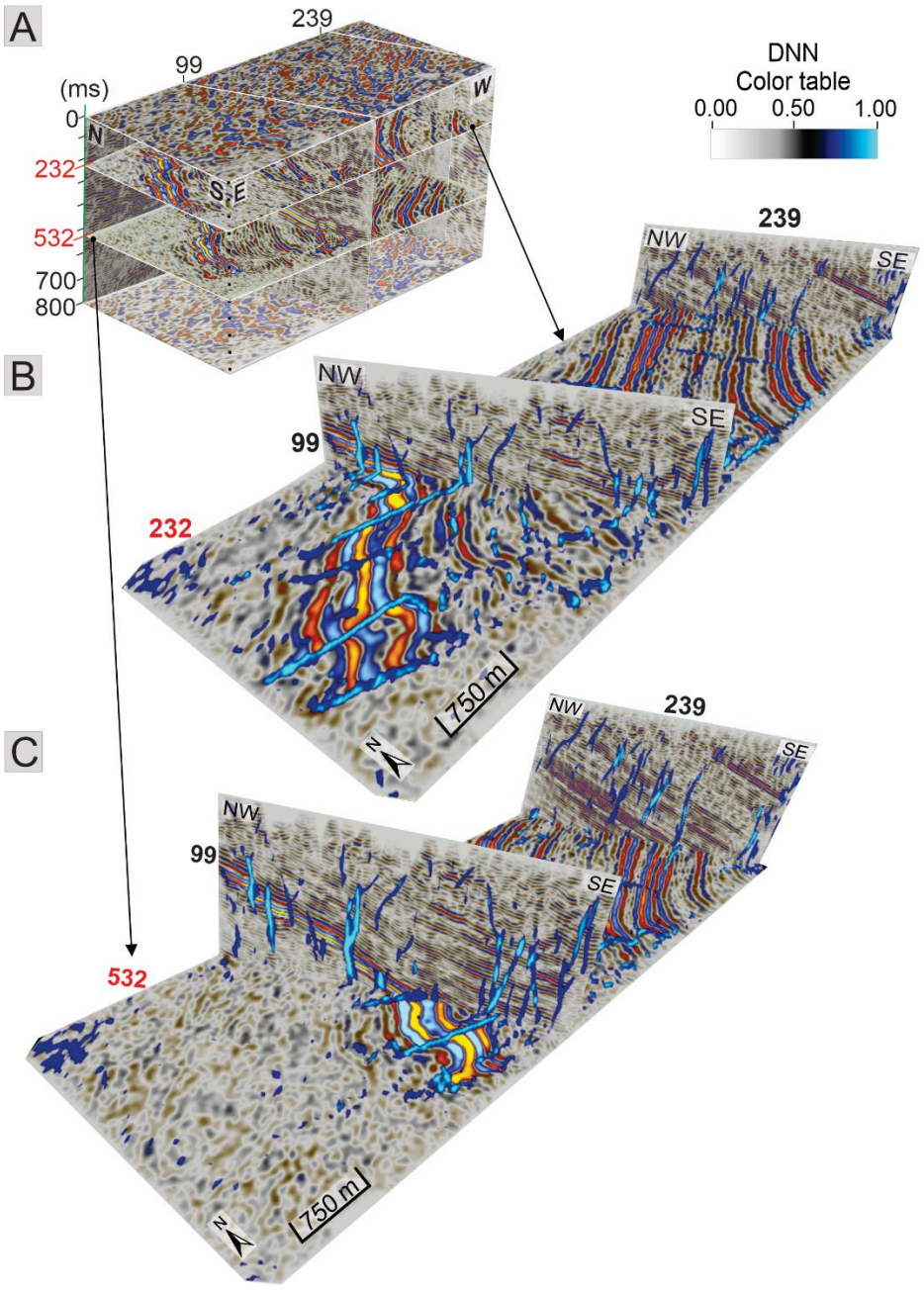

Figure 5 – (A) Seismic cube showing time slice, (B) time slice 232 ms and with inlines (99 and 239, (C) time slice 532 ms combined with inlines (99 and 239) together with results from the DNN model revealing the faults geometry in 3D structures' faults and the 3D geometry.

4.2.4.3 Comparison of seismic attributes with DNN results

Several seismic attribute volumes are presented in the results section. The most continuous and detailed results were obtained using the ant tracking volume generated with the variance attribute as input. We used ant tracking results and compared different directions in space with imaged faults derived from the DNN approach (Fig. 6).

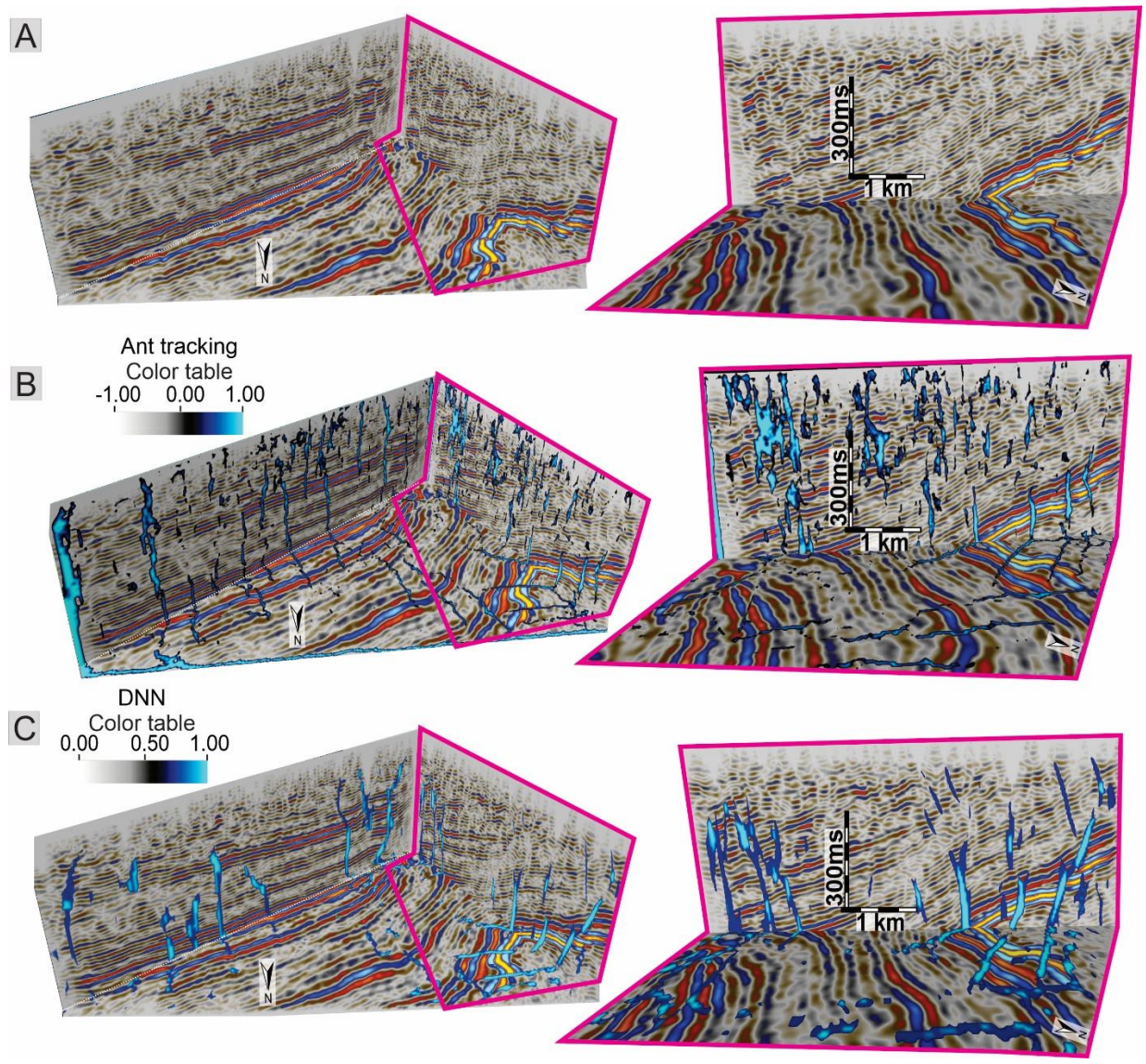

Figure 6 – Comparison between application of seismic attributes and DNN: (A) location of the time slice (420 ms) combined with inline and cross line (102 and 349, respectively); (B) Seismic data visualization with positive ant tracking; (C) Fault model from DNN revealing the fault traces combined with seismic data. The right columns in (A), (B), and (C) represent details of the left column.

We observe that the DNN fault volume allowed us to identify the geometry of faults better than faults detected by the seismic attributes since it displays different sizes of the fault segments in a greater variety of orientations. These results are meaningful

when compared to the geological setting and exposed faults in the study area (Figs. 6 and 7). The continuity of the imaged faults using the DNN method is better in both the horizontal and vertical directions (Fig. 7). The improved images of faults from the DNN method make it easier to interpret fault geometries such as conjugate pairs of faults or flower structures (Fig.7). In addition, the ant tracking results have more false positives than the DNN results (Figs. 6 and 7).

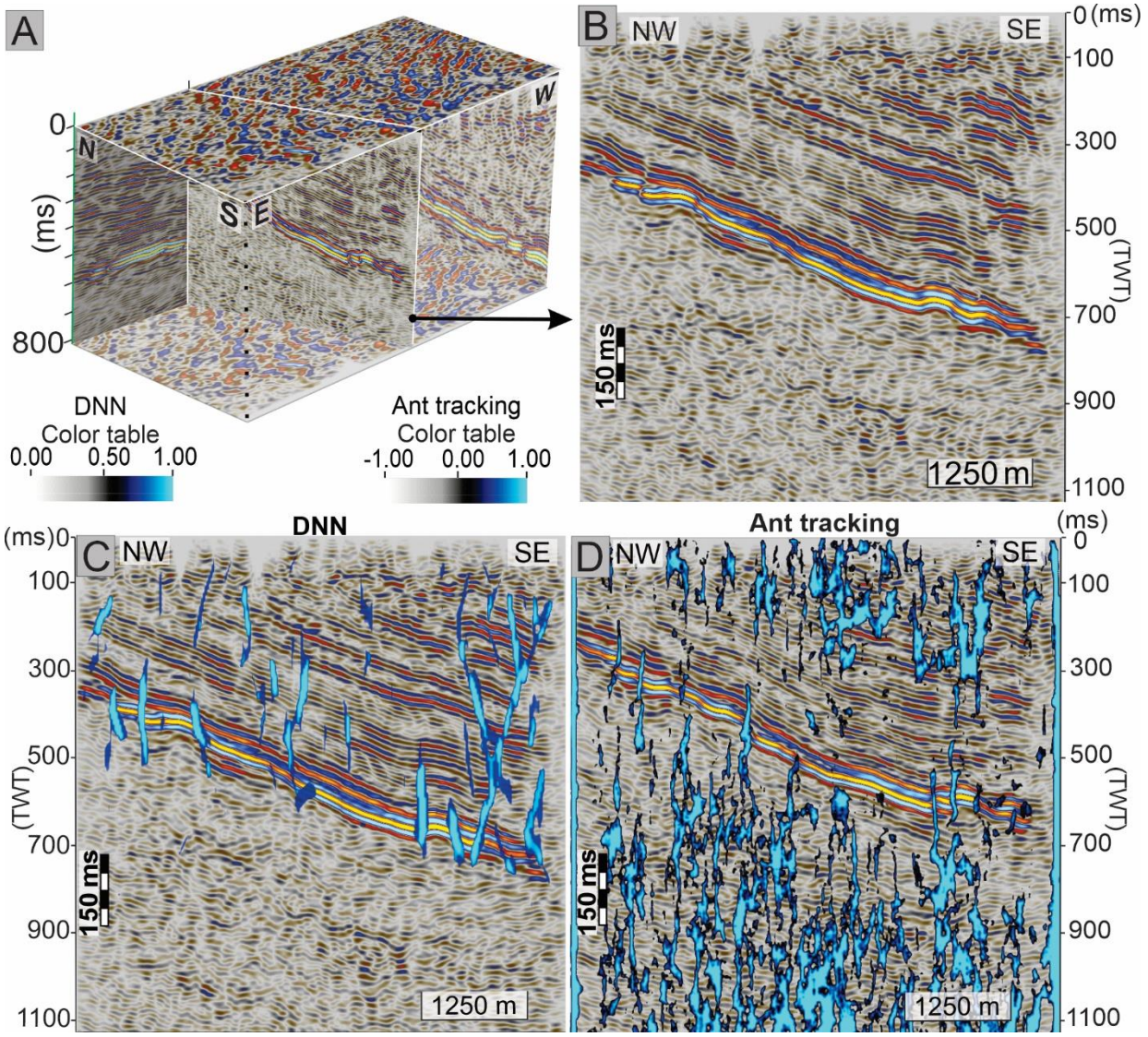

Figure 7 – Comparison between DNN and Ant tracking fault traces applied on (A) seismic cube; (B) Example of a seismic profile to show the comparison between (C), 3D fault model from DNN, and (D), the ant tracking seismic attribute. The most positive answer shows the ant tracking discontinuities marked in the color table.

Unlike the ant tracking results, the DNN results are less influenced by the noisy near-surface areas or in the deepest section closer to the basement (Fig. 8). Traces of imaged faults in the ant tracking data are mixed with noise, causing a misinterpretation

(not complete correct fault geometry) of the discontinuities in the seismic data. It is, therefore, difficult to use fault images from ant tracking for kinematic analyses and further characterization of faults in the study area. However, the DNN results only reveals the discontinuities in the seismic data as faults, not connecting these imaged fault segments to the noisy areas.

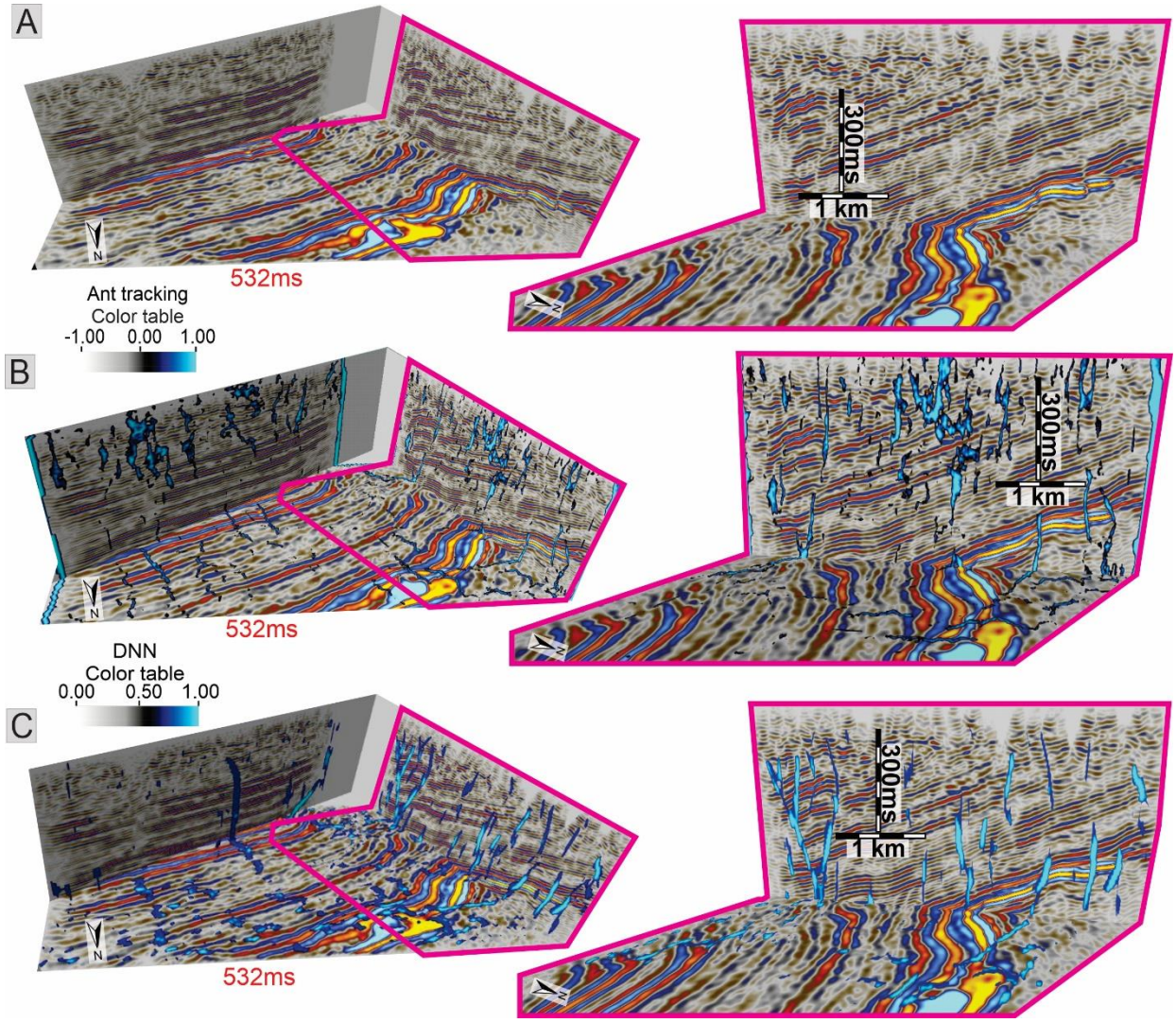

Figure 8 – Comparison between results of seismic attributes and DNN and (A) location of the time slice (532 ms) combined to inline and cross line (109 and 409, respectively). (B) Seismic data visualization with positive ant tracking. (C) Fault results from DNN model revealing the fault traces displayed with seismic data. The right columns in (A), (B), and (C) represent zoomed in of the left column.

4.2.4.4 3D Fault characterization using DNN results

We used the fault volume from the DNN approach (Figs. 6 and 7) and selected one of the faults to carrying out a further geometric characterization of the fault geometry in 3D. The selected fault is shown in Fig. 9. Using vertical and horizontal slices of seismic and fault volumes from the DNN approach at different depths, we derived the 3D geometry of the selected fault and its segments. The geometric characterization showed that the fault traces most likely represent patterns of a negative flower structure (Fig. 9). The results clearly indicate that the selected fault extends from the basement and throughout the entire basin to the surface from the Devonian to the Cretaceous sedimentary package.

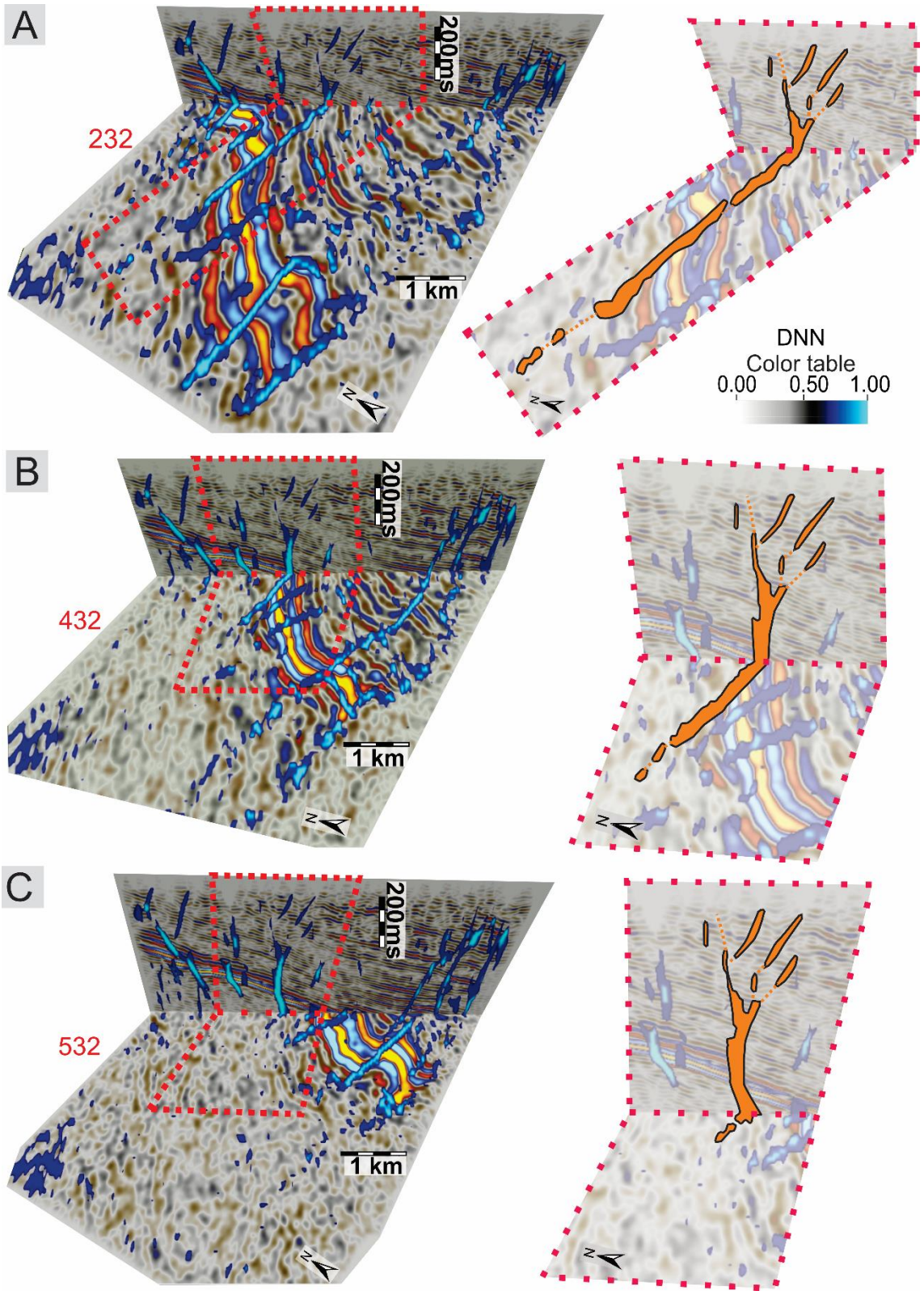

Figure 9 - Example of detected fault using the DNN results (A) in time slice (232 ms) combined with inline (102) exhibiting a flower structure geometry near the surface; (B)

time slice (232 ms) with inline (102) ing the E–W-striking fault; (C) time slice (532 ms) combined with inline (102) and the detected fault.

We interpreted the fault kinematics by analyzing the time slices and seismic lines passing through this fault. Combining the reflective patterns on both sides of the fault, we interpreted an oblique movement along the fault plane with a dextral horizontal component and a normal vertical component (Fig. 10). We observed that the antithetic subsidiary fault segments, which are part of the negative flower structure, were easier to identify than the synthetic subsidiary fault segments in the volume derived from the DNN approach.

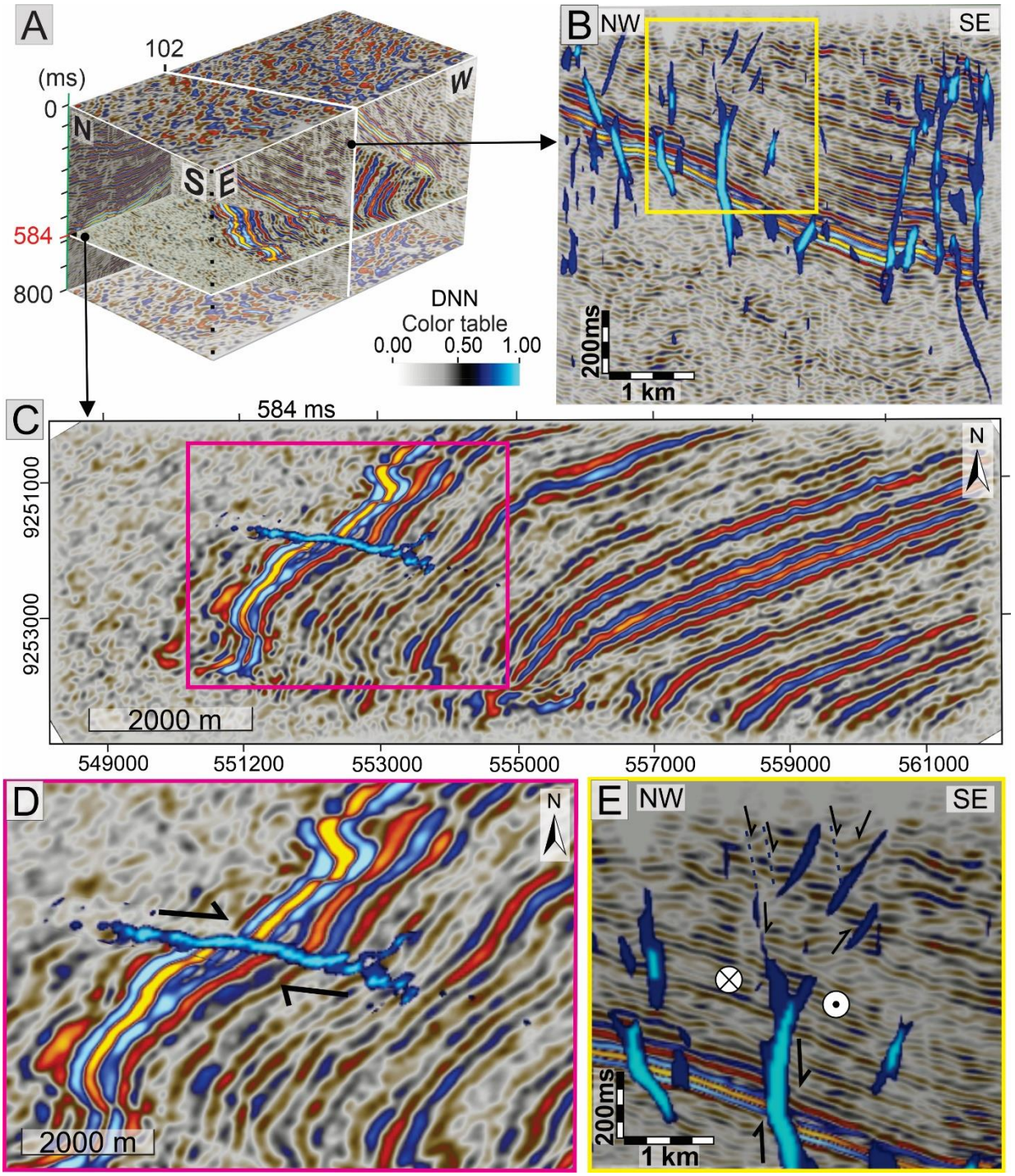

Figure 10 – A kinematic analysis of the fault revealed by the DNN: (A) 3D perspective of the structure; (B) a seismic profile (102); (C) a time slice (532 ms) with fault trace; (D) zoom of (C) on map view shows the dextral fault; (E) zoom of (B) the same detected fault with a normal vertical movement, geometry of the negative flower structure and its segments.

In order to characterize the fault from a 3D perspective, we used the 3D fault results from DNN approach and the seismic profiles to interpret the fault connecting to its segments and the minor subsidiary faults (Figure 11A). Analyzing the fault detected by the model in the inlines, we observe the fault is lengthening from the westernmost portion to the central region of the seismic cube, crosscutting all the sedimentary packages of the basin (Figs. 11B and 12A).

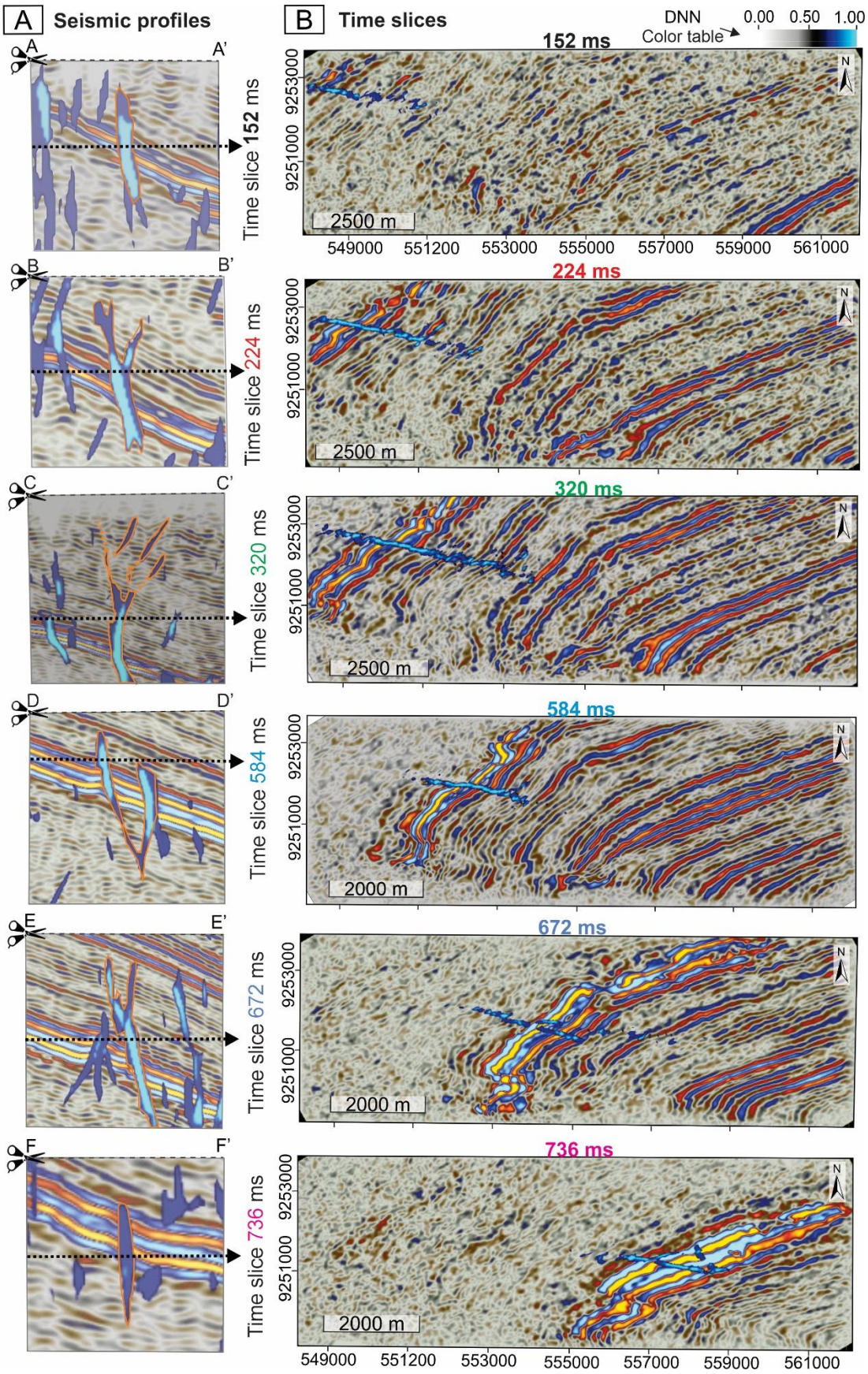
A Seismic profiles
B Time slices
DNN
Color table
0.00 0.50 1.00
A
A'
Time slice 152 ms
152 ms
B
B'
Time slice 224 ms
224 ms
C
C'
Time slice 320 ms
320 ms
D
D'
Time slice 584 ms
584 ms
E
E'
Time slice 672 ms
672 ms
F
F'
Time slice 736 ms
736 ms
N
2500 m
2000 m
9251000
9253000
549000
551200
553000
555000
557000
559000
561000

Figure 11 –The figure shows a combination of the 3D fault model from DNN and the seismic data: (A) fault traces on seismic profiles are part of the same fault (A-A' and F-F' seismic profiles); the fault splays between these segments as conjugate pairs (B-B', D-D' and E–E' seismic profiles). A negative flower structure was detected at the center of the fault (C-C'). (B) Map view of the fault at different depths. The locations of the seismic profiles are indicated in Fig. 12B.

The fault has two segments with two main strikes: E-W and WNW-ESE. These fault segments are interrupted in some portions and follow another fault segment in depth, showing parallel growth as en echelon termination (Figs. 11B and 12B). A fault trace in the time slices shows the segments in the map view migrating from the east to the west portion of the seismic cube, alternating the orientation of the fault from pure E-W to WNW-ESE (Fig. 12). The largest fault length is located in the west-central area of the seismic cube, where it presents the geometry of a negative flower (Fig. 11A). The fault is basement rooted, where its segments initiated and crosscut the entire basin. We connected the fault segments to fully interpret it, starting from 100 ms and going as far as 930 ms, where the basin reflectors disappear (Fig. 12A).

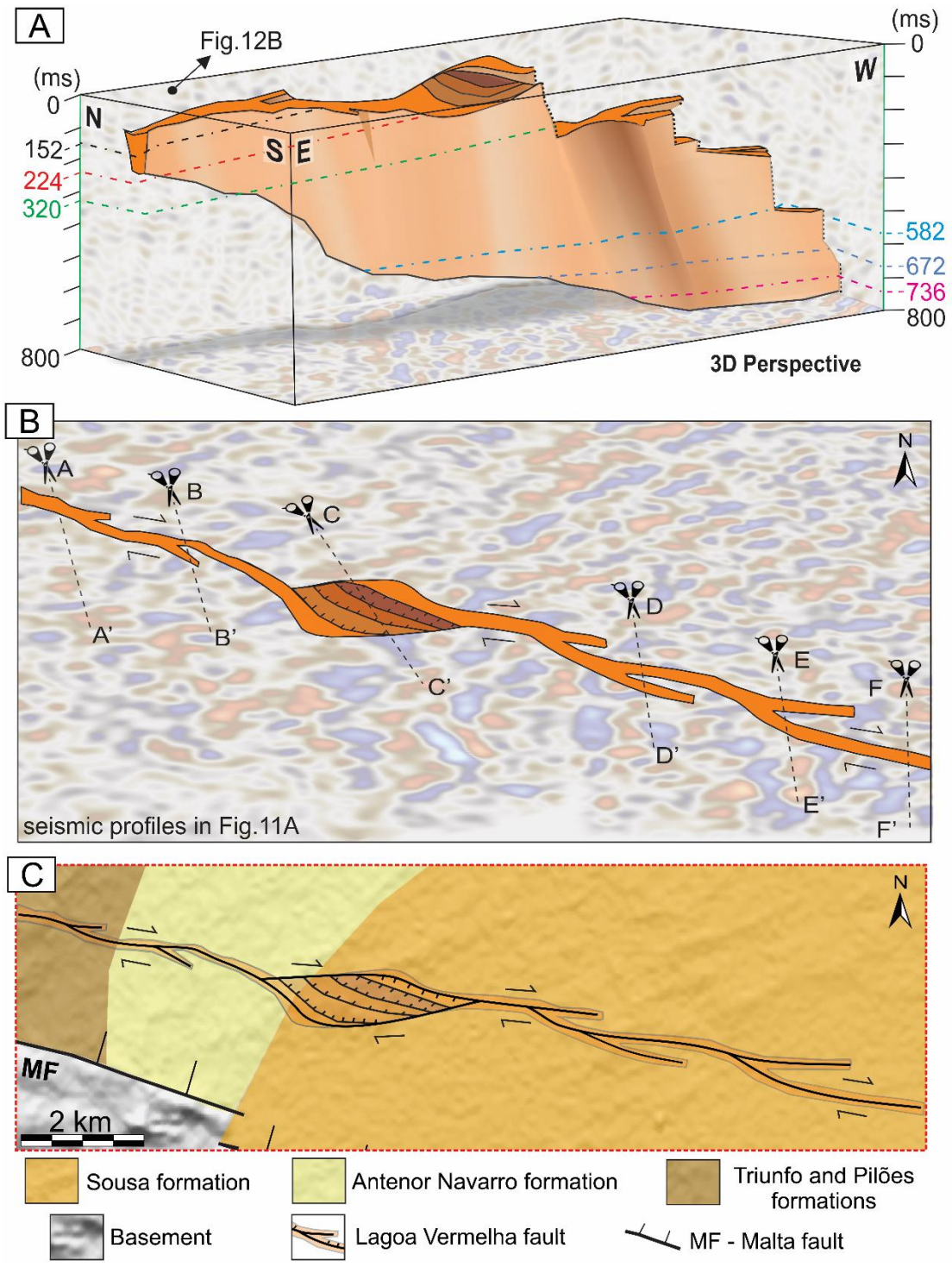

Figure 12 – The 3D fault model analysis and the seismic data used to interpret the fault: (A) a 3D perspective showing the fault geometry and its size variation in depth; (B) its projection on map view with the kinematics; (C) the map view shows the fault with its kinematics and the fault trace used to interpret normal vertical movement. Time slices present fault segments migrating at depth with dextral movement and a central negative flower structure.

We projected the fault trace from the seismic data in the geological map of the RPB. The main fault strikes E-W, with the fault segment striking WNW-ESE, which is parallel to the Malta Fault boundary. We named this fault the Lagoa Vermelha Fault, which occurs between the Patos and Itaporanga shear zones, following the E-W strikes of these structures. The Lagoa Vermelha Fault segments may continue beyond our interpretation. However, we limited the interpretation to the 3D seismic data area, which we used as the base to interpret this fault.

4.2.5 Discussion

4.2.5.1 Seismic attributes versus DNN

We used the coherence (similarity and variance) and fault enhanced attributes (eigen structure fagult enhancement and ant tracking) to identify faults in the onshore seismic data (Figs. 2 and 3). Comparing the results between these seismic attributes, we found that the ant tracking and fault enhancement provide similar results. The fault enhancement reveals structures with similar trends, and fault traces detected have shorter lengths than those imaged by the other seismic attributes. These seismic attributes were widely used in previous fault detection, fault zone and fractures, and fault prediction studies (Marfurt et al., 1998,1999; Jansen, 2005; Silva et al., 2005; Dutzer et al., 2010; Iacopini et al., 2012, 2016; Basir et al., 2013; Qi et al. 2017; Ma et al., 2019; Liao et al., 2019, 2020; Phillips et al., 2019). Even with a great and detailed fault detection capacity, seismic attributes have focused on revealing major structures such as lengthy faults (Wrona et al., 2021), through seismic discontinuities caused by major displacements, and different seismic facies by changes such as amplitude (Chopra and Marfurt, 2007).

We compared the seismic attributes and the DNN results in fault detection. We have considered several parameters such as level of detailed imaged by each method, continuity of the imaged faults, false positive content, and the effect on seismic noise on the quality of detected faults by each method. The DNN approach clearly provides more relevant detail from faults than the seismic attributes. Our results show that although seismic attributes reveal some fault traces (Figs. 2 and 3), the 3D fault shape from DNN results reveals a greater variety of detail with more continuity of fault geometry (Figs. 4, 5, 7, 9, and 10). The interpretation of the Lagoa Vermelha Fault was based on the DNN results and revealed major and minor faults with more continuty, thus detect the 3D fault structure more accurately than the seismic attributes. The use of the DNN fault results was fundamental to understanding and building a 3D image of the fault with flower structure geometry (Fig.12). The DNN results provides a unique opportunity to analyze the kinematics of the fault and its segments (Fig.10).

The structures imged by DNN method have greater continuity of fault traces and their segments can be clearly maped, for example as conjugate faults and flower structures (Figs. 7, 9, and 10). This improved connectivity of the imaged faults enable us to get a better 3D fault geometry in the DNN fault results compared to the results derived

from seismic attributes. The challenges caused by poor continuity in the faults imaged by seismic attributes have been documented by some studies (e.g. Wrona et al., 2021; Guo et al., 2021). The comparison with the seismic attributes confirms that the DNN results reveal details of the geometry of the structures for time slices or seismic profiles, which we point out to be relevant in the 3D seismic interpretation for the characterization of faults (e.g., Walsh et al., 2003; Wu et al., 2019; Wrona et al., 2020; An et al., 2021). In our case, ant tracking results reveal an incomplete characterization of fault geometry in inlines and crosslines compared to DNN (Fig. 7). Showing a detailed fault system using an automatic tool is an innovation, the deep learning has been used recently with a focus on revealing the structures in seismic data characterizing in a 3D perspective (Guo et al., 2021).

The next point that we used to compare the quality of imaged faults from ant tracking and DNN approach is the amount of false positives. This refers to features that are imaged as faults but are in fact artefacts of the approach (based on geological sense check on seismic data). We observed more false positives in ant tracking approach than DNN. In fact, since the DNN approach is supervised (meaning human picked faults have been used as true examples for both training the model and evaluating the quality of the results), there is less chance of false positive than ant trackng approach.

The next point to discuss in the comparison of ant tracking and DNN approaches is the effect on noise in the seismic data on the quality of the results. (Figs. 6, 7, and 8). In our case, the seismic data from the Sousa Subbasin show some areas near the surface presenting zones of little or No Reflection (NR) (Fig. 7). Seismic data with NR gaps can confuse the interpretation of fault discontinuities, cause poor connectivity of imaged with NR gaps (Rummerfeld, 1954; Barnes and Laughlin, 2002; Chopra and Marfurt, 2005; Di et al., 2017, 2019). Therefore, the influence of noise is a challenge that impacts the results of seismic attributes (Silva et al., 2005; Cohen et al., 2006; Hale, 2013; Yan et al., 2019; Wu et al., 2019). Similarly, the results from DNN applications were compared before, where the authors pointed out noisy features and the robustness of DNN model to noise content (Wu et al., 2019). Our results from DNN reveal the fault traces are properly imaged even in the noisy zones of the seismic survey from the NR shallow zone or basement (Figs. 4, 5, and 7). In contrast, the faults detected from seismic attributes show areas that connect the traces with NR or basement noise (Fig. 7). Some studies have focused on understanding the noise effect in seismic interpretation (Friedrich et al., 1998; Stehly et al., 2006), aiming to use noise attenuation and cancelation in the workflow (Libak et al., 2017; Iacopini et al., 2011, 2012). Our study shows that DNN application to image faults in noisy intervals of seismic data is less influenced than seismic attribute-based approaches.

4.2.5.2 Rio do Peixe Basin structural framework

The NE-SW-striking Portalegre and the E–W-striking Malta faults are the main structures bounding the RPB (e.g., Françolin et al., 1994; De Castro et al., 2007; Nogueira et al., 2015; Vasconcelos et al., 2021; Ramos et al., 2022). The faults detected by DNN

and seismic attributes show the same strike of these main RPB structures (E-W and NE-SW), but our results also reveal faults with the NW-SE and N-S strikes (Figs. 2 and 3). Outcrop data in the RPB also indicate fault zones, deformation bands and fracture sets showing the same strikes as mentioned above (e.g., Nogueira et al., 2015; Araujo et al., 2018; Pontes et al., 2019; de Souza et al., 2021; Torabi et al., 2021; Silva et al., 2022; Palhano et al., 2023).

We highlight the strong influence of the Malta Fault on the basin structures, even in the structures present more to the center of the basin, since the longest fault segments are more frequent with E-W trend in the seismic data. Our seismic interpretation indicates that the Lagoa Vermelha Fault is parallel to the E-W-striking Malta Fault. The kinematic interpretation from a 3D perspective of the Lagoa Vemellha Fault shows an oblique fault with dextral and normal movements. This result is consistent with a recent study on the RPB structural framework, which presents two rift phases evidenced by the paleostress change: an initial N-S extension following a second NW-SE opening (Nicchio et al., 2022). We suggest this fault kinematics originated from the initial N-S extension.

Also, our results show the Lagoa Vermelha Fault as a continuous fault trace on seismic data from the basement to the Cretaceous sedimentary package. It coincides with the interpretation made by Ramos et al. (2022), indicating that basement structures acted as weakness zones susceptible to brittle reactivation. In this case, our study shows preexisting basement structures have been reactivated as E-W striking faulting in the basin.

4.2.6 Conclusions

In this study, we compared seismic attributes and deep learning and conclude that DNN is more successful in detecting faults in our studied seismic data. The 3D fault model from deep learning identifies the faults and their segments with better variability of strikes and a greater quantity of minor faults than the seismic attributes. Even with the advances in using seismic attributes, we highlight that seismic noise influences them, making interpretation in near-surface or basement areas difficult, especially in seismic surveys obtained onshore. In the deep learning study, we selected a model that was not trained based on seismic data from Brazil and previous manual interpretation of the RPB, which allows comparison with faults derived from seismic attributes. Additionally, we highlight that this choice was important for comparing the methodologies. The 3D fault model from DNN detects the fault segments with more continuity on inlines, crosslines and time slices, revealing a better fault geometry in a 3D perspective without the noise influence. The fault results from DNN approach was fundamental to characterizing the 3D fault geometry in our case, otherwise using only seismic attributes would have been impossible to automatically detect geometries as conjugate pairs of faults or a flower structure. We interpreted and mapped a new fault, namely Lagoa Vermelha Fault, showing a negative flower structure in the southeastern part of the Rio do Peixe Basin, parallel to the E-W-striking Malta Fault. Our kinematics interpretation shows that the Lagoa Vermelha Fault is an oblique fault with a normal vertical movement and dextral

horizontal movement. As the DNN presents no noise influence and shows a great continuity of the fault segments detected, we can characterize the 3D fault geometry that starts from the basement and crosscuts the entire sedimentary package of the basin.

4.2.7 Acknowledgments

The first author is thankful to the National Petroleum Research School of Norway (NFiP) for funding her research stay at the University of Oslo, which partly contributed to this work. We thank Earth Science Analytics for providing the EarthNet platform and their pretrained fault model, which was used to train and apply the fault interpretation model. We thank Schlumberger for providing a Petrel software license to the Federal University of Campina Grande (UFCG). Petrobras funded the DEBRIP Project (TC 5850.0109438.18.9), coordinated by Francisco C. C. Nogueira (UFCG) and the LSBO Ph.D. grant. LBSO and KMLO especially thanks the Attribute-Assisted Seismic Processing & Interpretation consortium at the University of Oklahoma, whose software was used to compute the seismic attributes.

4.2.8 References

Alaei, B., 2012, Improved fault imaging by integration of frequency decomposition and fault attributes, example from mid Norwegian sea: Proceedings of the 3rd EAGE Fault and Top Seal Conference, C13; Doi: 10.3997/2214-4609.20143024.

Alaei, B., Torabi, A., 2017, Seismic imaging of fault damaged zone and its scaling relation with displacement: Interpretation, 5, 83-93; http://dx.doi.org/10.1190/INT-2016-0230.1.

An, Y., Guo, J., Ye, Q., Childs, C., Walsh, J., Dong, R., 2021, Deep convolutional neural network for automatic fault recognition from 3D seismic datasets: Computers and Geosciences, 153, 104776, https://doi.org/10.1016/j.cageo.2021.104776.

Anvari, R, Kahoo, A. R., Mohammadi, M., Pouyan, A., Random noise attenuation in 3D seismic data by iterative block tensor singular value thresholding: 2017 3rd Iranian Conference on Intelligent Systems and Signal Processing (ICSPIS), 164-168; doi: 10.1109/ICSPIS.2017.8311609.

Araujo, R. E. B., Bezerra, F. H. R., Nogueira, F. C. C., Carvalho, B. R. B. M., Souza, J. A. B., Sanglard, J. C. D., de Castro, D. L., Melo, A. C. C., 2018, Basement control on fault formation and deformation band damage zone evolution in the Rio do Peixe Basin, Brazil: Tectonophysics, 745, 117-131; https://doi.org/10.1016/j.tecto.2018.08.011.

Bahorich, M. S., Farmer, S. L., 1995, 3-D seismic discontinuity for faults and stratigraphic features: The coherence cube: SEG Technical Program Expanded Abstracts, Abstracts: 93-96, https://doi.org/10.1190/1.1887523.

Barnes, A. E., and K. J. Laughlin, 2002, Investigation of methods for unsupervised classification of seismic data: 72nd Annual International Meeting, SEG, Expanded Abstracts, 2221–2224, doi: 10.1190/1.1817152.

Basir, H. M., Javaherian, A., Yaraki, M. T., 2013, Multi-attribute ant-tracking and neural network for fault detection: a case study of an Iranian oilfield: Journal of Geophysics and Engineering, 10; https://doi.org/10.1088/1742-2132/10/1/015009.

Berndt, C., 2005, Focused fluid flow in passive continental margins: Philosophical Transactions of the Royal Society, 363, 2855-2871; doi: 10.1098/rsta.2005.1666.

Birnie, C., Ravasi, M., Liu, S., Alkhlifah, T., 2021, The potential of self-supervised networks for random noise suppression in seismic data: Artificial Intelligence in Geosciences, 2, 47-59; https://doi.org/10.1016/j.aiig.2021.11.001.

Botter, C., Cardozo, N., Hardy, S., Lecomte, I., Escalona, A., 2014, From mechanical modeling to seismic imaging of faults: A synthetic workflow to study the impact of faults on seismic: Marine and Petroleum Geology, 57, 187-207, http://dx.doi.org/10.1016/j.marpetgeo.2014.05.013.

Botter, C., N. Cardozo, S. Hardy, I. Lecomte, G. Paton, and A. Escalona, 2016, Seismic characterization of fault damage in 3D using mechanical and seismic modeling: Marine and Petroleum Geology, 77, 973–990, accessed 23 October 2022; doi: 10.1016/j.marpetgeo.2016.08.002.

Botter, C., N. Cardozo, I. Lecomte, A. Rotevatn, and G. Paton, 2017, The impact of faults and fluid flow on seismic images of a relay ramp over production time: Petroleum Geoscience, 23, 17–28, doi: 10.1144/petgeo2016-027.

Brouwer, F., Huck, A., 2011, An Integrated Workflow to Optimize Discontinuity Attributes for the Imaging of Faults: Attributes: New Views on Seismic Imaging – Their Use in Exploration and Production: 31st Annual, book, DOI: 10.5724/gcs.11.31.0496.

Chen, J., Lu, Y., Yu, Q., Luo, X., Adeli, E., Wang, Y., Lu, L., Yuille, A. L., Zhou, Y., 2021, TransUNet: Transformers Make Strong Encoders for Medical Image Segmentation: arXiv preprint arXiv:2102.04306.

Chopra, S., 2002, Coherence cube and beyond: First Break, 20, 27–33, doi: 10.1046/j.1365-2397.2002.00225.x.

Chopra, S., Marfurt, K. J., 2005, Seismic Attributes: A Historical Perspective: Geophysics, 70, 3-28; https://doi.org/10.1190/1.2098670.

Chopra, S., Marfurt, K. J., 2007, Volumetric curvature attributes for fault/fracture characterization: First Break, 25, 19-30; https://doi.org/10.1190/1.2756864.

Chopra, S., Marfurt, K. J., 2010b, Delineating Fractures from Seismic Attributes: Search and Discovery Article #110124

Cohen, I., Coult, N., Vassilou, A. A., 2006, Detection and extraction of fault surfaces in 3D seismic data: Geophysics, 71, 21-27; doi:10.1190/1.2215357.

Córdoba V. C., Antunes A. F., Jardim de Sá E. F., Nunes da Silva A., Sousa D. C., Lins F. A. P. L., 2008, Análise estratigráfica e estrutural da Bacia do Rio do Peixe Nordeste do Brasil: integração de dados a partir do levantamento sísmico pioneiro: Boletim de Geociências da Petrobras, 16, 53-68.

De Castro, D. L., Oliveira, D. C., Castelo Branco, R. M. G., 2007, On the tectonics of the Neocomian Rio do Peixe Rift Basin, NE Brazil: Lessons from gravity, magnetics, and radiometric data: Journal of South American Earth Sciences, 24 (2–4): 184–202. https://doi.org/10.1016/j.jsames.2007.04.001

De Souza, D. H. S., Nogueira, F. C. C., Vasconcelos, D. L., Torabi, A., Souza, J. A. B., Nicchio, M. A., Pérez, Y. A. R., Balsamo, F., 2021, Growth of cataclastic bands into a fault zone: A multiscalar process by microcrack coalescence in sandstones of Rio do Peixe Basin, NE Brazil: Journal of Structural Geology, 146, 104315; https://doi.org/10.1016/j.jsg.2021.104315.

Di, H., Shafiq, M. A., AlRegib, G., 2017, Seismic-fault detection based on multiattribute support vector machine analysis: SEG Technical Program Expanded Abstracts 2017, Society of Exploration Geophysicists, pp. 2039-2044; 10.1190/segam2017-17748277.1.

Di, H., Wang, Z., AlRegib, G., 2018a, Seismic fault detection from post-stack amplitude by convolutional neural networks: 80th EAGE Conference and Exhibition 2018. European Association of Geoscientists & Engineers, 1–5.

Di, H., Shafiq, M. A., Wang, Z., AlRegib, G., 2019, Improving seismic fault detection by super-attribute-based classification: Interpretation, 7 (3), pp. SE251-SE267, 10.1190/INT-2018-0188.1.

Dorn, G. A., 1998, Modern 3-D seismic interpretation: The Leading Edge, 17, 1177–1328; https://doi.org/10.1190/1.1438121.

Dutzer, J. F., Basford, H., Purves, S. 2010, Investigating fault sealing potential through fault relative seismic volume analysis. In: Geological Society, London, Petroleum Geology Conference Series, 7, pp. 509–515.

Françolin, J. B. L., Cobbold, P. R., Szatmari, P., 1994, Faulting in the early Cretaceous Rio do Peixe basin (NE Brazil) and its significance for the opening of the Atlantic: Journal of Structural Geology, 16, 647-661; doi: 10.1016/0191-8141(94)90116-3.

Friedrich, A., Krüger F., Klinge, K., 1998, Ocean generated microseismic noise located with the Gräfenberg array, Journal of. Seismology, 2, 47-64;

Gersztenkorn A, Marfurt KJ (1999) Eigen structure-based coherence computations as an aid to 3-D structural and stratigraphic mapping. Geophysics 64:1468–1479.

Goodfellow, J., Bengio, Y., Courville, A., 2016. Deep Learning, MIT publishing, ISBN: 9780262035613.

Guo, J., Li, Y., Jessell, M. W., Giraud, J., Li, C., Wu, L., Li, F., Liu, S., 2021, 3D geological structure inversion from Noddy-generated magnetic data using deep learning methods: Computers & Geosciences, 149, 104701; https://doi.org/10.1016/j.cageo.2021.104701.

Hale, D., 2013, Methods to compute fault images, extract fault surfaces, and estimate fault throws from 3D seismic images: Geophysics, 78, 033–043, doi: 10.1190/geo2012-0331.1.

Hustoft, S., Mienert, J., Bünz, S., Nouzé, H., 2007, High-resolution 3D-seismic data indicate focussed fluid migration pathways above polygonal fault systems of the mid-Norwegian margin: Marine Geology, 245, 89-106; doi:10.1016/j.margeo.2007.07.004.

Iacopini, D., and R. W. H. Butler, 2011, Imaging deformation in submarine thrust belts using seismic attributes: Earth and Planetary Science Letters, 302, 414–422, doi: 10.1016/j.epsl.2010.12.041.

Iacopini, D., Butler, R. W. H., Purves, S., 2012, Seismic imaging of thrust faults and structural damage: a visualization workflow for deepwater thrust belts: First Break, 5, 39-46; DOI: 10.3997/1365-2397.30.5.58681.

Iacopini, D., Butler, R. W. H., Purves, S., McArdle, N., De Freslon, N., 2016, Exploring the seismic expression of fault zones in 3D seismic volumes: Journal of Structural Geology, 89, 54-73; https://doi.org/10.1016/j.jsg.2016.05.005.

Jansen, K., 2005, Seismic investigation of wrench faulting and fracturing at Rulison field: M.S. thesis, Colorado School of Mines, Golden, CO, USA.

Jones, G., Knipe, R. J., 1996, Seismic attribute maps; application to structural interpretation and fault seal analysis in the North Sea Basin: First Break, 14; https://doi.org/10.3997/1365-2397.1996024.

Kluesner, J. W., Brothers, D. S., 2016, Seismic attribute detection of faults and fluid pathways within an active strike-slip shear zone: New insights from high-resolution 3D P-Cable™ seismic data along the Hosgri Fault, offshore California: Interpretation, 4, 1F-T121; https://doi.org/10.1190/INT-2015-0143.1.

Krizhevsky, A., Sutskever, I., Hinton, G. E., 2012, Imagenet classification with deep convolutional neural networks: Communications of the ACM, 60, 84-90, accessed 19 October 2022; https://doi.org/10.1145/3065386.

Li, F. Lu, W., 2014, Coherence attribute at different spectral scales: Interpretation, 2. 99-106; https://doi.org/10.1190/INT-2013-0089.1.

Liao, Z., Liu, H., Carpenter, B. M., Marfurt, K. J., Reches, Z., 2019, Analysis of fault damage zones using three-dimensional seismic coherence in the Anadarko Basin, Oklahoma: The American Association of Petroleum Geologist, 103, 1771–1785; DOI:10.1306/1219181413417207.

Liao, Z., Hu, L., Huang, X., Carpenter, B. M., Marfurt, K. J., Vasileva, S., Zhou, Y., 2020, Characterizing damage zones of normal faults using seismic variance in the Wangxuzhuang oil field, China: Interpretation, 8, 1-8; http://dx.doi.org/10.1190/INT-2020-0004.1.

Libak, A., Behzad, A., Torabi, A., 2017, Fault visualization and identification in fault seismic attribute volumes: Implications for fault geometric characterization: Interpretation, 5; http://dx.doi.org/10.1190/INT-2016-0152.1.

Ligtenberg, J. H., 2005, Detection of fluid migration pathways in seismic data: implications for fault seal analysis: Basin Research, 17, 141-153; https://doi.org/10.1111/j.1365-2117.2005.00258.x.

Lohr, T., Krawczyk, C. M., Onken, O., Tanner, D. C., 2008, Evolution of a fault surface from 3D attribute analysis and displacement measurements: Journal of Structural Geology, 30, 6, 690-700; DOI: 10.1016/j.jsg.2008.02.009.

Lorentzen, M. C. L., Bredesen, K., Smit, F. W. H., Hansen, T. H., Nielsen, L., Mosegaard, K., 2022, Mapping Cretaceous faults using a convolutional neural network – A field example from the Danish North Sea: Bulletin Of The Geological Society Of Denmark, 71, 31-50; https://2dgf.dk/.

Lourenço, M. C. M., Jardim De Sá, E. F. J., Córdoba, V. C., Pichel, L. M., 2021, Multi-scale tectono-stratigraphic analysis of pre- and syn-rift sequences in the Rio do Peixe Basin, NE Brazil: Marine and Petroleum Geology, 130, 105127; https://doi.org/10.1016/j.marpetgeo.2021.10512

Lubo-Robles, D., Devegowada, D., jayaram, V., Bedle, H., Marfurt, K., J., Pranter, M. J., 2022, Quantifying the sensitivity of seismic facies classification to seismic attribute selection: An explainable machine-learning study: Interpretation, 10, 41-69; https://doi.org/10.1190/INT-2021-0173.1.

Ma, D., Wu, G., Scarselli, N., Luo, X., Han, J., Chen, Z., 2019, Seismic damage zone and width–throw scaling along the strike-slip faults in the Ordovician carbonates in the Tarim Basin: Petroleum Science, 16, 752-762; https://doi.org/10.1007/s12182-019-0352-4.

Machado, G., A. Alali, B. Hutchinson, O. Olorunsola, K. J. Marfurt, 2016, Display and enhancement of volumetric fault images: Interpretation, 4, 51–61; doi: 10.1190/INT-2015-0104.1.

Mahadik, R., Singh, G, Routray, A., 2022, Multispectral Coherence Analysis for Better Fault Visualization in Seismic Data: IEEE Geoscience and Remote Sensing Letters, 19, 1-5; doi: 10.1109/LGRS.2021.3076213.

Mansfield C. S., Cartwright. J. A., 1996, High resolution fault displacement mapping from three-dimensional seismic data: evidence for dip linkage during fault growth: Journal of Structural Geology, 18, 249-263; https://doi.org/10.1016/S0191-8141(96)80048-4.

Marfurt, K. J., Kirlin, R. L., Farmer, S., Bahorich, M., 1998, 3-D seismic attributes using a semblance-based coherency algorithm: Geophysics, 63, 1150-1165.

Marfurt, K. J., Sudhaker, V., Gerztenkorn, A., Crawford, K. D., Nissen, S. E., 1999, Coherency calculations and the presence of structural dip: Geophysics, 64, 104,111.

Neves, F. A., Zahrani, M. S., & Bremkamp, S. W., 2004, Detection of potential fractures and small faults using seismic attributes: The Leading Edge, 23, 903-906; doi:10.1190/1.1803500.

Nicchio, M. A., Nogueira, F. C. C., Balsamo, F., Souza, J. A. B., Carvalho, B. R. B. M., Bezerra, F. H. R., 2018, Development of cataclastic foliation in deformation bands in feldspar-rich conglomerates of the Rio do Peixe Basin, NE Brazil: Journal of Structural Geology, 107, 132-141; doi:10.1016/j.jsg.2017.12.013.

Nicchio, M. A., Balsamo, F., Cifelli, F., Nogueira, F. C. C., Aldega, L., Bezerra, F. H. R., Vasconcelos, D. L., Souza, J. A. B., 2022, An Integrated Structural and Magnetic Fabric Study to Constrain the Progressive Extensional Tectonics of the Rio do Peixe Basin, Brazil: Tectonics, 41; https://doi.org/10.1029/2022TC007244.

Nogueira, F. C. C., Marques, F. O., Bezerra, F. H. R., de Castro, D. L., Fuck, R. A., 2015, Cretaceous intracontinental rifting and post-rift inversion in NE Brazil: insights from the Rio do Peixe Basin: Tectonophysics, 644, 92-107, accessed 13 September 2022; doi:10.1016/j.tecto.2014.12.016.

Nogueira, F. C. C., Nicchio, M. A., Balsamo, F., Souza, J. A. B., Silva, I. V. L., Bezerra, F. H. R., Vasconcelos, D. L., Carvalho, B. R. B. M., 2021, The influence of the cataclastic matrix on the petrophysical properties of deformation bands in arkosic sandstones: Marine and Petroleum Geology, 124, 104825; https://doi.org/10.1016/j.marpetgeo.2020.104825.

Oliveira, L. S. B., Nogueira, F. C. C., Vasconcelos, D. L., Balsamo, F., Bezerra, F. H. R., Perez, Y. A. R., 2022, Mechanical stratigraphy influences deformation band pattern in arkosic sandstones, Rio do Peixe Basin, Brazil: Journal of Structural Geology, 155, 104510; https://doi.org/10.1016/j.jsg.2022.104510.

Palhano, L. C., Nogueira, F. C. C., Marques, F. O., Vasconcelos, D. L., Bezerra, F. H. R., Souza, J. A. B., Nicchio, M. A., Perez, Y. A. R., Balsamo, F., 2023, Influence of hydrothermal silicification on the physical properties of a basin-boundary fault affecting arkosic porous sandstones, Rio do Peixe Basin, Brazil: Marine and Petroleum Geology, 148, 106062; https://doi.org/10.1016/j.marpetgeo.2022.106062.

Phillips, T. B., Jackson, C. A-L., Bell, R. E., Valencia, A. A., 2019, Rivers, reefs, and deltas; Geomorphological evolution of the Jurassic of the Farsund Basin, offshore southern Norway: Petroleum Geoscience, 26, 81-100; https://doi.org/10.1144/petgeo2018-056.

Qi, J., B. Lyu, A. Alali, G. Machado, Y. Hu, and K. J. Marfurt, 2019, Image processing of seismic attributes for automatic fault extraction: Geophysics, 84, 25–37.

Randen, T. S., Pedersen, I., Sonneland, L., 2001, Automatic extraction of fault surfaces from three-dimensional seismic data: 71st Annual International Meeting, SEG, 511-554.

Rapozo, B. F., Córdoba, V. C., Antunes, A. F., 2021, Tectono-stratigraphic evolution of a cretaceous intracontinental rift: Example from Rio do Peixe Basin, north-eastern Brazil: Marine and Petroleum Geology, 126, 104899; doi:10.1016/j.marpetgeo.2021.104899.

Rummerfeld, B., 1954, Reflection quality, a fourth dimension: Geophysics, 19, 684–694.

Sénant, J., Popoff, M., 1991, Early Cretaceous extension in northeast Brazil related to the South Atlantic opening: Tectonophysics, 198, 35-46; doi:10.1016/0040-1951(91)90129-G.

Silva, C., Marcolino, C., Lima, F., 2005, Automatic fault extraction using ant tracking algorithm in the Marlim south field, Campos Basin: Seg Technical Program Expanded Abstracts, 24; 10.1190/1.2148294.

Silva, J. G. F., Córdoba, V. C., Caldas, L. H. C., 2014, Proposta de novas unidades litoestratigráficas para o Devoniano da Bacia do Rio do Peixe, Nordeste 44, 561-578; doi:10.5327/Z23174889201400040004.

Silva, M. E., Nogueira, F. C. C., Pérez, Y. A. R., Vasconcelos, D. L., Stohler, R. C., Sanglard, J. C. D., Balsamo, F., Bezerra, F. H. R., Carvalho, B. R. B. M., Souza, J. A. B., 2022, Permeability modeling of a basin-bounding fault damage zone in the Rio do Peixe Basin, Brazil: Marine and Petroleum Geology, 135, 105409; https://doi.org/10.1016/j.marpetgeo.2021.105409.

Souza, D. H. S., Nogueira, F. C. C., Torabi, A., Souza, J. A. B., Nicchio, M. A., Pérez, Y. A. R., Balsamo, F., 2021, Growth of cataclastic bands into a fault zone: A multiscalar process by microcrack coalescence in sandstones of Rio do Peixe Basin, NE Brazil: Journal of Structural Geology, 146, 104315; https://doi.org/10.1016/j.jsg.2021.104315.

Stehly, L., Campillo, M., Shapiro, N. M., 2006, A study of the seismic noise from its long-rangecorrelation properties: Journal of Geophysical Research, 111; doi:10.1029/2005JB004237.

Pontes, C. C. C., Nogueira, F. C. C., Bezerra, F. H. R., Balsamo, F., Miranda, T. S., Nicchio, M. A., Souza, J. A. B., Carvalho, B. R. B. M., 2019, Petrophysical properties of deformation bands in high porous sandstones across fault zones in the Rio do Peixe Basin, Brazil: International Journal of Rock Mechanics and Mining Sciences, 114, 153-163; https://doi.org/10.1016/j.ijrmms.2018.12.009.

Preuss, S., Herrendörfer, R.,Gerya, T. V., Ampuero, J.-P., &van Dinther, Y., 2019, Seismic and aseismic fault growth lead to different fault orientations: Journal of

Geophysical Research: Solid Earth, 124, 8867–8889; https://doi.org/10.1029/2019JB017324.

Ramos, G. V., Vasconcelos, D. L., Marques, F. O., de Castro, D. L., Nogueira, F, C. C., Bezerra, F. H. R., Perez, Y. A. R., Souza, J. A. B., Medeiros, V. C., 2022, Relations between inherited basement fabric and fault nucleation in a continental setting: The Rio do Peixe Basin, NE Brazil: Marine and Petroleum Geology, 139, 105635;, https://doi.org/10.1016/j.marpetgeo.2022.105635.

Torabi, A., B. Alaei, and D. Kolyukhin, 2016a, Analysis of fault scaling relations using fault seismic attributes: Geophysical Prospecting, 65, 581–595, doi: 10.1111/1365-2478.12440.

Torabi, A., B. Alaei, D. Kolyukhin, R. H. Libak, R. H. Gabrielsen, and A. Braathen, 2016b. Fault geometric and seismic attributes: An integrated study with focus on the Barents Sea: First Break, 34, 73–80.

Torabi, A., Balsamo, F., Nogueira, F. C. C., Vasconcelos, D. L., Silva, A. C. E., Bezerra, F. H. R., Souza, J. A. B., 2021, Variation of thickness, internal structure and petrophysical properties in a deformation band fault zone in siliciclastic rocks: Marine and Petroleum Geology, 133, 105297; https://doi.org/10.1016/j.marpetgeo.2021.105297.

Torabi, A., Alaei, B., 2022. Fault characterization challenges and recent advances in deep learning. Sixt EAGE Fault and Top Seal Conference, Vienna, keynote talk.

Vasconcelos, D. L., Marques, F. O., Nogueira, F, C. C., Perez, Y. A. R., Bezerra, F. H. R., Stohler, R. C., Souza, J. A. B., 2021. Tectonic inversion assessed by integration of geological and geophysical data: the intracontinental Rio do Peixe Basin, NE Brazil: Basin Research, 33, 705-728; https://doi.org/10.1111/bre.12491.

Xu, H., Sun, S. Z., 2014, Seismic singularity attribute and its applications in sub-seismic faults detection: Acta Geodaetica et Geophysica, 49, 403-414, accessed 20 October 2022; DOI: 10.1007/s40328-014-0071-7.

Yan, Z., Liu, S., Gu, H., 2019, Fault image enhancement using a forward and backward diffusion method: Computers & Geosciences, 131, pp. 1-14, 10.1016/j.cageo.2019.06.004.

Walsh, J. J., Watterson, J., Childs, C., Nicol, A., 1996, Ductile strain effects in the analysis of seismic interpretations of normal fault systems: Geological Society, London, Special Publications, 99, 27–40; http://dx.doi.org/10.1144/GSL.SP.1996.099.01.04.

Walsh, J. J. & Watterson, J. 1987, Distributions of cumulative dis-placement and seismic slip on a single normal fault surface: Journal of Structural Geology 9, 1039-1046; https://doi.org/10.1016/0191-8141(87)90012-5.

Walsh, J., Bailey, W. R., Childs, C., Nicol, A., Bonson, C.G., 2003, Formation of segmented normal faults: A 3-D perspective: Journal of Structural Geology, 25, 1251–1262.guo

Wrona, T. Pan, I., Bell, R. E., Gawthorpe, R. L., Fossen, H., Brune, S., 2020, 3D seismic interpretation with deep learning: A brief introduction: The Leading Edge 40, 524–532; https://doi.org/10.1190/tle40070524.

Wrona, T., Pan, I., Bell, R., Jackson, C. A.-L., Gawthorpe, R., Fossen, H., Osagiede, E., Brune, S., 2022, Complex fault system revealed from 3-D seismic reflection data with deep learning and fault network analysis, EGUsphere, https://doi.org/10.5194/egusphere-2022-1190.

Wu, H., Zhang, B., 2018, A deep convolutional encoder-decoder neural network in assisting seismic horizon tracking; https://doi.org/10.48550/arXiv.1804.06814.

Wu, X., Liang, L., Shi, Y., Fomel, S., 2019b, FaultSeg3D: Using synthetic data sets to train an end-to-end convolutional neural network for 3D seismic fault segmentation: Geophysics, 84, 35-45; http://dx.doi.org/10.1190/geo2018-0646.1.

Yang, D., Cai, Y., Hu, G., Yao, X., and Zou W., 2020, Seismic fault detection based on 3D Unet++ model, SEG Technical Program Expanded Abstracts : 1631-1635.

Liu, N., He, T., Tian, Y., Wu, B., Gao, J., Xu, Z., 2020, Common-azimuth seismic data fault analysis using residual UNet, Interpretation 8: SM25-SM37.

Oikonomou, D., Larsen, E., Alaei, B., Stefos, G., and Purves, S., 2019, EarthNET a native cloud web based solution for next generation subsurface workflows, 81st EAGE Conference and Exhibition 2019 Workshop Programme, p.1 – 4.

Capítulo 5

Conclusões

5 Conclusões

A presente tese tem como principal objetivo obter um maior entendimento em relação as zonas de falhas na Bacia Rio do Peixe, suas especificidades e geometrias, bem como a caracterização dessas em diferentes escalas, compreendendo o impacto e influência de suas estruturas secundárias como as bandas de deformação alterando as camadas sedimentares desde os aspectos sedimentológicos e mecânicos às propriedades petrofísicas da rocha hospedeira. O entendimento da estratigrafia mecânica de arenitos a conglomerados atingidos por estruturas como bandas de deformação ainda demonstra carência de mais estudos, uma vez que essa complexidade em zonas de falhas vem tendo foco em fraturas desde estudos mais antigos aos mais recentes. Além disso, as técnicas de detecção automática de falhas implementadas criaram uma oportunidade de mapear essas estruturas em profundidade, em uma escala mais regional, podendo assim correlacionar essas como o arcabouço estrutural da Bacia Rio do Peixe. Ainda, houve a contribuição acerca do mapeamento e interpretação de uma zona de falha na porção sudoeste da Sub-Bacia de Sousa, a qual foi caracterizada geometricamente em 3D e com uma cinemática dextral-normal. Com isso, os objetivos propostos foram alcançados através das investigações de campo e das técnicas implementadas utilizando os dados de sísmica. Os resultados dessa tese foram comparados com os de artigos publicados anteriormente. A partir dos resultados e discussões apresentados anteriormente, as seguintes conclusões foram extraídas:

(I) Os principais parâmetros que controlam as unidades mecânico-estratigráficas se baseiam principalmente nos seguintes parâmetros: petrofísicos, UCS, espessura

da camada, continuidade da camada lateral, tamanho e frequência do grão, mergulho, espessura, geometria, e linkagem das bandas de deformação.

(II) As interfaces de camadas não impedem a propagação das bandas de deformação através das camadas, mas promovem uma mudança no padrão das bandas de deformação.

(III) A espessura da camada não controla exclusivamente as bandas de deformação. A densidade dessas estruturas apresenta-se com diferentes expressões de deformação em cada camada. Portanto, a densidade não é determinada exclusivamente pela espessura da camada.

(IV) O tamanho do grão da rocha hospedeira, a porosidade e o módulo de Young são fatores que controlam a frequência das bandas de deformação. Esta influência é mais efetiva quando há uma alta porosidade, um tamanho do grão mais fino, e um baixo valor de módulo de Young.

(V) A coesão (UCS) é maior nas bandas de deformação do que na rocha hospedeira (espaço entre bandas). Além disso, a coesão da rocha (UCS) aumenta nas bandas de deformação em unidades com maior granulometria e maior espessura.

(VI) As propriedades mecânicas das camadas impactam fortemente o comportamento mecânico das unidades sedimentares. Estas descobertas podem ter implicações no fluxo de fluido em reservatórios siliciclásticos.

(VII) A comparação entre atributos sísmicos e DNN mostra que este é mais bem sucedido na detecção de falhas, em nosso caso de dados sísmicos (na BRP). Esta comparação permite observar que o modelo de falha 3D do DNN identifica

as falhas e seus segmentos subsidiários com melhor variabilidade de direções e maior quantidade das falhas menores.

(VIII) Mesmo com os avanços no uso dos atributos sísmicos, destacamos que o ruído sísmico os influencia e os condiciona, o que dificulta a interpretação em áreas próximas à superfície ou no subsolo em nosso caso.

(IX) Escolhemos um modelo computacional de falhas que não foi treinado com base em dados sísmicos do Brasil ou interpretação manual prévia da bacia estudada, o que permitiu a comparação com falhas derivadas de atributos sísmicos. Desta forma, ressaltamos que esta escolha foi importante para a comparação das metodologias. O modelo de falha 3D do DNN detecta os segmentos de falha com mais continuidade nas *inlines, xlines e time slices*, revelando melhor a geometria da falha em uma perspectiva 3D, e sem a influência do ruído sísmico.

(X) O modelo de aprendizado profundo foi fundamental para a caracterização da geometria de falha 3D em nosso caso, uma vez que somente utilizando atributos sísmicos não seria possível detectar automaticamente geometrias como pares conjugados de falhas ou uma estrutura em forma de flor. Com isto, interpretamos e mapeamos uma nova falha mostrando uma estrutura em flor negativa em sua porção central, localizada na parte sudeste da Bacia do Rio do Peixe, que também está alinhada paralelamente à tendência E-W da Falha de Malta. Como o DNN não apresenta nenhuma influência do ruído sísmico e mostra uma grande continuidade dos segmentos de falha detectados, foi possível caracterizar a geometria 3D da falha que parte próxima ao embasamento, e cruzando todo o pacote sedimentar da bacia. Nossa interpretação cinemática mostra uma falha

oblíqua com movimento vertical normal e um movimento horizontal dextral da nova falha mapeada, nomeada de Falha Lagoa Vermelha.